Antarctic Specific Features of the Greenhouse Effect:

A Radiative Analysis Using Measurements and Models

Holger Schmithüsen

ALFRED-WEGENER-INSTITUT
HELMHOLTZ-ZENTRUM FÜR POLAR- UND MEERESFORSCHUNG

iup

Universität Bremen

Dissertation

zur Erlangung des Grades

Doktor der Naturwissenschaften (Dr. rer. nat.)

durch den

Fachbereich 1 (Physik/ Elektrotechnik)

Institut für Umweltphysik

Universität Bremen

gemäß der Promotionsordnung vom 25. April 2012.

1. Gutachter: Prof. Dr. Peter Lemke

2. Gutachter: Prof. Dr. Justus Notholt

Die Dissertation wurde angefertigt am

Alfred-Wegener-Institut

Helmholtz-Zentrum

für Polar- und Meeresforschung (AWI)

in Betreuung durch die Gutachter und

Dr. Gert König-Langlo

Bremerhaven, den 10. Dezember 2014

ALFRED-WEGENER-INSTITUT
HELMHOLTZ-ZENTRUM FÜR POLAR-
UND MEERESFORSCHUNG

iup

Universität Bremen

Hiermit erkläre ich, dass ich

1. die Arbeit ohne unerlaubte fremde Hilfe angefertigt habe,
2. keine anderen als die von mir angegebenen Quellen und Hilfsmittel benutzt habe und
3. die den benutzten Werken wörtlich oder inhaltlich entnommenen Stellen als solche kenntlich gemacht habe.

Bremerhaven, den 10. Dezember 2014

Abstract

CO_2 is the strongest anthropogenic forcing agent for climate change since pre-industrial times. Like other greenhouse gases, CO_2 absorbs terrestrial surface radiation and causes emission from the atmosphere to space. As the surface is generally warmer than the atmosphere, the total long-wave emission to space is commonly less than the surface emission. However, this does not hold true for the high elevated areas of central Antarctica. For this region, it is shown that the greenhouse effect of CO_2 is around zero or even negative. Moreover, for central Antarctica an increase in CO_2 concentration leads to an increased long-wave energy loss to space, which cools the earth-atmosphere system. These unique findings for central Antarctica are in contrast to the well known general warming effect of increasing CO_2. The work contributes to explain the non-warming of central Antarctica since 1957.

Contents

Chapter 1: Scientific background

1.1 The structure of the Earth's atmosphere

The Earth's atmosphere is heated mainly by the surface, which is a fundamental property of planetary atmospheres (Thomas and Stamnes 1999, chapter 1.4.1). The heating from below causes the vertical atmospheric temperature profile to tend towards an adiabatic lapse rate.

In the Earth's lowermost part of the atmosphere, the *troposphere*, adiabatic processes typically dominate the vertical temperature gradient (also called *lapse rate*). Hence, the gradient is somewhere between the dry adiabatic value of -9.8°C/km and the moist adiabatic lapse rate, which can be as low as -3°C/km in very humid conditions (Chamberlain 1987). In the US Standard Atmosphere (National Oceanic and Atmospheric Administration et al. 1976) (figure 1.1), which is a good approximation of the global mean atmosphere, the temperature declines at a rate of -6.5°C/km up to the *tropopause*, the upper boundary of the troposphere.

Above that, in the *stratosphere*, the temperature increases due to the vigorous absorption of ultraviolet (UV) radiation from the sun by ozone. The *stratopause* marks the upper end of this layer, where the ozone-induced heating dictates the sign of the vertical temperature gradient.

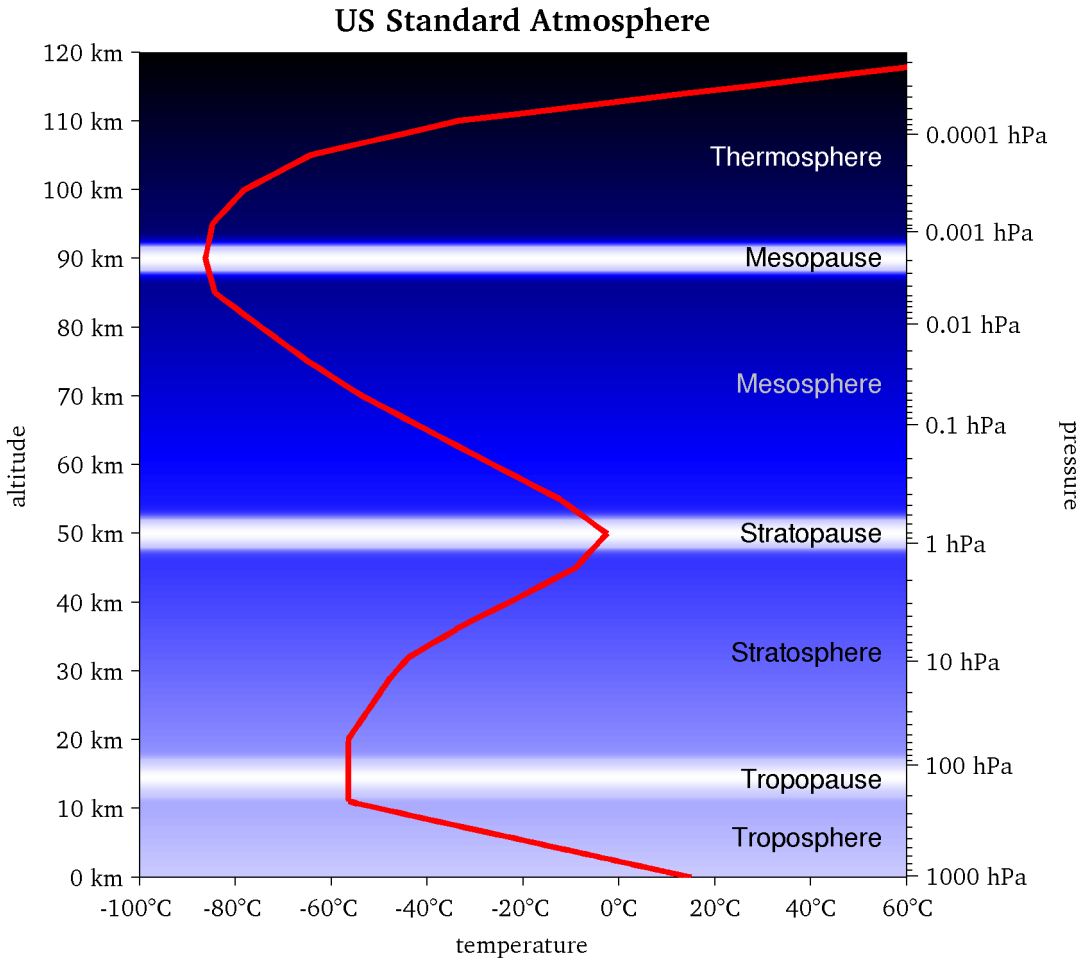

***Figure 1.1**: The mean temperature structure of the Earth's atmosphere as defined in the US Standard Atmosphere (1976). The pressure at the surface is 1013.25 hPa.*

Ozone itself is created by photolysis, with the help of high energetic UV photons from the sun. There is little vertical exchange of air through the tropopause and the production of ozone is confined to a certain depth into the atmosphere, when seen from above. Hence, the location of the ozone layer, and with this the location of the strato- and tropopause, are set by the amount of UV radiation provided by the sun as well as the chemical and radiative properties of ozone.

In the *mesosphere*, which is limited by the stratopause at the lower and by the *mesopause* at the upper end, the temperature decreases again at a rate of approximately -3°C/km. The thermal structure of this atmospheric layer is governed both by radiative and by dynamical processes. In the mesosphere, not only the UV heating by ozone decreases with altitude, also the infrared cooling to space, mainly by CO_2, diminishes. In addition to that, convective motion plays a role for the temperature profile. (Salby 1996, chapter 1.2.3 and 8.5.3; Thomas and Stamnes 1999, chapter 1.4.1).

The *thermosphere*, which comprises the upper 0.2 Pa or 0.0002 % of the atmosphere, is characterised by photoionisation heating due to energetic UV and X-ray absorption. This is a very hot layer, reaching temperatures of more than several hundreds degrees Celsius. However, the effect of temperature in this layer is not comparable to that in the tropo- or stratosphere, due to the tremendous mean free path lengths of the molecules. Also, ionised molecules in the thermosphere take considerable time before they recombine, which makes the atmosphere a plasma (Salby 1996; Thomas and Stamnes 1999).

The atmosphere in the polar regions features two distinct qualitative differences to the above description:

1. The surface heating is drastically reduced due to the geographic location on the one hand; and due to the high amount of reflected sunlight (= high *surface albedo*) from the mostly snow-covered surfaces on the other hand. The atmospheric circulation creates a meridional heat transport which causes the polar atmosphere to be much warmer than the radiative equilibrium would allow. This yields massive surface temperature *inversions*, i.e. a positive lapse rate in the lowermost part of the troposphere.

2. During the polar night, no sun light is available to heat the stratosphere, and the meridional heat transport does not compensate for that. Therefore, the stratosphere cools down, yielding a negative temperature gradient up to altitudes beyond 20 km. Considering other definitions of the tropopause, e.g. using the ozone profile or dynamical metrics, the minimum in the temperature profile does not mark the tropopause any more.

The gases nitrogen (N_2), oxygen (O_2) and argon (Ar) constitute almost the entire atmosphere. When water vapour is neglected, their respective volume fractions are 78 % (N_2), 21 % (O_2) and 1 % (Ar), which are virtually constant throughout the atmosphere up to the mesopause. In addition to that, the atmosphere contains so-called *trace gases*: These are gas species which occupy only small fractions of the total volume, but greatly influence the radiative or chemical properties of the atmosphere. Their distribution in the atmosphere is not necessarily constant. Typical trace gas concentrations range between several hundred parts (atoms or molecules) per million (ppm) and some parts per billion (ppb) or even parts per trillion (ppt). The exception to that is the trace gas water vapour: Its concentration is extremely variable in space and time, and can reach values of more than 5 %, but its presence is mostly confined to the troposphere.

1.2 The role of radiation in climate

The Earth receives electromagnetic radiation from the sun, the so-called *solar* or *short-wave* radiation. In order to compensate for this permanent heating, the Earth emits *thermal infrared*, *terrestrial*, or *long-wave* electromagnetic radiation. These two radiation regimes govern the Earth's climate.

To a first approximation, the incoming solar radiation as well as the thermal emission of our planet's surface is spectrally distributed according to Plack's law, which gives the spectral radiance of a black body B_λ for a certain wavelength λ at temperature T:

$$B_\lambda(T) = \frac{2hc^2}{\lambda^5} \cdot \frac{1}{exp(\frac{hc}{k\lambda T}) - 1} \quad , \tag{1.1}$$

with the h being the Planck constant, c the speed of light and k the Boltzmann constant.

At the top of the Earth's atmosphere (TOA), the incoming solar energy amounts to 1360.8 ± 0.5 W/m^2 (Kopp and Lean 2011), which is incident on the circular area of the Earth's cross section. Distributed over the spherical area of the Earth's surface this corresponds to some 340 W/m^2 (see figure 1.2), of which 100 W/m^2 are reflected back into space. According to the spectral and hemispherical integration of Planck's law, the Stefan-Boltzmann law

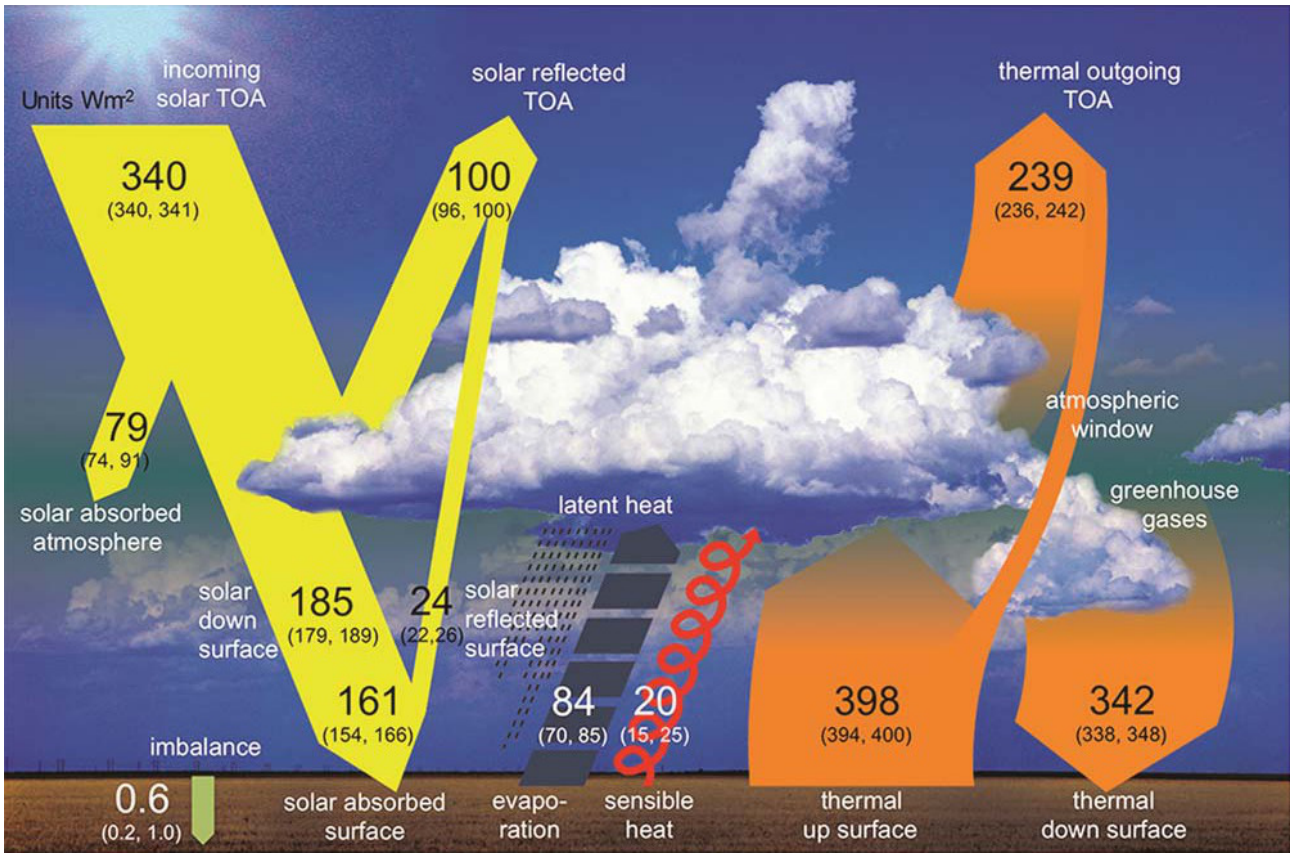

***Figure 1.2**: The Earth's energy budget as published by IPCC* (2013, figure 2.11) *adapted from Wild et al. (2012). All numbers given are in units of W/m^2. The small numbers in parathesis give an estimate of the uncertainty ranges, which are individually justified in the discussion part of Wild et al.* (2012, section 5). *Basically, they cover the range of observational constraints. Figures for thermal upward surface flux and evaporation deviate slightly from those in the original publication (Wild et al. 2012).*

$$F_{BB} = \sigma T^4 \,, \tag{1.2}$$

with the Stefan-Boltzmann constant σ, and F_{BB} denoting the radiative flux of a black body, the 240 W/m^2 of absorbed solar radiation would yield an average surface temperature of -18°C. This is some 33°C cooler than the observed average surface air temperature of approximately 15°C. The in this respect rather warm surface of the Earth is attributed to the presence of radiatively active constituents in the atmosphere: Molecules, that absorb and emit terrestrial radiation; the so-called *greenhouse gases* (GHGs). These gases insolate the Earth by causing a downwelling radiative flux at the surface and by "shielding" parts of the surface emission from being emitted into space. More precisely, the GHGs absorb and emit the terrestrial radiation at characteristic wavelengths. This is what is known as *greenhouse effect* (GHE). As the spectral radiance of the emission strongly depends on temperature, and as the surface is usually warmer than the atmosphere, the long-wave emission of GHGs into space is mostly less than the surface emission. On global average, the thermal outgoing radiation at top of atmosphere is estimated to be around 239 W/m^2 while the surface emission is some 398 W/m^2 (IPCC 2013).

Spectral separation of solar and terrestrial radiation

By assuming the solar and terrestrial spectra to be well approximated by Planck's law, one can easily separate the two spectral regions for the conditions on Earth: Figure 1.3 shows the normalised Planck curves for typical solar and terrestrial temperatures (black dashed lines). The two curves intersect at 4.2 µm. If this was taken to separate the two spectra, the energy emitted in the overlapping parts would not be equal: 0.83 % of the solar energy is emitted at wavelength greater than 4.2 µm, while only 0.26 % of the terrestrial emission lies below this wavelength. Figure 1.3 also shows the spectrally integrated Planck curves as functions of the integration limit λ. The red solid curve denotes the fraction of solar energy, which is emitted at longer wavelengths than the wavelength λ on the abscissa. The blue solid curve indicates the fraction of terrestrial emission at wavelengths shorter than λ. These two curves intersect at 4.7 µm, leaving 0.62 % of the total energy of both spectra to overlap with the other spectrum. In this work, the so-determined value of λ_0 = 4.7 µm is taken to separate the solar and terrestrial spectra.

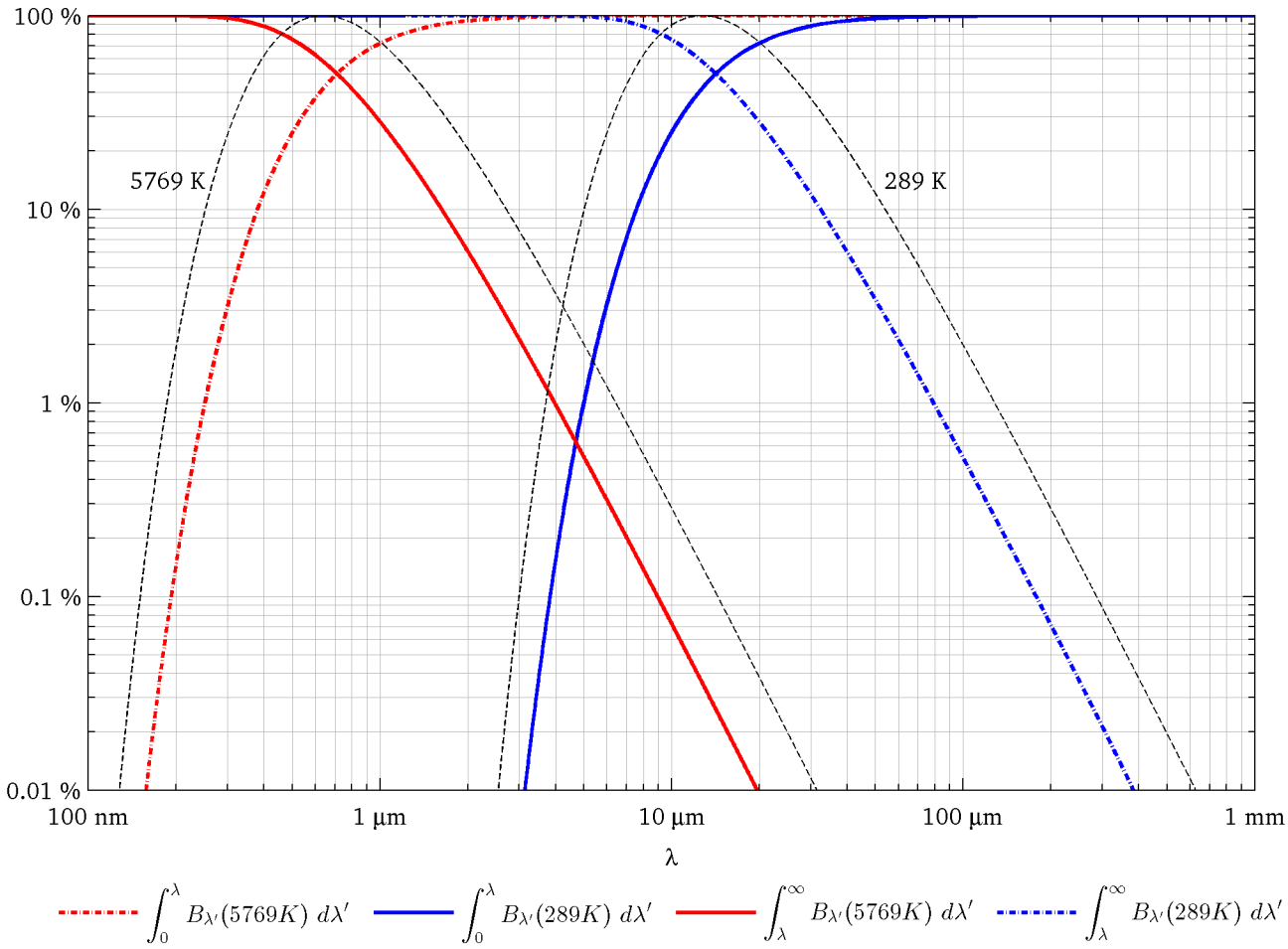

Figure 1.3: *Spectrally integrated Planck functions for the solar and the terrestrial idealised blackbody emission spectra. The coloured lines show the fraction of blackbody irradiance, that is emitted below (rising curves) and above (falling curves) the wavelength λ. At 4.7 µm, less than 0.7 % of the total solar irradiance is emitted at higher wavelengths, while the same fraction of the terrestrial spectrum is emitted below this wavelength. The legend entries omit the applied normalisation (division with the integral over the full spectrum) for clarity. The black dashed curves indicate the normalised quantity λB_λ of both spectra. The solar curve (5769 K) corresponds to blackbody emission of 1360.8 W/m² (Kopp and Lean 2011), while the terrestrial curve (289 K) corresponds to 398 W/m² (Loeb et al. 2009).*

1.3 Anthropogenic impact on climate

The Intergovernmental Panel on Climate Change (IPCC) issues the most comprehensive and broadly accepted reports on global climate change. Particularly, the influence of human activity is thoroughly analysed and documented. The last report of Working Group I, entitled *"The Physical Science Basis"*, which is a contribution to the Fifth Assessment Report (AR5), was published in 2013 (IPCC 2013). The report reaffirms the key findings of IPCC's earlier reports: the anthropogenic impact on the Earth's climate. AR5 names and quantifies manifold causes for climate change, and restates that anthropogenic emissions of carbon dioxide have caused the largest impact on our climate since 1750.

As metric to quantify the influence of drivers of climate change, the concept of *radiative forcing* (RF) is widely used. The concept is based on the net radiative flux change induced by a certain forcing agent. To calculate radiative forcing, the flux change is commonly, but not always, considered at the tropopause. AR5 distinguishes several variations of radiative forcing: *Instantaneous radiative forcing*, *stratospherically adjusted radiative forcing*, and *effective radiative forcing*, which allows for some degree of tropospheric adjustment to the forcing, also. Chapter 8.1 of AR5, which is largely based on the work of Hansen et al. (2005), depicts the various metrics and evaluates their efficiency as indicator of climate change.

Figure 1.4 gives the assessed stratospherically adjusted radiative forcing of the main drivers of climate change. It clearly identifies CO_2 as the main contributor to the global anthropogenically induced change of our climate.

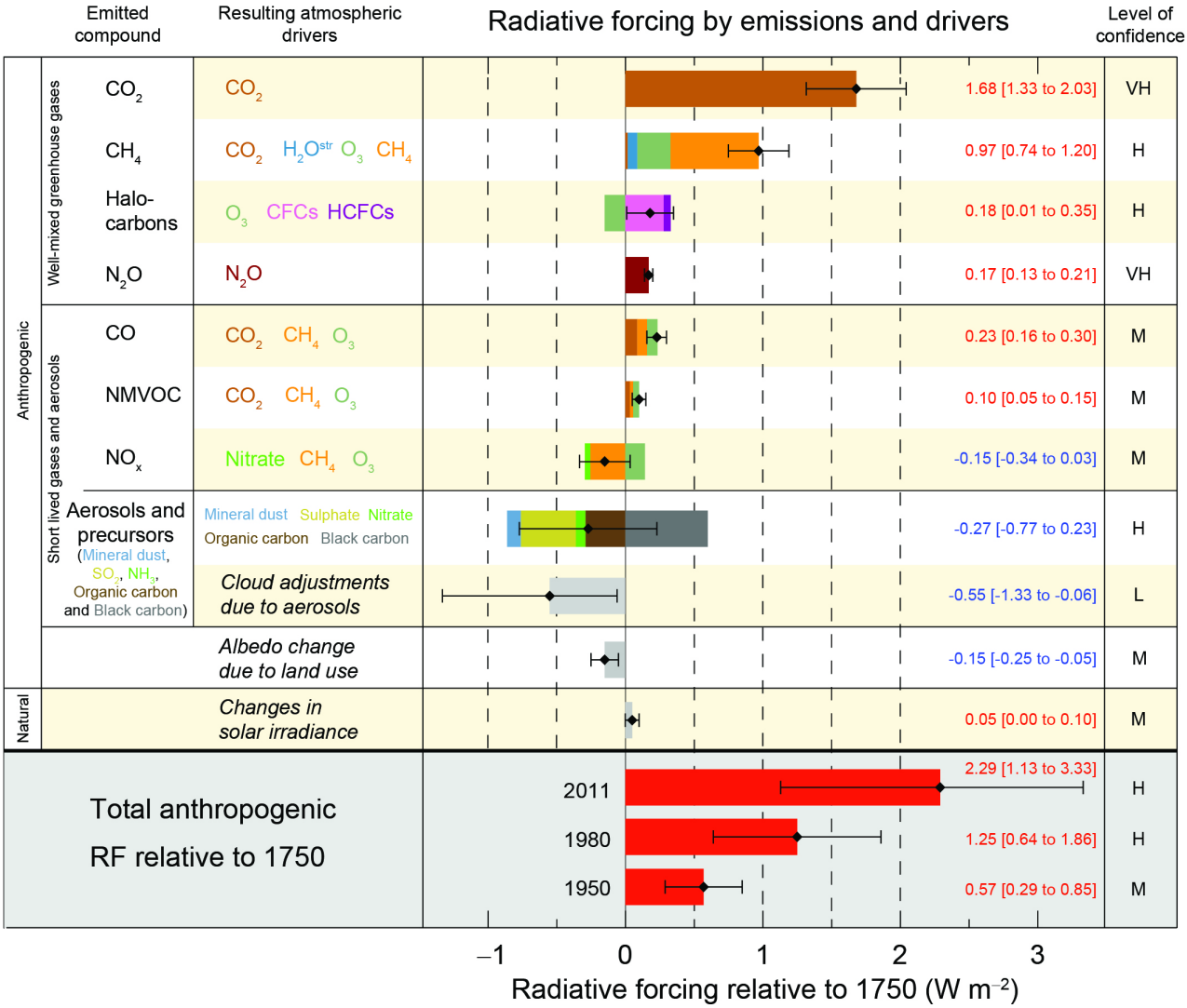

Figure 1.4: *Graphic and caption from AR5 (IPCC 2013, Summary for Policymakers, figure SPM.5): "Radiative forcing estimates in 2011 relative to 1750 and aggregated uncertainties for the main drivers of climate change. Values are global average radiative forcing (RF), partitioned according to the emitted compounds or processes that result in a combination of drivers. The best estimates of the net radiative forcing are shown as black diamonds with corresponding uncertainty intervals; the numerical values are provided on the right of the figure, together with the confidence level in the net forcing (**VH** – very high, **H** – high, **M** – medium, **L** – low, **VL** – very low). Albedo forcing due to black carbon on snow and ice is included in the black carbon aerosol bar. Small forcings due to contrails (0.05 Wm^{-2}, including contrail induced cirrus), and HFCs [hydrofluorocarbons; note from the author], PFCs [perfluorocarbons; note from the author] and SF_6 (total 0.03 Wm^{-2}) are not shown. Concentration-based RFs for gases can be obtained by summing the like-coloured bars. Volcanic forcing is not included as its episodic nature makes is difficult to compare to other forcing mechanisms. Total anthropogenic radiative forcing is provided for three different years relative to 1750. [...]"*

1.4 Topography of Antarctica

The continent Antarctica (figure 1.5) is covered almost entirely by a massive ice sheet with a total area of nearly 14 million km^2 (Fretwell et al. 2013). This is about one third more than the area of Europe. Most of the ice is grounded on the underlying rock, but some 12 % of the total area float on the ocean, forming the so-called ice shelves. The central parts of the continent form a vast plateau, while the edges of the ice sheet are comparably steep. The mean thickness of the ice sheet, excluding the ice shelves, amounts to 2126 m (Fretwell et al. 2013) making Antarctica by far the highest continent (Zhang 2005). The Transantarctic Mountains separate the continent into what is known as West and East Antarctica. While the West Antarctic ice sheet is comparably small, the East Antarctic ice reaches up to 4082 m above sea level (ASL). In terms of potential contribution to global sea level rise, the East Antarctic ice mass makes 53.3 m of the total 58.3 m of sea level rise estimated for the entire Antarctic ice sheet (Fretwell et al. 2013).

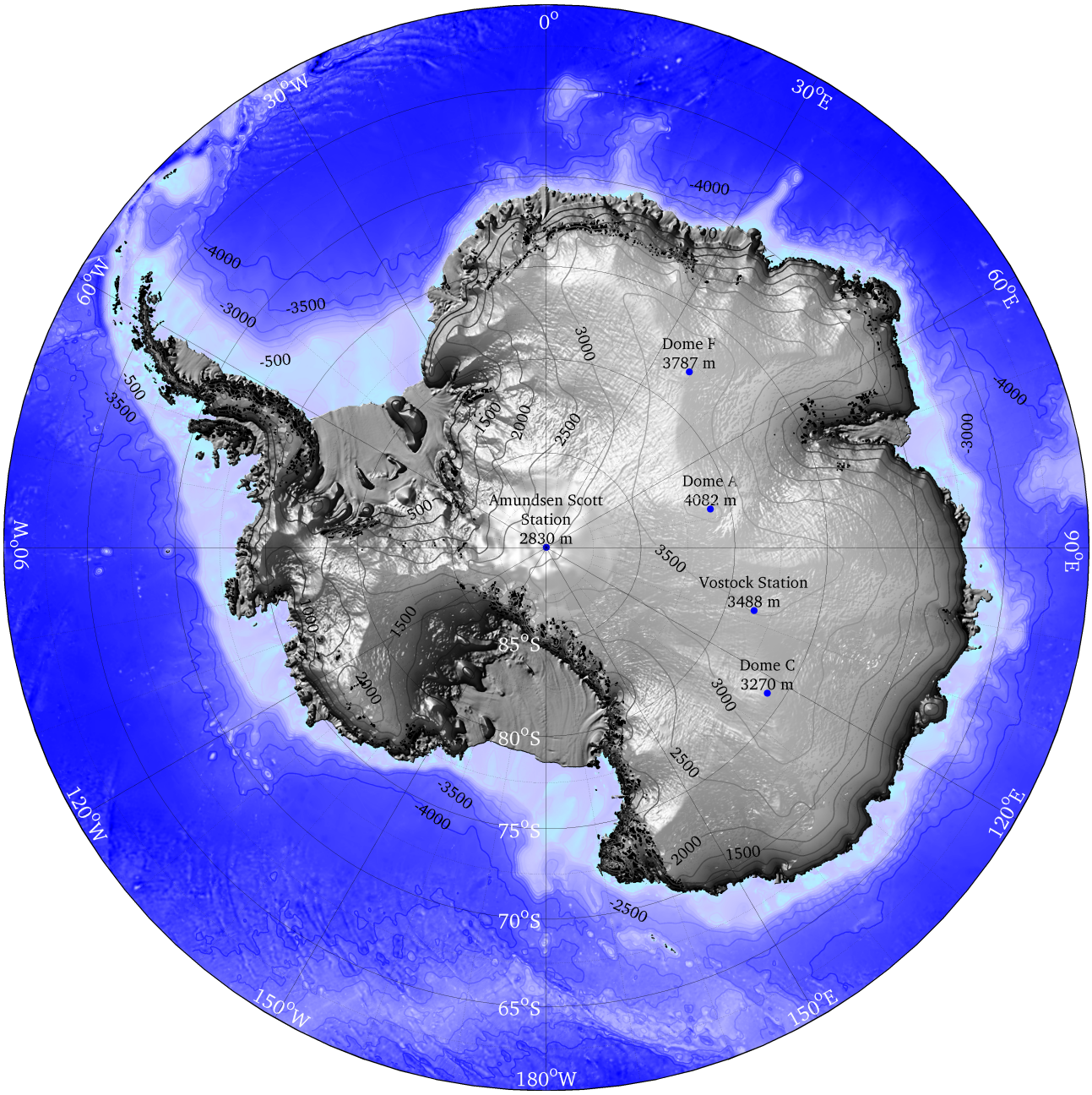

Figure 1.5: *Topography of the Antarctic. Contour lines are shown in 500 m intervals. The underlying data were taken from the International Bathymetric Chart of the Southern Ocean (IBCSO) (Arndt et al. 2013), which includes Bedmap2 data (Fretwell et al. 2013). Altitude readings for Amundsen-Scott and Vostok Station are those reported in the Global Telecommunication System of the World Meteorological Organisation.*

1.5 Antarctic temperature records

Antarctica is the continent with the coldest surface temperatures on our planet. Yearly averages below -50°C in the center of East Antarctica are quite common. Additionally, the lowest surface air temperature ever recorded was measured on the Antarctic plateau. Besides the polar location, the reasons for the extremely cold surface of Antarctica are on the one hand the continental character of the climate, and on the other hand the high elevation of vast areas of this continent. In the following, several temperature records and analyses of Antarctic surface temperature are presented.

1.5.1 Station records

The Scientific Committee on Antarctic Research (SCAR) fosters the Reference Antarctic Data for Environmental Research (READER) project, which aims to provide high quality, long term records of mean surface and upper air in-situ meteorological measurements (Turner et al. 2004). They provide monthly averages of temperature, pressure and wind from manned stations, automatic weather stations and upper air soundings.

The longest instrumental records of meteorological parameters from the Antarctic plateau are those from the year-round manned stations Amundsen-Scott (South Pole) and Vostok (78.5°S, 107°E). The records of surface temperature, pressure and wind were started during the International Geophysical Year (IGY) in 1957/58 and are continued until today.

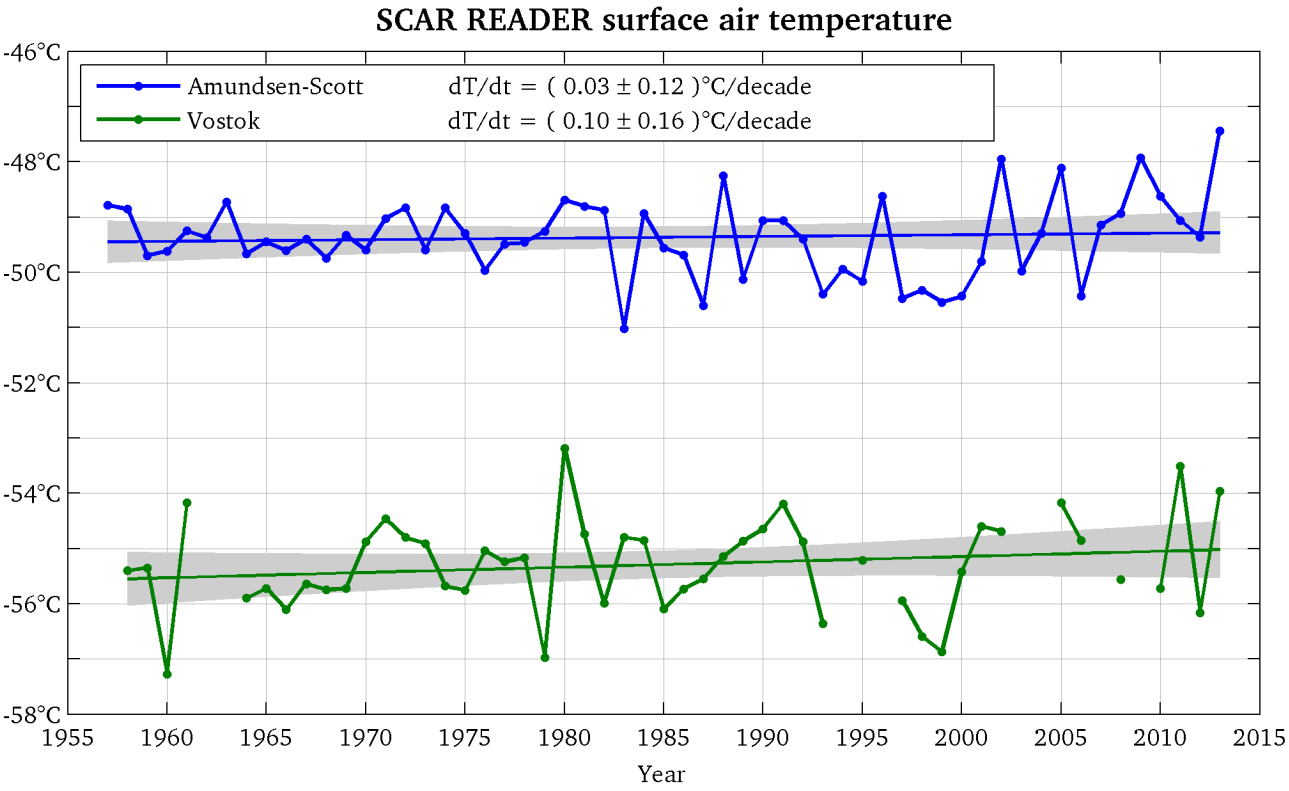

Figure 1.6: *The longest records of surface air temperature from the Antarctic plateau: Amundsen-Scott (South Pole) and Vostok (78.5°S, 107°E). Yearly averages and linear trends are shown in colour. The grey shaded areas denote the 95 % confidence interval of the mean. Any linear trend within the range of uncertainty as given in the legend would be inside the grey patches. The data shown is compiled in the READER data set (Colwell and Turner 2014; Turner et al. 2004).*

Figure 1.6 shows the South Pole and Vostok time series of yearly averaged surface air temperature as compiled in the READER data set. There are no statistically significant linear trends (on the 95 % confidence level) over the last 57 years in these two records . The South Pole record shows almost no temperature trend at all ((0.03 ± 0.12)°C/decade). However, the interannual variability seems to have increased since 1982. The Vostok record shows a slight warming trend ((0.10 ± 0.16)°C/decade), but still not significant.

Figure 1.7 depicts the monthly means of the READER surface air temperature record from the South Pole. None of the months show statistically significant linear trends (see also table 1.1). However, non-significant warming trends greater than 0.1°C/decade are observed in Summer, i.e. November until January as well as in September and March. Cooling trends, also not significant, exceeding 0.1°C/decade are found for February, May and June.

The trends for Vostok are illustrated in figure 1.8 and table 1.1. The data shows statistically significant warming trends in summer (November and December), whereas the other trends are not significant. May and June show cooling trends exceeding 0.1°C/decade, still not significant on the 95 % confidence level.

Table 1.1: *Linear trends of monthly means for the two longest surface air temperature records from the Antaractic plateau. The records are shown in figures 1.7 and 1.8. Uncertainties given are calculated from linear regression analysis using the 95 % confidence level. Statistically significant trends are highlighted.*

Month	Amundsen-Scott [°C/decade]	Vostok [°C/decade]
January	0.10±0.30	0.21±0.24
February	-0.18±0.35	-0.04±0.28
March	0.22±0.39	-0.03±0.36
April	-0.03±0.51	0.11±0.44
May	-0.19±0.42	-0.12±0.48
June	-0.19±0.52	-0.16±0.53
July	-0.09±0.47	0.31±0.60
August	0.04±0.48	0.32±0.62
September	0.21±0.53	0.10±0.56
October	-0.07±0.37	0.04±0.46
November	0.32±0.33	0.42±0.25
December	0.17±0.33	0.32±0.29

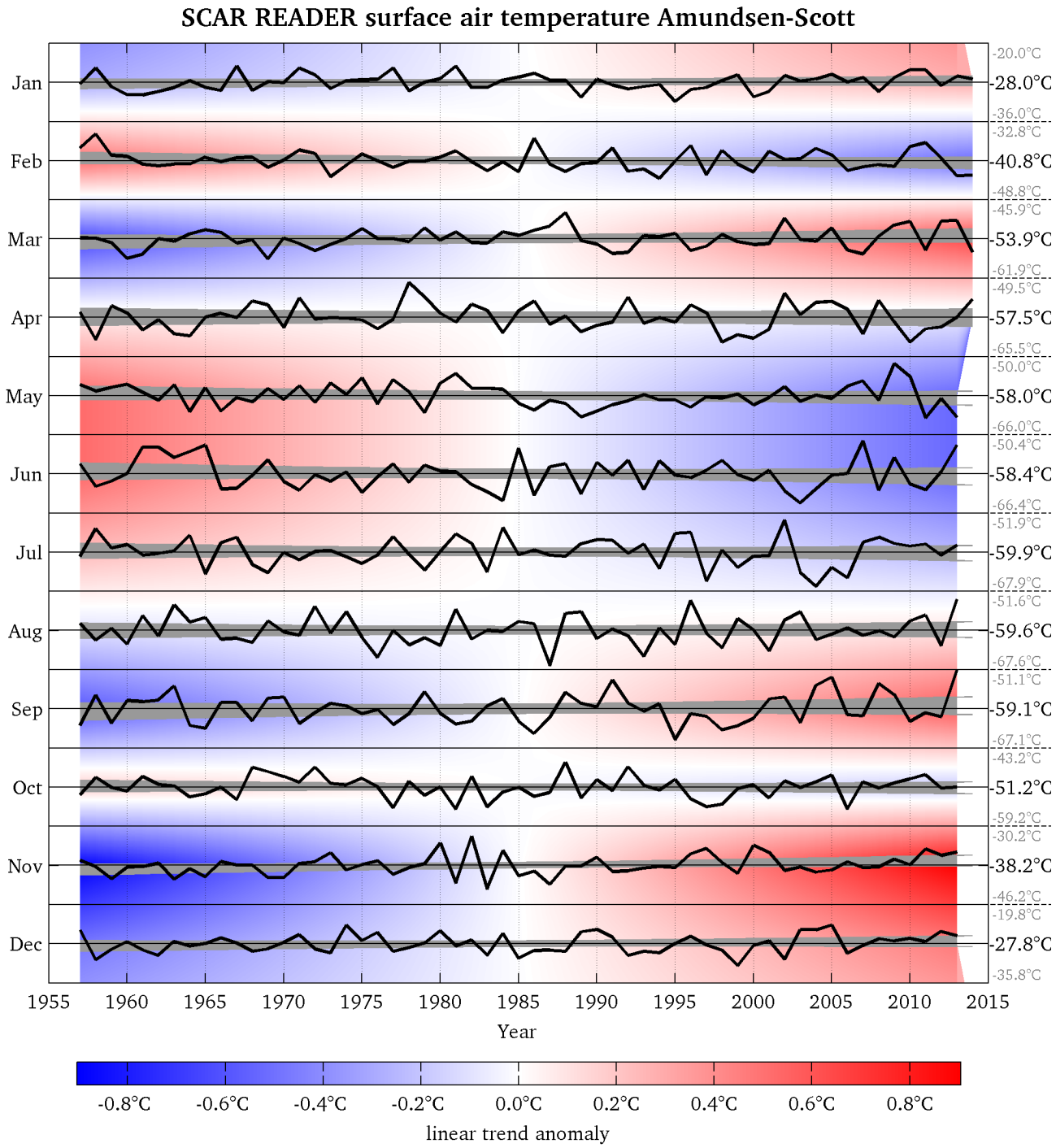

Figure 1.7: *Monthly means (black lines) of surface air temperature from South Pole for the period 1957 - 2014. The black numbers on the right give the mean temperature of the respective month over the entire period. The temperature range shown around the mean is ±8°C for all months. The colour shading illustrates the linear trend anomalies. The grey shaded areas denote the 95 % confidence interval of the mean. None of the trends are statistically significant. See table 1.1 for the numeric trend values. Data has been taken from the READER data set (Colwell and Turner 2014; Turner et al. 2004).*

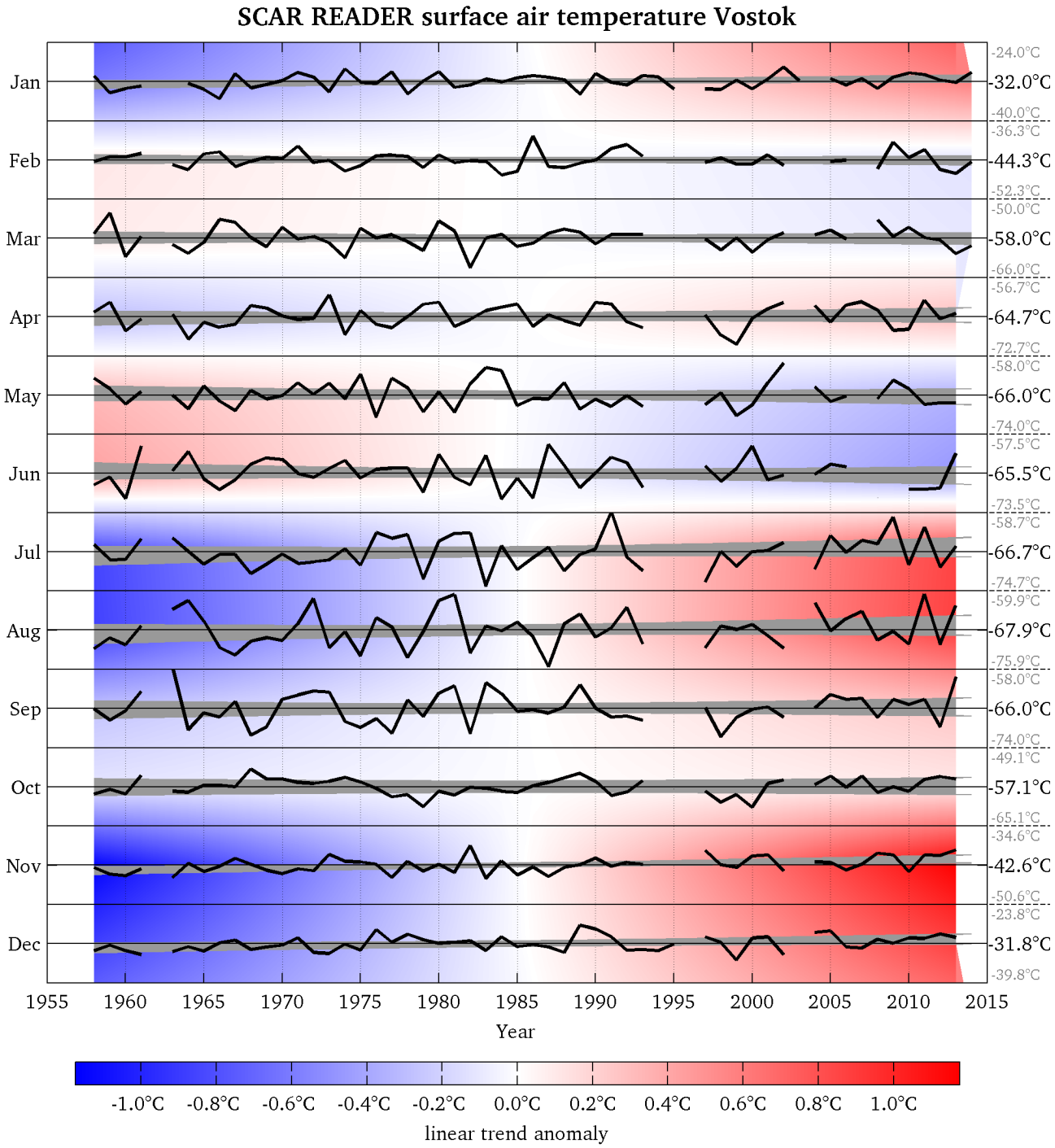

Figure 1.8: *Monthly means (black lines) of surface air temperature from Vostok for the period 1958 - 2014. The black numbers on the right give the mean temperature of the respective month over the entire period. The temperature range shown around the mean is ±8°C for all months. The colour shading illustrates the linear trend anomalies. The grey shaded areas denote the 95 % confidence interval of the mean. Only the November and December trends are statistically significant. See table 1.1 for the numeric trend values. Data has been taken from the READER data set (Colwell and Turner 2014; Turner et al. 2004).*

1.5.2 Spatially interpolated analyses

The Goddard Institute for Space Studies (GISS) has a long history in compiling surface temperature measurements in order to estimate global surface temperature change since 1880 (Hansen et al. 2010). The GISS Surface Temperature Analysis (GISTEMP) uses many sources of measurement data. For the Antarctic continent it utilises the SCAR READER data set.

Figure 1.9a shows the linear surface temperature trend of the GISTEMP data set for the period 1958 - 2002 and Figure 1.10 and 1.11 show the decadal GISTEMP surface temperature anomaly for the time since the IGY 1957/58. The data set shows pronounced warming in the northern hemisphere, while the southern hemisphere has experienced smaller changes. Substantial changes in the Antarctic region are evident at the Antarctic Peninsula, also extending westwards as far as the Ross Sea. For most of the period shown, the interior of the Antarctic continent reveals virtually no changes in surface air temperature. However, the most recent years do show a warming trend also for parts of the east Antarctic plateau.

Chapman and Walsh (2007) analysed surface air temperature measurements from land surface stations, automatic weather stations as well as ship and buoy observations from the high-latitude southern hemisphere (figure 1.9b). They compiled the available records to deduce linear temperature trends for the entire Antarctic region (60°S - 90°S) for the period from 1958 to 2002. Their analysis shows a strong warming trend for the Antarctic Peninsula, partly statistically significant on the 95 % level. Apart from that, there is only one small region on the shoreline of Antarctica at 15°E which shows a significant trend; a warming of some 0.1°C/decade. The center of the high elevated Antarctic plateau appears to have a slight cooling trend, extending towards the east side of the Weddell Sea. However, this trend is statistically not significant. For the Antarctic continent, their result is in agreement with the GISTEMP data set (figure 1.9a): Both show strong

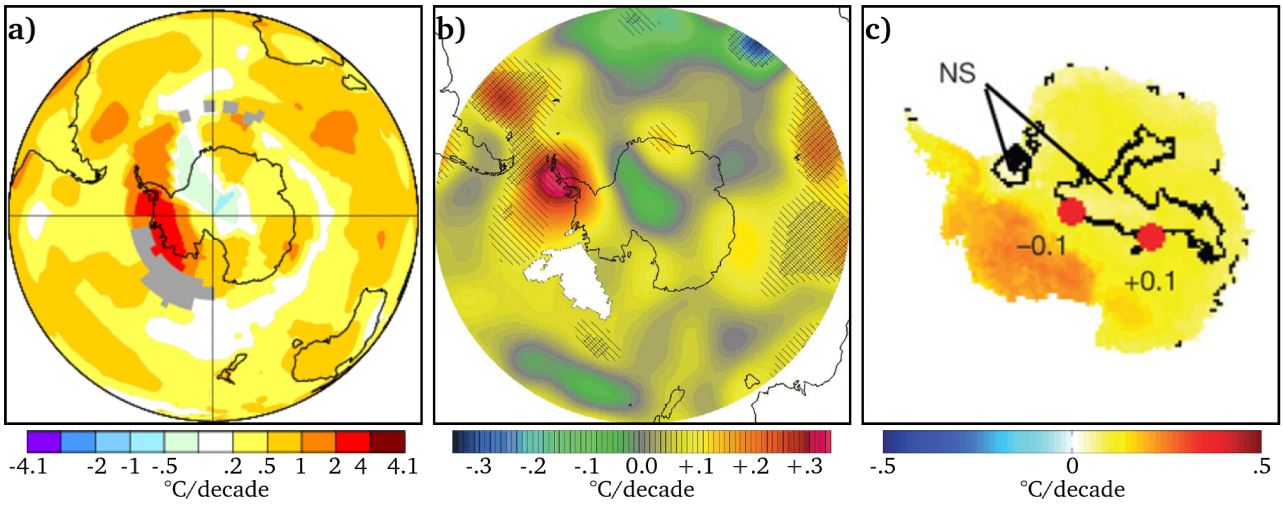

Figure 1.9: *Linear trends of annual mean surface temperature from various studies:* ***a)*** *GISTEMP, comprising continental data from manned stations and AWSs for the period 1958 - 2002. The map was created using the GISS's web-interface (Schmunk 2014).* ***b)*** *Chapman and Walsh's (2007) trend analysis also using manned stations' and AWS data from 1958 - 2002. Single hatching denotes statistical significance on the 95 % level, cross-hatching 99 %. The figure has been rotated by 90° for better comparison.* ***c)*** *Analysis by Steig et al. (2009) incorporating data from manned stations, AWSs and satellite-measured brightness temperatures for cloud free conditions; covering the period 1957 - 2006. The red dots denote the locations of the stations Amundsen-Scott and Vostok, with the respective trend values given. Regions with significant trends (95 % level) are confined by black contour lines; non-significant trends are labelled "NS". (Reprinted by permission from Macmillan Publishers Ltd: Nature, Steig et al. 2009, copyright 2009)*

warming at the Peninsula, particularly on the west coast, with mostly moderate warming along the coast around East Antarctica, and slight cooling on the plateau extending towards the Weddell Sea.

Steig et al. (2009) carried out a similar analysis, also incorporating the SCAR READER data, but additionally included surface temperature measurements obtained by satellite. The latter are available only for clear-sky conditions, as they are derived from measurements of thermal infrared emission. However, they contribute data for large, otherwise data void areas. Figure 1.9c shows their derived surface temperature trend for the period 1957 - 2006. They report a *"significant warming in East Antarctica at 0.10±0.07°C per decade"*, which is in contrast to cooling found by the studies mentioned before (see figure 1.9). However, for a small region around the South Pole they report a cooling trend of some 0.1°C/decade. According to their analysis, the strongest warming does not occur at the Peninsula, but in the entire West Antarctic.

Seasonal temperature trend analysis by Chapman and Walsh (2007) and Steig et al. (2009) are shown in figure 1.12. Virtually all trends during all four seasons in East Antarctica are not significant. However, Chapman and Walsh report a slight warming on the East Antarctic plateau during austral summer (December, January, February; DJF), and mostly cooling for the other seasons. The strongest cooling in their analysis occurs in autumn (March, April, May; MAM), even though cooling also seems to occur in winter (June, July, August; JJA) and spring (September, October, November; SON). This is somewhat similar to Steig et al.'s findings: Even though they report an overall warming trend in East Antarctica, their results for autumn also show slight cooling.

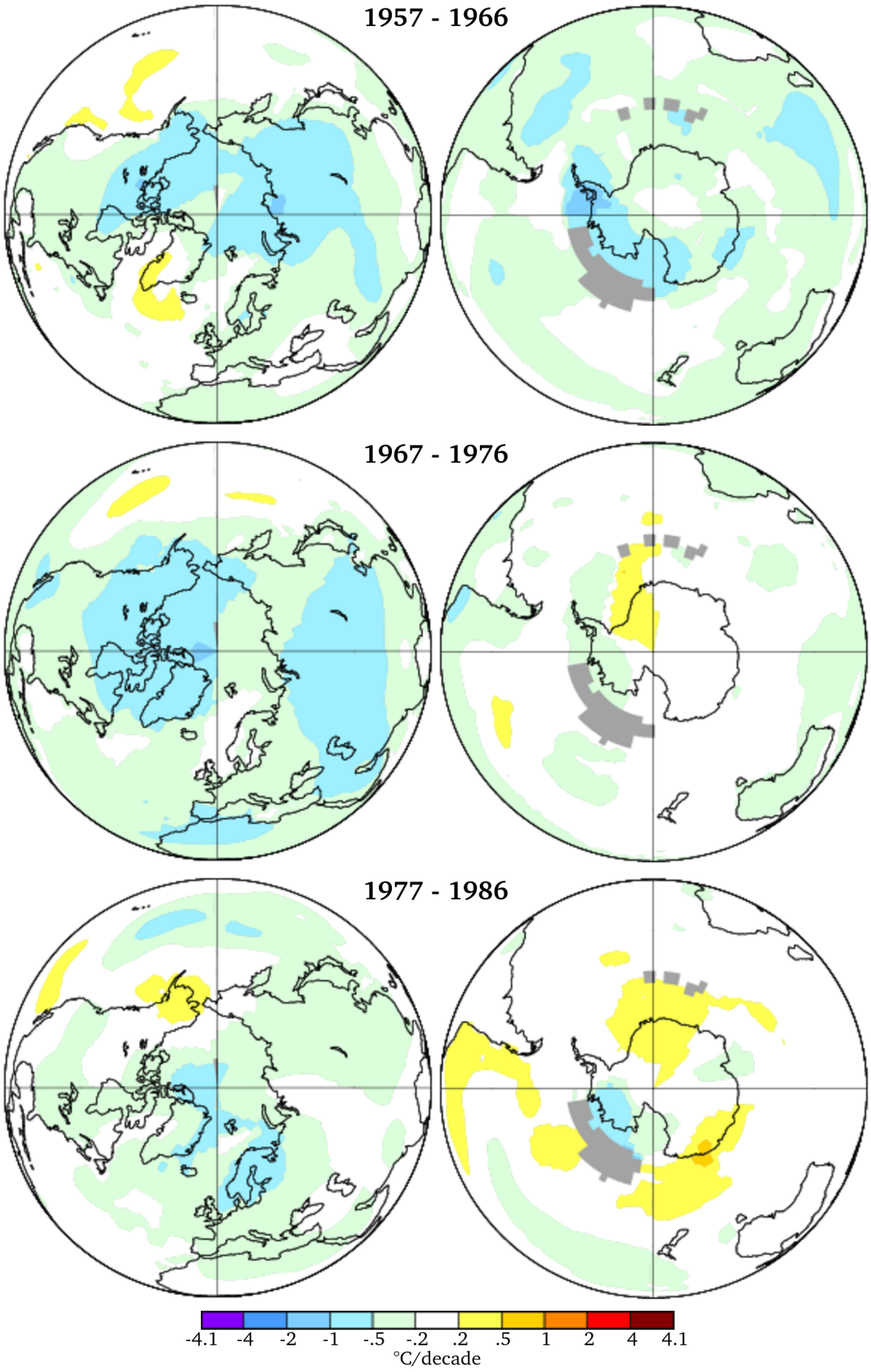

Figure 1.10: *Decadal surface air temperature anomalies from the GISTEMP analysis. The reference period for the anomalies shown is 1957 - 2013. Note that negative anomalies during the first half of the reference period indicate warming over the entire period, positive anomalies cooling. Grey shading denotes data void areas. The individual maps were created using the GISS's web-interface (Schmunk 2014).*

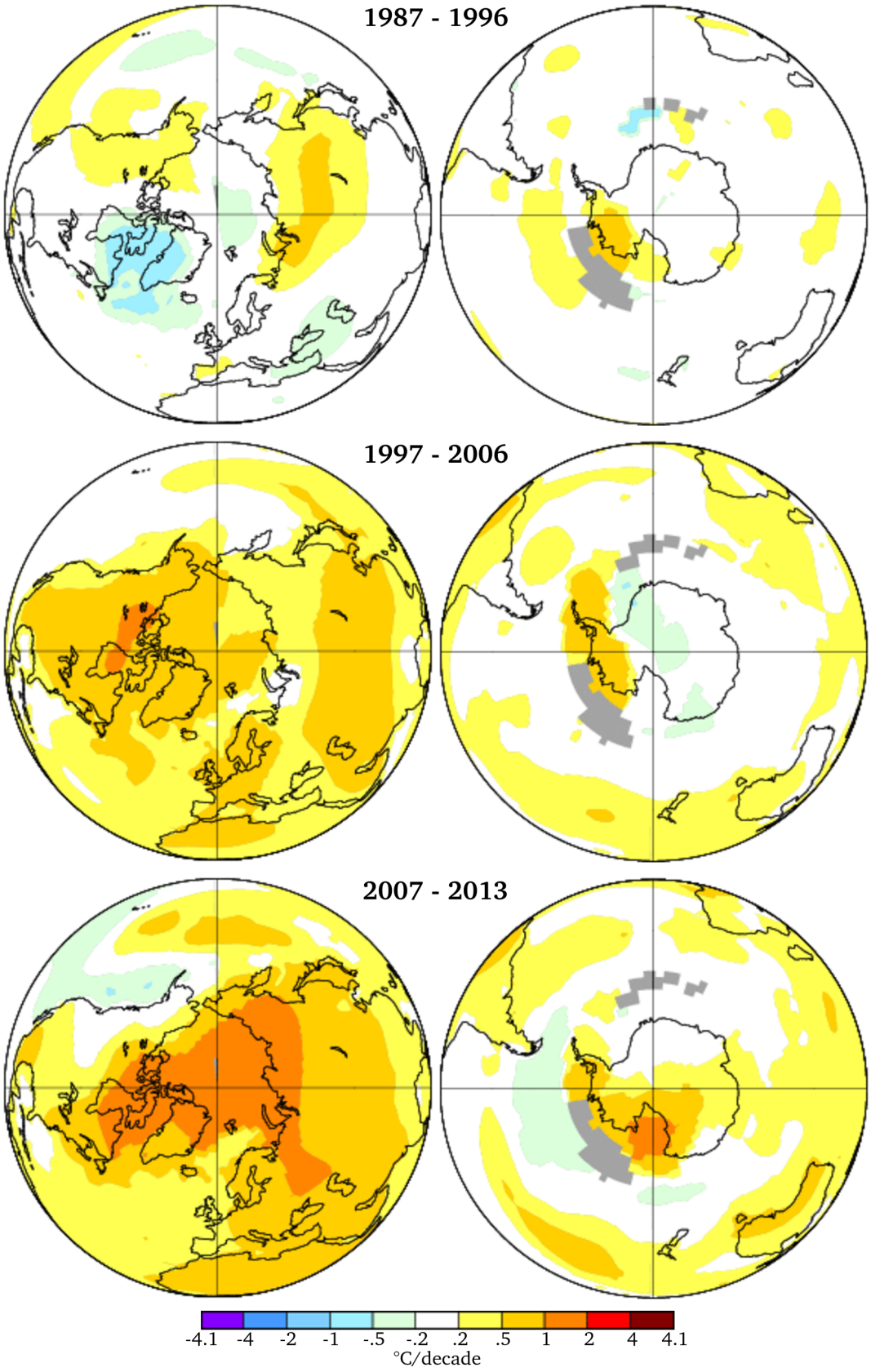

Figure 1.11: *Decadal surface air temperature anomalies from the GISTEMP analysis. The reference period for the anomalies shown is 1957 - 2013. Note that positive anomalies during the second half of the reference period indicate warming over the entire period, negative anomalies cooling. Grey shading denotes data void areas. The individual maps were created using the GISS's web-interface (Schmunk 2014).*

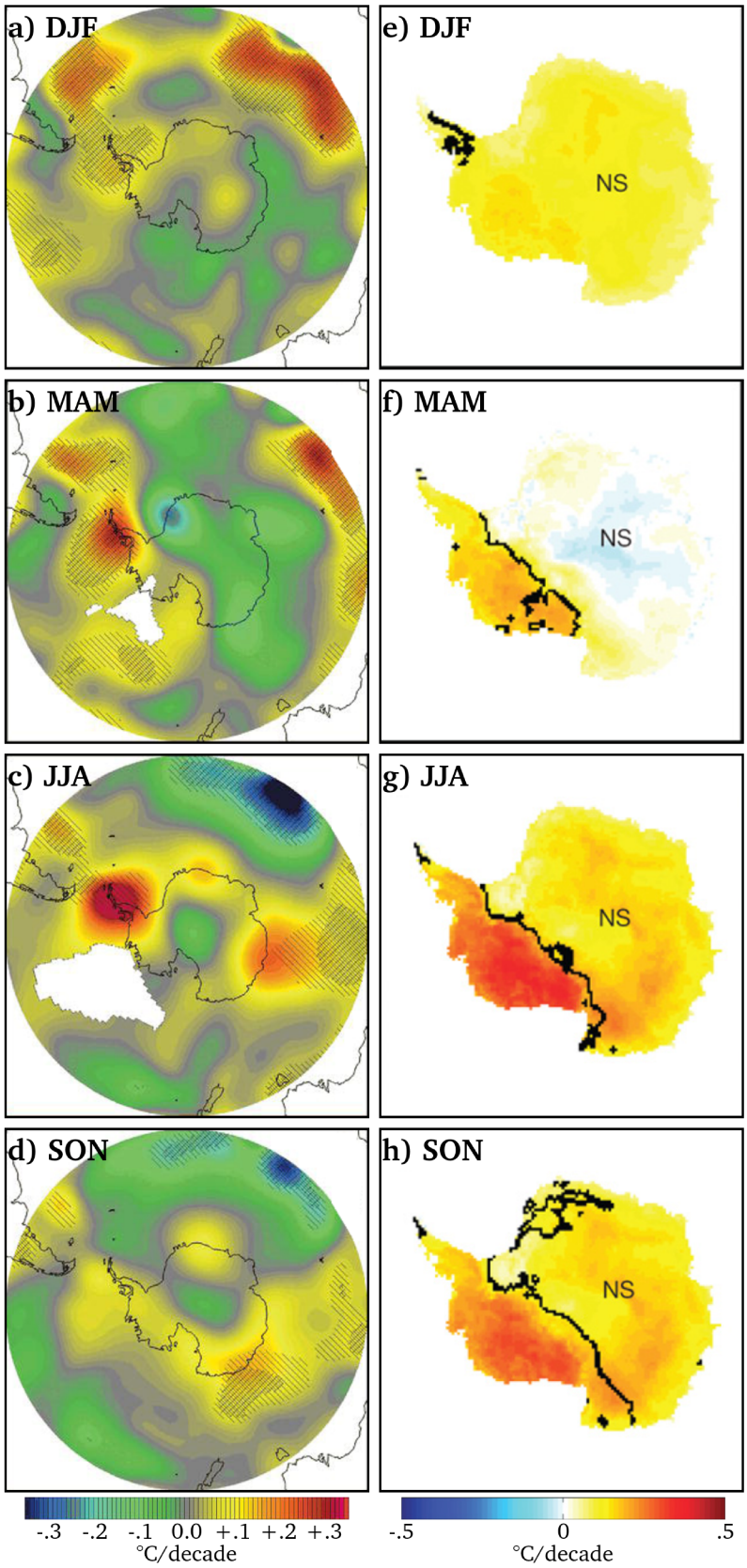

Figure 1.12: *Linear trends of seasonal mean surface temperature:* ***a-d)*** *Analysis from Chapman and Walsh (2007). Single hatching denotes statistical significance on the 95 % level, cross-hatching 99%. The panels have been rotated by 90° for better comparison.* ***e-h)*** *Results from Steig et al. (2009). Regions with significant trends (95 % level) are confined by black contour lines; non-significant trends are labelled "NS". (Reprinted by permission from Macmillan Publishers Ltd: Nature, Steig et al. 2009, copyright 2009)*

1.6 Current explanations of the non-warming of central Antarctica

Current explanations for the non-warming of Eastern Antarctica focus on dynamic aspects. Many publications (IPCC 2013, chapter 10.3.3.3 and 14.5.2 and references herein) regard the depletion of ozone in the southern hemisphere (Thompson et al. 2011) as well as increasing well-mixed greenhouse gases (Langematz 2003; Shindell 2004) and also increasing stratospheric water vapour (Forster and Shine 1999) as actual cause. All these changes induce a cooling of the stratosphere, particularly at high latitudes. Therefore, baroclinicity in the hemisphere increases, which in turn enhances the polar vortex. This alteration of the dynamics in the southern hemisphere causes a reduced heat transport towards the South Pole, resulting in a cooling of the Antarctic atmosphere.

This change in the atmospheric circulation of the southern hemisphere is commonly described by what is known as *Southern Annular Mode* (SAM). There are multiple definitions for the associated climate index; three common ones were formulated by Thompson and Wallace (2000), Nan and Li (2003) and by Marshall (2003) (see also IPCC 2013, box 2.5). The work of Marshall, for instance, defines the SAM index as the difference in normalised zonal mean sea level pressure at 40°S and 65°S, calculated from station records of the period 1958 - 2000. Positive values of SAM indicate large pressure differences between these two latitudes, while a negative index implies a rather small meridional surface pressure gradient. During the last decades, the SAM has been in its positive phase (IPCC 2013, chapter 14.5.2), which is associated with a comparable strong circumpolar vortex, and hence with an increased insulation of central Antarctica (Thompson and Solomon 2002).

Chapter 2: A theory why central Antarctica is currently not warming

2.1 Objectives and content of the thesis

Prerequisites

Thermal infrared radiation is the physical phenomenon that the Earth utilises to compensate for the energy received by the sun. The entire surface of the planet emits thermal radiation into space. However, the surface emission is hampered on its way through the atmosphere: Parts of the electromagnetic spectrum are absorbed, and according to Kirchhoff's law, reemitted. This is, what is commonly called *greenhouse effect*.

The greenhouse effect typically causes the emission into space to be less than what has been emitted by the underlying surface. This reduction in outgoing radiation occurs at specific wavelengths: the absorption bands of the greenhouse gases.

A typical top of atmosphere thermal emission spectrum is shown in figure 2.1a, along with the black body surface emission. Absorption bands of greenhouse gases are visible as local emission minima in the spectrum. The reason for the spectral radiance, which is emitted to space, being less than the surface emission is the atmospheric temperature profile: Typically, the surface is the warmest point in the profile as there most of the solar radiation is absorbed. Hence, the emitted spectral radiance from the surface exceeds the emission from the atmosphere itself.

Panels c)-g) of figure 2.1 give the transmittance through the atmosphere for the five most important greenhouse gases. From that, one can attribute the minima in the emission spectrum shown in panel a) to the various gases: The minimum from 5 µm to 8 µm is mainly caused by water, methane and nitrous oxide; ozone acts between 9 µm and 10 µm; carbon dioxide is the main species causing the minimum between 13 µm and 18 µm; and water causes the greenhouse effect for longer wavelengths.

Observations show, that emission spectra at the top of the atmosphere over the high altitude Antarctic plateau can look opposite to what is typically observed over the rest of the planet: Thermal emission in the absorption bands of GHGs may exceed the surface emission. Figure 2.1b shows such a spectrum: It features local maxima, where typically local minima are observed.

Hypotheses behind the thesis

The occurrence of emission maxima at TOA in the absorption bands of GHGs means, that, from a top of atmosphere perspective, the presence of GHGs causes a surplus of energy loss into space. Taking the difference between surface and TOA emission as greenhouse effect, this yields a negative GHE being observed over Antarctica. Furthermore, when considering increasing concentrations of GHGs, particularly CO_2, this phenomenon should yield an increase in thermal emission. This is opposite to what is generally known to result from increasing concentrations of GHGs.

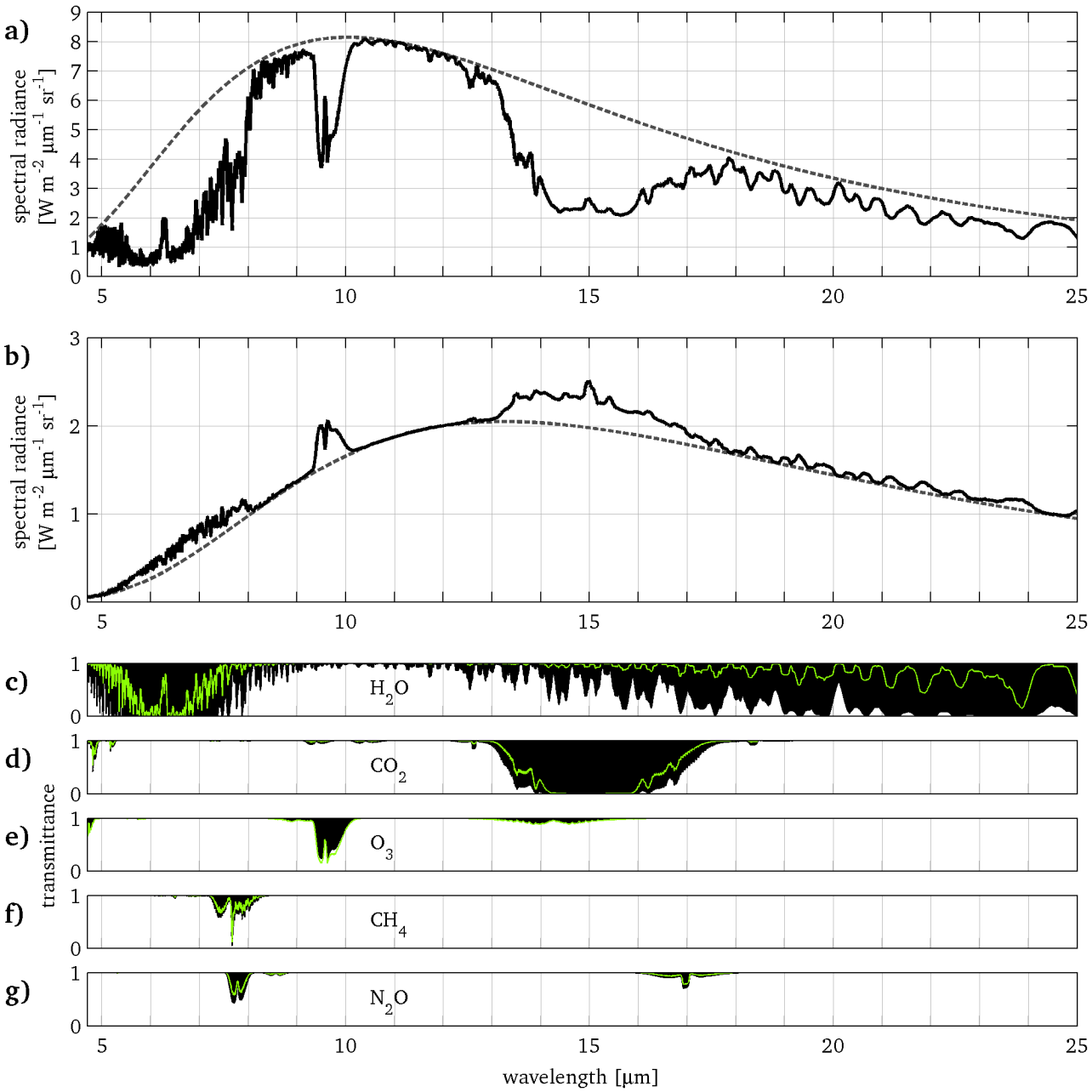

***Figure 2.1**: **a)** Typical thermal emission spectrum at the top of atmosphere (solid line) and black body surface emission of 15°C (dashed line). The spectrum was calculated with the line-by-line model ALFIP (see section 2.4) for the US Standard Atmosphere (1976). **b)** Thermal emission spectrum over the Antarctic ice sheet (solid line) and black body surface emission of -54°C (dashed line). The spectrum was calculated with the line-by-line model ALFIP for typical south polar conditions in March. **c-g)** Atmospheric transmittance of the five most important greenhouse gases: water, carbon dioxide, ozone, methane and nitrous oxide. The black patches show the transmittance as calculated with ALFIP for the emission spectrum in panel a), while the green lines were calculated for the Antarctic conditions shown in panel b).*

In section 1.5 it has been demonstrated, that global warming during the last decades has not been proven to occur over the highest elevated areas of Antarctica. There are even indications, that parts of the continent might have experienced slight cooling. One cause of this non-warming might be the inverted effect of GHGs on the long-wave radiative emission to space over central Antarctica.

Key questions to be addressed by this work

In order to examine above hypotheses, the following key questions are investigated in this work, focusing on the greenhouse gas CO_2:

1. How frequent do thermal emission spectra with local emission maxima in the absorption bands of greenhouse gases occur?

2. Is the interior of the Antarctic continent the only place on the planet where a negative GHE is observed?

3. In areas, where the GHE is negative, how does the TOA thermal emission respond to changes in the concentration of GHGs? Can increasing GHGs cause a regional cooling of the Earth-atmosphere system?

Methods to be used

Above *QUESTION 1* is answered from satellite observations of thermal emission spectra. At least one year of observations is required, in order to evaluate whether the phenomenon is of climatic relevance. A region with negative yearly averaged GHE is assumed to be relevant for the local climate. The question is also addressed with line-by-line radiative transfer calculations for typical Antarctic conditions. This reproduces observed local emission maxima in the absorption bands of GHGs. General circulation models (GCMs) should incorporate a negative GHE already, if the according radiation scheme allows for this. As GCMs typically only output spectrally integrated radiation quantities, the spectral characteristic behind the phenomenon is not seen from this type of data. Theoretical considerations using a simple two layer model also give some insight into the phenomenon of negative GHE.

QUESTION 2 is also answered from one year of satellite observed thermal emission spectra covering the entire globe. If the phenomenon occurs only sporadically, yearly averages of the GHE will show positive values all over the Earth.

QUESTION 3 could be answered from long records of comparable satellite observations of thermal emission spectra. The atmospheric CO_2 concentration has risen by more than 15 % since satellites have observed the Earth's radiation for the first time, more than three decades ago. However, this approach is tedious, and the increased CO_2 is not the only change the atmosphere has undergone. Hence, the local change in TOA thermal emission might be superseded by other changes. Here, the easier modelling approach is taken to analyse the change in TOA long-wave emission caused by increasing CO_2. Again, two layer model considerations are presented, line-by-line radiative transfer calculations, and results from GCM analyses.

2.2 Top of atmosphere measurements

2.2.1 Quantification of greenhouse effect from satellite

In AR5 (IPCC 2013, annex III, page 1455) the *greenhouse effect* is defined as follows:

> *"***Greenhouse effect** *The infrared radiative effect of all infrared-absorbing constituents in the atmosphere. [...]"*

with *radiative effect* being defined as (IPCC 2013, annex III, page 1460):

> *"***Radiative effect** *The impact on a radiation flux [...] caused by the interaction of a particular constituent with either the infrared or solar radiation fields through absorption, scattering and emission, relative to an otherwise identical atmosphere free of that constituent. This quantifies the impact of the constituent on the climate system. [...]"*

Following these definitions, the *GHE of a particular constituent* can be defined as:

> **GHE of a particular constituent** The impact on a radiation flux caused by the interaction of this particular constituent with the infrared radiation field through absorption, scattering and emission, relative to an otherwise identical atmosphere free of that constituent.

Above definitions of the GHE do not refine the infrared radiation fluxes to be considered. Particularly, they do not define the altitude level of the fluxes. In order to determine the overall effect of greenhouse gases on the climate system, it seems obvious to look at the flux at the top of atmosphere.

Hence, the *GHE of CO_2* can be mathematically defined as

$$G_{CO_2} = \int_{\lambda_0}^{\infty} [F_{\lambda,TOA}(c=0) - F_{\lambda,TOA}(c)]\, d\lambda \tag{2.1}$$

with $F_{\lambda,TOA}$ being the spectral irradiance emitted to space as a function of CO_2 concentration c. λ_0 denotes the wavelength which separates the solar and terrestrial spectra. For the calculations performed here, a value of λ_0 = 4.7 µm is used. This choice is justified in section 1.2, figure 1.3. To illustrate the above equation, figure 2.2 shows example spectra of $F_{\lambda,TOA}$.

Effectively, the GHE of CO_2 , as considered here, is the difference in the outgoing long-wave radiation to what would be emitted, if suddenly there was no CO_2. Obviously, this definition omits any feedback mechanism that the sudden absence of CO_2 would have. This approach is quite similar to the concept described by Thomas and Stamnes (1999): They define the GHE to be the difference between the radiation emitted by the surface and the TOA flux. Essentially, this results in different quantifications when clouds are present: Equation 2.1 then uses the long-wave emission from the cloud's top, whereas the definition of Thomas and Stamnes always uses the surface emission.

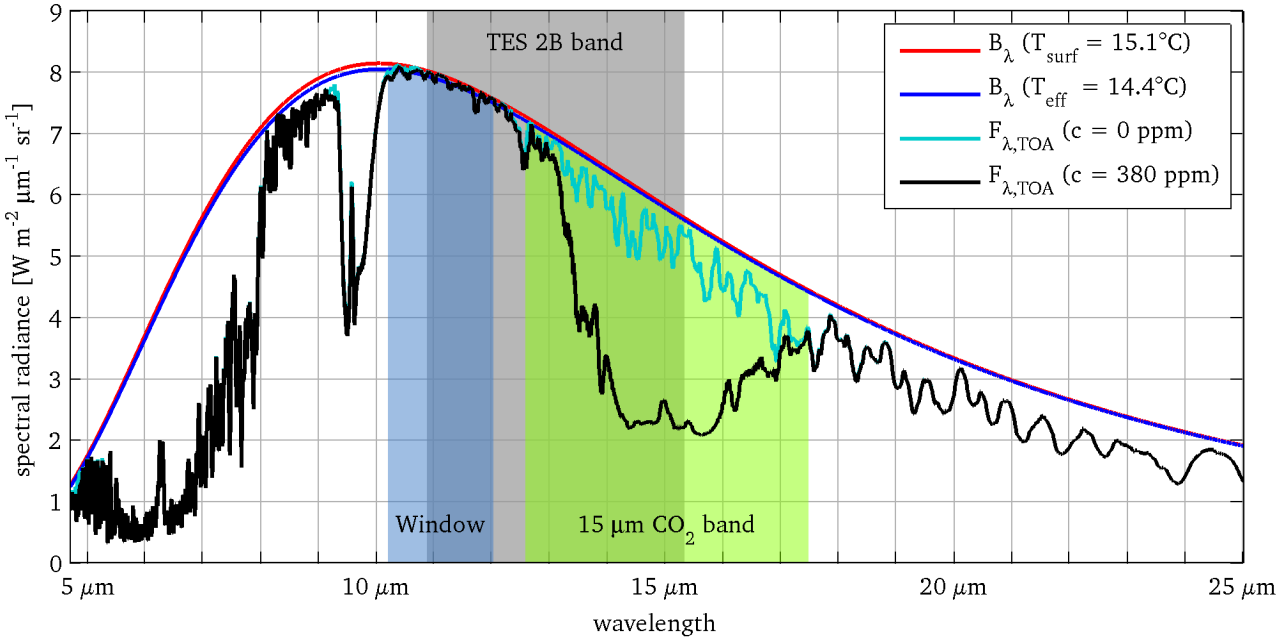

***Figure 2.2**: Examples of TOA emission as used in equation 2.1 calculated with the radiative transfer model ALFIP (see section 2.4). Spectral ranges that are relevant for the calculation of the GHE of CO_2 are indicated by coloured patches. The surface emission that was used to calculate the spectra is plotted in red, whereas the blue line indicates the black body spectral radiance corresponding to the effective temperature in the window region of the emission spectrum.*

In order to determine G_{CO2} (equation 2.1) from measurements, one needs to quantify the two terms $F_{\lambda,TOA}(0)$ and $F_{\lambda,TOA}(c)$. The latter is not much of an issue, it can easily be derived from satellite measurements. The trouble with equation 2.1 is, that $F_{\lambda,TOA}(0)$ is a hypothetical quantity and cannot be measured. Consequently, it needs to be approximated somehow.

Satellite observations of long-wave emission spectra $F_{\lambda,sat}$ can be used to quantify the TOA emission into space:

$$F_{\lambda,TOA}(c) = a \cdot F_{\lambda,sat} \tag{2.2}$$

The attenuation a accounts for the height of the satellite above the Earth:

$$a = \frac{(r_{earth} + h_{sat} - h_{TOA})^2}{r_{earth}^2}, \tag{2.3}$$

where r_{earth} = 6371 km is the mean radius of the Earth, h_{sat} the altitude of the satellite and h_{TOA} the altitude of the top of the atmosphere. The latter is taken to be at 80 km. This value was determined from an experiment with the line-by-line radiative transfer model ALFIP (see section 2.4): The model was run to calculate the TOA emission, while the model atmosphere was cut at a certain altitude, leaving only the lower layers. Figure 2.3 shows the result: Down to 80 km altitude the TOA emission remains virtually constant. Going further down causes the hypothetical TOA emission to increase slightly, due to the warmer uppermost layers of these model configurations. From the stratopause downwards, TOA emission decreases because of the inverted temperature gradient in the stratosphere. At about 30 km the minimum is reached: From here on, the warm troposphere and surface dominates the TOA emission.

The spectral irradiance of a CO_2-free atmosphere $F_{\lambda,TOA}(0)$ cannot be measured. However, it can be approximated by assuming black body emission from the emitting surface, and assuming that the absorption bands of CO_2 do not overlap greatly with absorption bands of other greenhouse gases. If then, the temperature of the emitting surface T_{surf} (i.e. the Earth's surface or the top of clouds) is known, one can estimate the spectral irradiance for no CO_2 using the Planck-function B_λ:

$$F_{\lambda,TOA}(0) = \pi B_\lambda(T_{surf}) \tag{2.4}$$

T_{surf} can be derived from irradiance measurements in an atmospheric window. This is done by using the effective temperature of the observed spectral irradiance in a window region T_{eff}:

$$T_{surf} = T_{eff} \tag{2.5}$$

where T_{eff} is defined by the integrals over the spectral window between $\lambda_{w,min}$ and $\lambda_{w,max}$ (see also figure 2.2):

$$\int_{\lambda_{w,min}}^{\lambda_{w,max}} \pi B_\lambda(T_{eff})\ d\lambda = \int_{\lambda_{w,min}}^{\lambda_{w,max}} a \cdot F_{\lambda,sat}\ d\lambda \tag{2.6}$$

This requires, that the satellite sensor covers an atmospheric window, where (virtually) no absorption and no emission occurs. The expression cannot be rearranged to have T_{eff} on one side, and some straight forward definition on the other side. Therefore, in practice, equation 2.6 is solved iteratively for T_{eff}.

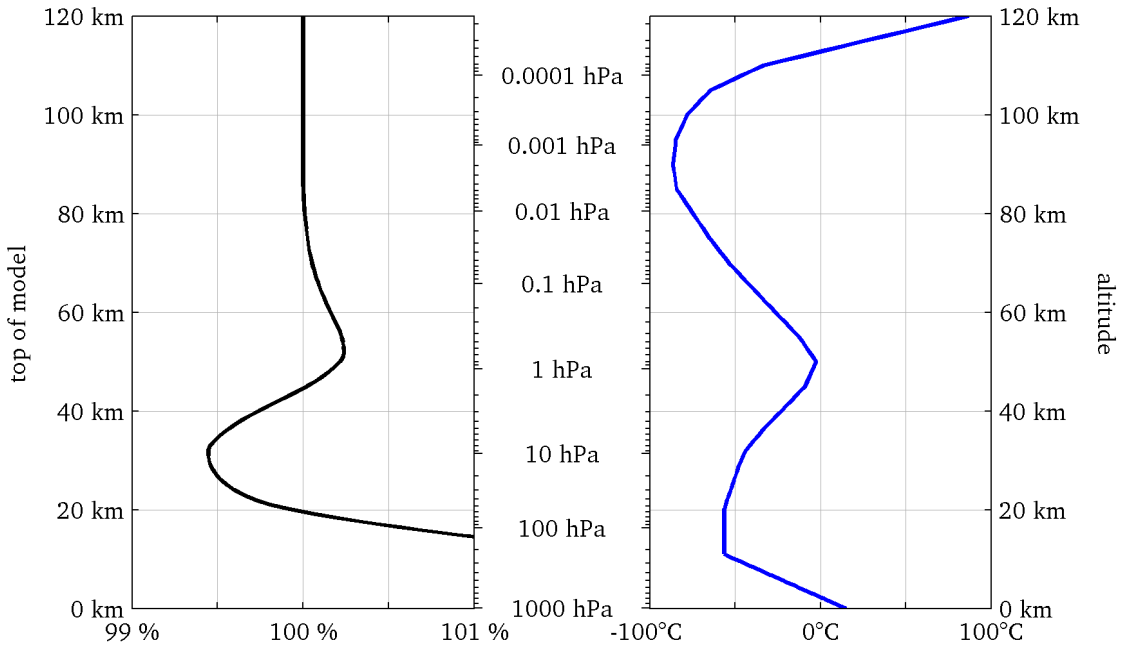

***Figure 2.3**: **Left panel:** Top of atmosphere long-wave emission for different top of model altitudes. This was calculated with the line-by-line model ALFIP (see section 2.4) for the US Standard Atmosphere (1976) and the five most important greenhouse gases (H_2O, CO_2, O_3, CH_4 and N2O). All values are normalised with the emission of a 120 km atmosphere. The curve reaches 140 % at the surface. **Right panel:** The US Standard Atmosphere (1976) temperature profile.*

Equation 2.1 can now be rewritten, to determine the GHE of CO_2 from satellite observed thermal infrared spectra between λ_{min} and λ_{max}:

$$G_{CO_2} = \int_{\lambda_{min}}^{\lambda_{max}} [\pi B_\lambda(T_{eff}) - a \cdot F_{\lambda,sat}] \, d\lambda \tag{2.7}$$

with T_{eff} given by equation 2.6. In terms of wave numbers ν, the above equation reads:

$$G_{CO_2} = \int_{\nu_{min}}^{\nu_{max}} [\pi B_\nu(T_{eff}) - a \cdot F_{\nu,sat}] \, d\nu \tag{2.8}$$

2.2.2 Sensor used: Tropospheric Emission Spectrometer (TES)

The satellite instrument used for this work is the Tropospheric Emission Spectrometer (TES) (Beer et al. 2001) onboard the satellite Aura, which was developed and is operated by the National Aeronautics and Space Administration (NASA). The satellite was launched 2004-07-15 into a sun-synchronous, near polar orbit of 98.2° inclination. Aura orbits the Earth at an altitude of some 705 km, with a repeat cycle of 16 days and 233 orbits per cycle, corresponding to nearly 100 minutes per orbit. The ascending node (the satellite flying northward) is in daylight (crossing of the equator at approximately 13:45 o'clock), whereas in the descending node the satellite sees the Earth at nighttime (Douglass and Brill 2014). Due to the sun-synchronous orbit, the instrument lacks observations north and south of 82° latitude.

The TES instrument is an imaging infrared Fourier-transform spectrometer, which was build for NASA by the Jet Propulsion Laboratory, California Institute of Technology. It features four 1-by-16 pixel detectors, each equipped with a characteristic spectral filter covering wavelengths between 4.44 µm and 15.34 µm. The detector that covers most of the main CO_2 absorption band, namely *filter 2B*, detects infrared radiation between λ_{min} = 10.88 µm (919 cm^{-1}) and λ_{max} = 15.34 µm (652 cm^{-1}) (see figure 2.2). Therefore, only data from this detector are used here. The spectral accuracy is rated to be ±0.00025 cm^{-1}, which corresponds to 0.0030 nm for the lower wavelengths and 0.0059 nm for the upper limit of the filter. The spectral resolution of filter 2B is 0.06 cm^{-1}, which translates to 0.7 nm for the shortest wavelengths transmitted through the filter, and 1.4 nm for the longest wavelengths. The spacial resolution of the *Global Survey Mode*, which is used here, is 0.5 km by 5.3 km per pixel at nadir. The 16 pixels are lined up along the flight path, resulting in a spacial coverage over areas at sea level of 5.3 km by 8.5 km. The radiometric accuracy is specified to be smaller than 1 K in brightness temperature (Beer et al. 2001).

The acquisition cycle of TES is set up to perform a *Global Survey* approximately every second day. A Global Survey consists of 16 orbits and takes some 26 hours to be completed. Observations of one survey do not cover the entire globe, as the footprint of one observation is some 45 km^2 and the distance between two observations is about 185 km along the flight path. The observed spots alter with every orbit, revisiting the same spots every 16 days. The first global survey was carried out in September 2004. In June 2005 no global survey was acquired. For every month from July 2005 until December 2009 at least 9 Global Surveys are available. However, since July 2008 operation over the polar regions is discontinued in order to extend the instruments lifetime. In 2010 and 2011 about half of the months have either no or only few Global Surveys, not suitable for calculating global averages. For the time since January 2012 there is hardly any Global Survey data available (Gluck and Cosic 2014; Gluck and Cosic 2008). Due to these limitations in data availability, this work focuses on data from 2006: This year has an almost complete record of observations, which allows the reliable calculation of yearly averages.

TES data are provided, as typical for satellite data, in different stages of post-processing. From the raw *level 1A* data *level 1B* data are generated: Essentially, these are radiometrically calibrated spectra constructed from the observed interferograms. This is the stage used here to calculate the greenhouse effect. Later stages (namely *level 2* and *level 3* data) include retrieved profiles of trace gases or temperature and interpolated 3D-fields thereof. All TES data can be obtained free of charge from the NASA Langley Research Center Atmospheric Science Data Center. The web-portal https://eosweb.larc.nasa.gov/project/tes/tes_tl1bn_table offers various methods for download. For this work, data has been downloaded using the ftp access.

The data provided by NASA includes several quality assessment flags, which have been used here to filter erroneous or suspicious measurements. The flags are documented in the TES Data Products Specifications (Lewicki et al. 2009). Specifically, the following flags were used for filtering the data:

- L1A_Time_Date_Error_Occurred
- Geolocation_Failed
- L1B_General_Quality_Flag
- L1B_General_Error_Flag

The central part of the data processing is the calculation of the greenhouse effect of CO_2 (G_{CO2}). As TES L1B data files contain the spectral radiances in units of W/cm^2/sr/cm^{-1}, equation 2.8 is used for this. The spectral range is that of the 2B filter (ν_{min} = 652 cm^{-1}, ν_{max} = 919 cm^{-1}). T_{eff} is iteratively determined from equation 2.6, and α from equation 2.3. $F_{\nu,sat}$ is the actual value from the L1B file.

For the creation of maps, all calculated values of G_{CO2} of one *Global Survey* (which is associated with a specific *Run ID*) are interpolated onto a 1°-by-1° latitude-longitude grid. Averages over time are then calculated from those gridded data sets pixel by pixel.

2.2.3 Results

Figure 2.4 shows three sample spectra that were observed with the 2B-detector of the TES instrument. For each measured spectrum $F_{\lambda,sat}$ the TOA emission $F_{\lambda,TOA}$ (calculated from equation 2.2) is also shown, along with the black body emission $B_\lambda(T_{eff})$. The calculated values of the GHE of CO_2 are indicated as coloured patches. The top panel shows a typical long-wave TOA emission spectrum, with the corresponding value of G_{CO2} being comparable to that of the US Standard Atmosphere listed in table 2.1, in the column entitled $G_{CO2}(TES, T_{eff})$. The panel in the middle of figure 2.4 gives an example from the East Antarctic plateau in March: This is characterised by an already very cold surface, causing comparable low emissions in the window region, and a rather warm stratosphere, wich gives rise to the negative GHE of CO_2 throughout the entire CO_2 band. The lowermost panel depicts the situation above the Antarctic plateau in spring: The surface is still very cold, but the stratosphere is recovering from its coldest state in winter. This causes negative GHE only in those parts of the spectrum with the highest density of CO_2 absorption lines, namely around 15 µm and 13.9 µm.

The yearly averages of G_{CO2} from 2006 are illustrated in figure 2.5. The uppermost panel gives the average over all available observations from that year. The strongest GHE is evident over the tropics, with the exception of the inner-tropical convergence zone (ITCZ). This exception results from the frequent occurrence of high-reaching clouds. For most of the Antarctic plateau, G_{CO2} is close to zero or even negative. This is not seen in the Arctic: There, the GHE of CO_2 is well above

zero. However, above the Greenland ice sheet values of G_{CO2} as low as 4.3 W/m^2 are reached. The lower two panels of figure 2.5 show the yearly averages of all day- and night-time observations separately. Major differences between the two are seen over the northern part of Africa, Australia, the Tibetan plateau and Siberia. This reflects the strong continental climatic character of these regions. As for Antarctica, the difference between day and night is hardly discernible; which is not surprising for polar regions, even though the difference seems more pronounced in the Arctic, i.e. north of 60°N.

Figure 2.6 gives the zonal means of the data shown in figure 2.5. From this, a pronounced difference between the two hemispheres becomes obvious: On the one hand, there is almost no difference between day and night south of 45°S, which is not seen in the north. On the other hand, the GHE of CO_2 at the highest latitudes is lower on the southern hemisphere than it is in the north.

The global average of the GHE of CO_2 can be calculated when the data gaps at the poles are filled with estimated values. For this, a linear trend of the zonal mean from 60°N/S to the poles is assumed (see figure 2.6). This yields a globally averaged GHE of CO_2 in the spectral range of the TES instrument of 18.9 W/m^2 for 2006.

In order to evaluate the seasonality of G_{CO2}, figures 2.7 and 2.8 show the seasonal and monthly means of the 2006 TES data. In the northern hemisphere, the lowest values are observed over Greenland, with the lowest summer-value (JJA) being 5.4 W/m^2, and the lowest winter-value (DJF) being 3.0 W/m^2. Over Siberia, the situation is similar (minimum of 8.9 W/m^2 in summer and 4.0 W/m^2 in winter), even though the difference between summer and winter is not as large. Over the high-elevated areas of Antarctica (those above 2000 mASL), G_{CO2} ranges between -1.9 W/m^2 and 1.6 W/m^2 in summer (DJF), between -3.3 W/m^2 and 4.7 W/m^2 in autumn (MAM), between -0.4 W/m^2 and 6.8 W/m^2 in winter (JJA), and between -1.4 W/m^2 and 5.3 W/m^2 during spring (SON). As seen from these ranges, negative values occur quite frequently. In fact, all months but August show areas with negative GHE. The phenomenon is most pronounced in autumn with monthly averages as low as -5.0 W/m^2 in March. During this time of the year, almost the entire plateau above 3000 mASL has a greenhouse effect below zero. Slightly southeast of Dome F at 79°S, 44°E, 3630 mASL there is a small region with a negative GHE of CO_2 during all seasons (see figure 2.7).

Negative values of GHE of CO_2 over central Antarctica occur predominantly during austral autumn, because at this time of the year the surface has already cooled down almost to its winter temperature, whereas the stratosphere is still warm. More specifically, a remnant of the positive vertical temperature gradient above the tropopause typically exists until May. After that, the lower stratosphere becomes colder than the upper troposphere, resulting in a negative temperature gradient extending up to some 20 km altitude, reaching a minimum temperature typically below -90°C. Once the stratosphere is that cold, atmospheric infrared radiation emitted to space is lower than the surface emission, giving rise to a slightly positive GHE above most of the continent. In spring the stratosphere is warmed up rapidly by the absorption of ozone, while the surface has just started to recover from its winter temperature. This then causes the rather strong negative GHE seen in October. After that, the surface has warmed up, causing again slightly positive values of G_{CO2}.

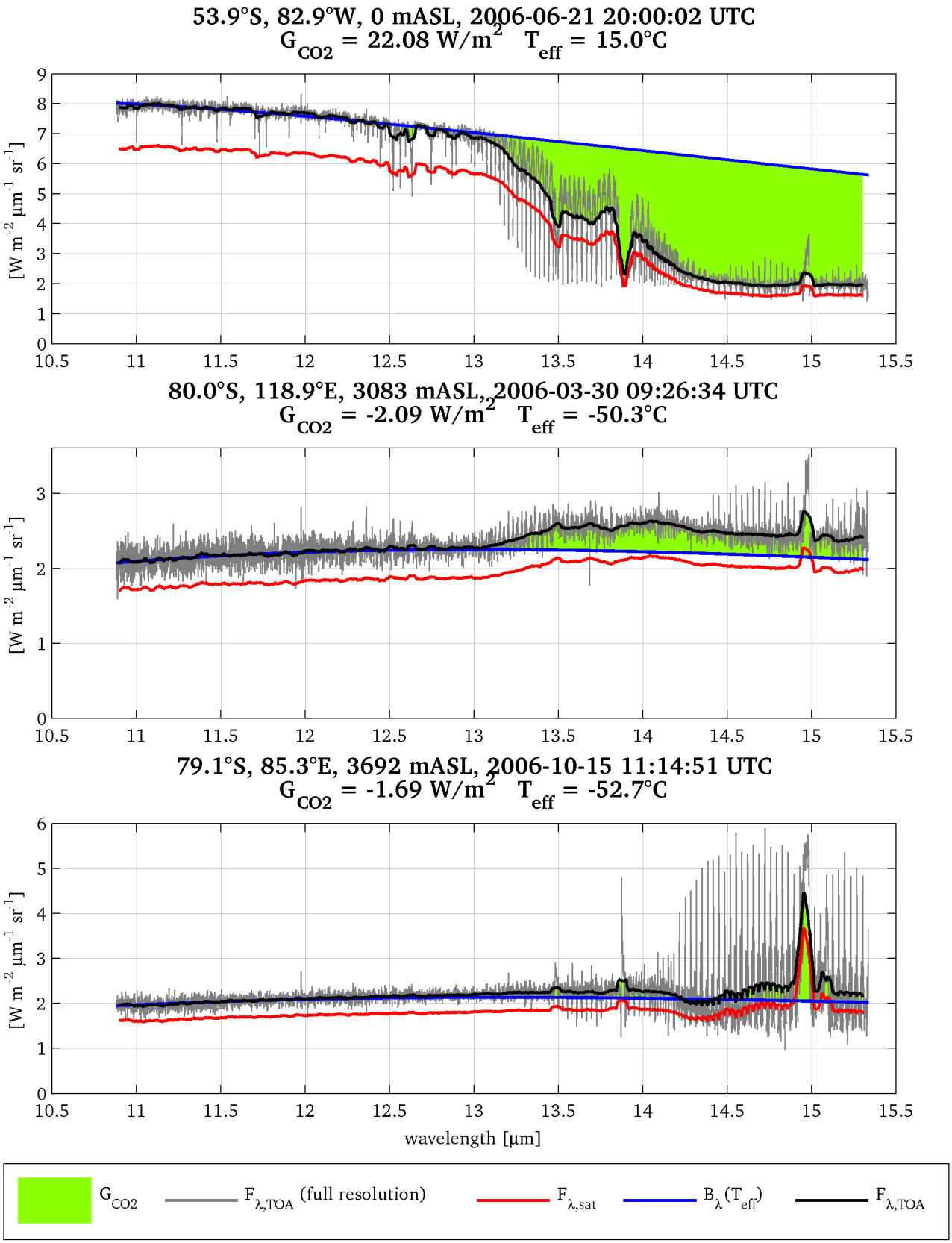

***Figure 2.4**: Three sample spectra observed by TES. The actually observed spectra (shown in red) and the derived TOA emission (black curves) are low-pass filtered for the sake of clarity. The full spectral resolution of $F_{\lambda,TOA}$ is also shown in light grey. The time and location of observation as well as the values of the derived GHE of CO_2 and the effective temperature in the window region are given in the titles.*

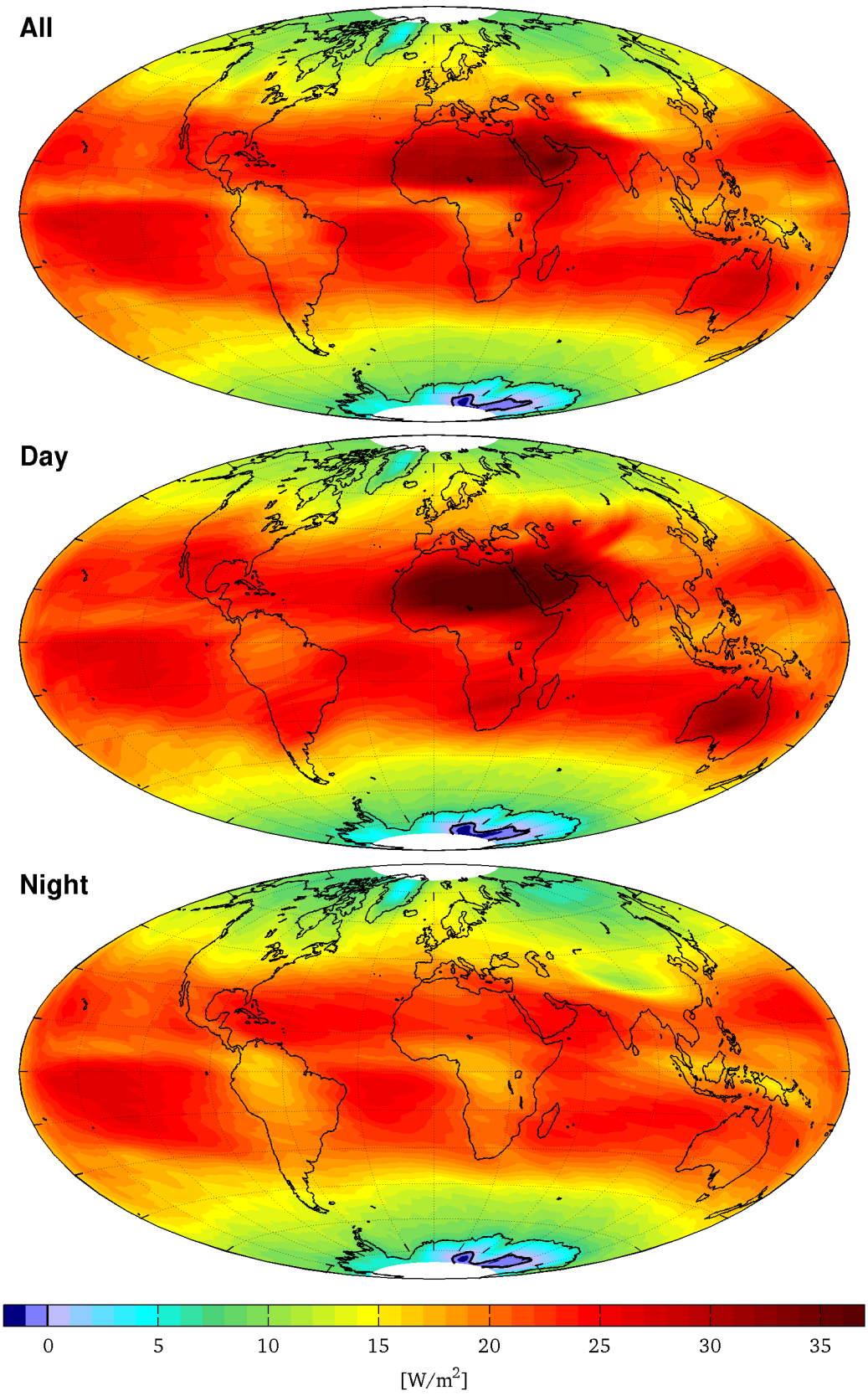

***Figure 2.5**: Yearly averaged greenhouse effect of CO_2 in 2006, calculated from TES spectra. The **All** panel comprises 545203 observed spectra from 165 global surveys. The panel **Day** shows the average over the 275317 observations acquired at daytime, while **Night** is the compilation of the remaining 269886 night-time measurements. The orbit of the satellite does not allow data acquisition right at the poles. The black contour line over Antarctica denotes 0 W/m^2.*

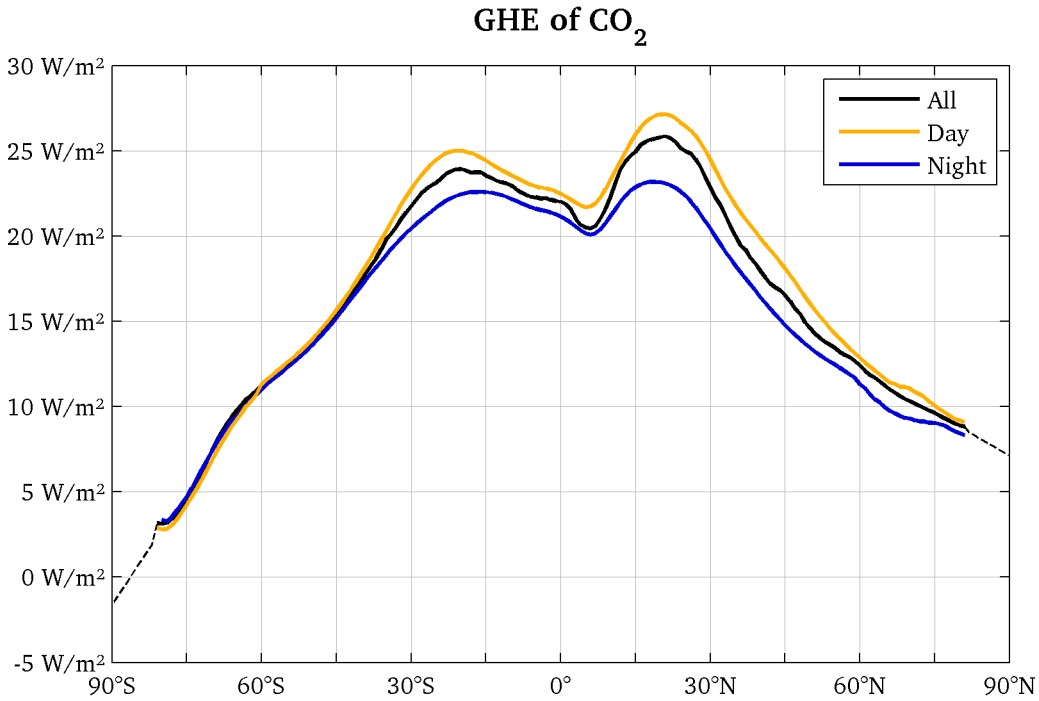

***Figure 2.6**: Zonal mean of the yearly averaged GHE of CO_2 for all, day- and night-time observations. The dataset shown is the same as in figure 2.5. The dashed line is the linear interpolation of the* All *line from 60°N/S towards the poles.*

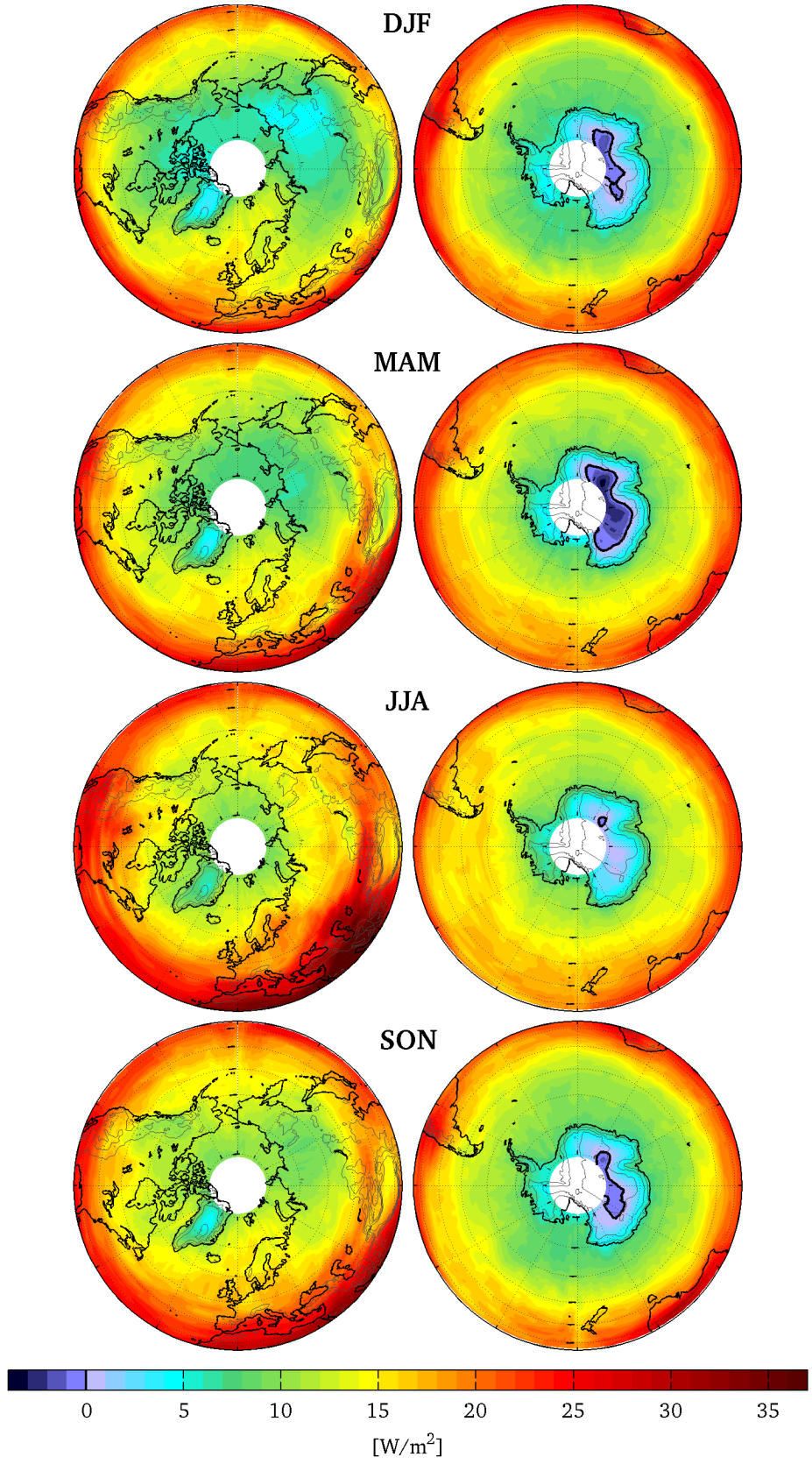

***Figure 2.7**: Seasonally averaged greenhouse effect of CO_2 in 2006, calculated from TES spectra. Each seasonal average comprises between 112494 (DJF) and 154195 (MAM) observed spectra from 36 to 46 global surveys per season. The black contour lines denote 0 W/m². Surface elevation contour lines are shown in 1000 m intervals.*

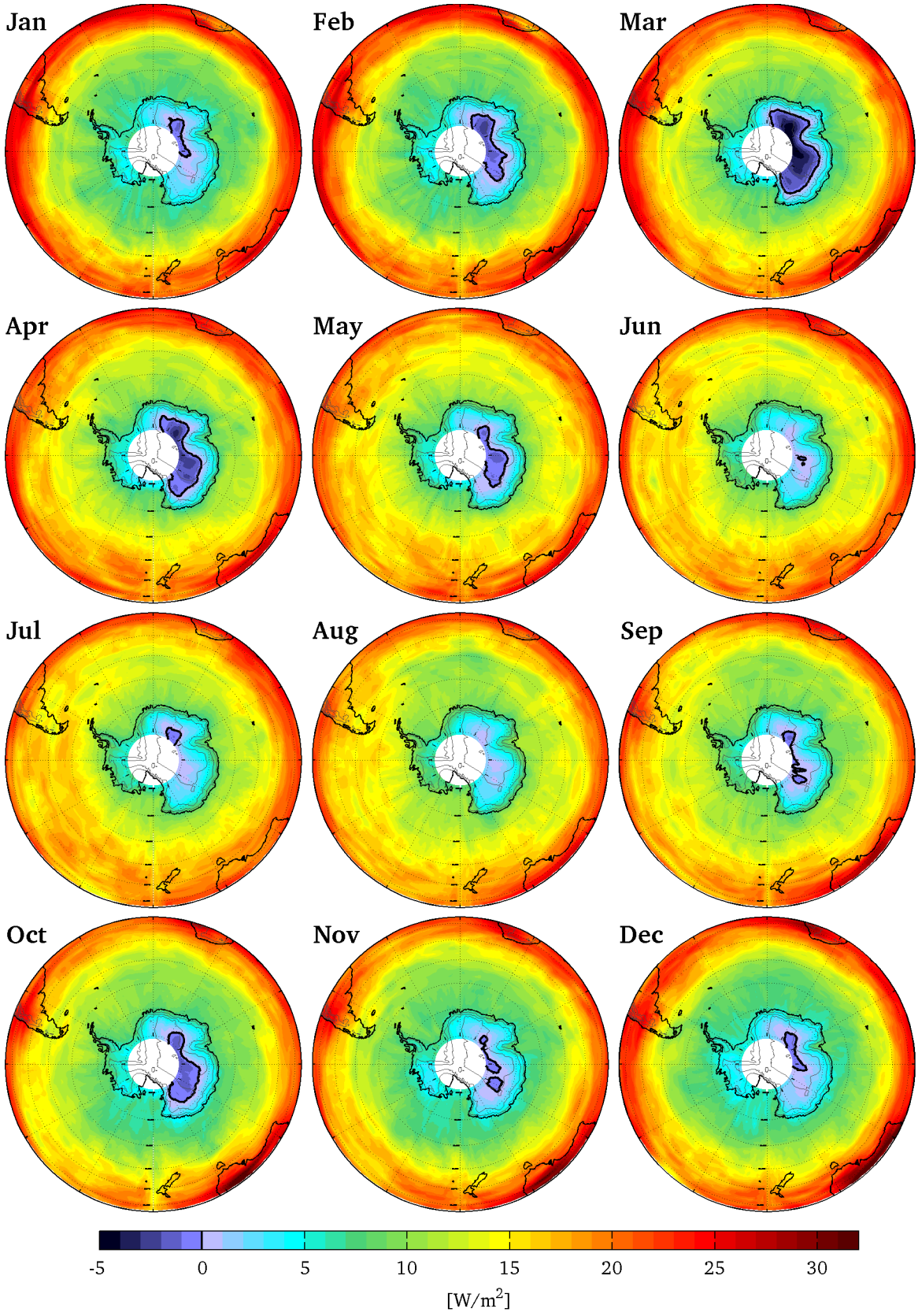

Figure 2.8: *Monthly averaged greenhouse effect of CO_2 in 2006, calculated from TES spectra. Each monthly average comprises between 20021 (Feb) and 52336 (Jul) observed spectra from 6 to 16 global surveys per month. The black contour lines denote 0 W/m^2. Surface elevation contour lines are shown in 1000 m intervals.*

2.2.4 Discussion

Methodology

For the calculation of G_{CO2} according to equation 2.8 the following assumptions and prerequisites need to be fulfilled:

1. The Earth's surface and clouds emit blackbody radiation according to Plack's law
2. The observed spectra cover an atmospheric window, where no absorption by GHGs occurs
3. The observed spectra cover the gross of all absorption bands of CO_2
4. Spectral overlap with absorption bands of other GHGs can be neglected

Water in its liquid and solid phase is very close to a black body in the thermal infrared (Hori et al. 2006). Therefore, assumption 1 is reasonable, as most of the planet's surface is either water, water-rich material (i.e. vegetation), or ice. Additionally, this work is mostly concerned with Antarctica, which is almost entirely ice-covered. The assumption also holds for sufficiently thick clouds: Long-wave emission from their top is nearly that of a black body (Allen 1971; Griffith et al. 1980). Thin clouds can have emissivity values right down to zero, but in this case the transmissivity of the cloud is greater than zero. Hence, the radiation seen by the satellite is a mixture of the cloud and surface emissions.

The validity of points 2 - 4 can be evaluated with the help of modelled emission spectra. These were calculated for the US Standard Atmosphere (1976) and typical South Pole conditions using the ALFIP model (see section 2.4). Table 2.1 shows resulting values of the greenhouse effect. The column entitled G_{CO2} is considered the “true” GHE of CO_2, as it was calculated from the mathematical definition (equation 2.1) for the entire spectrum from 4.7 µm to 200 µm. The other columns list the estimates calculated from a limited spectral range and using different reference spectra (see also figure 2.2). Some columns include percentages greater than 100 %. This means, that parts of the according spectrum have positive contributions to the GHE, while other spectral regions contribute negatively. As only some parts of the spectrum are considered, it can be that

Table 2.1: *Modelled greenhouse effect of CO_2 calculated using different formulae and for different atmospheric conditions. The column **G_{CO2}** was calculated from the full spectra for $c = 0$ ppm and $c = 380$ ppm (equation 2.1). Column **G_{CO2}(15µm-band)** uses the same spectra, but only the spectral range of the main CO_2 absorption band around 15 µm (12.58 µm to 17.48 µm). Similar to that is **G_{CO2}(TES)**, which uses the spectral range of the TES instrument (10.88 µm to 15.34 µm). The last two columns **$G_{CO2}(T_{surf})$** and **$G_{CO2}(T_{eff})$** were calculated using equation 2.7 with the actual surface temperature T_{surf} and the effective temperature T_{eff} (equation 2.6) respectively. **US Standard** refers to the US Standard Atmosphere (1976), the **South Pole** profiles are described in detail in sections 2.4.3 and 2.4.4. The percent-values denote the fraction of the value in the G_{CO2} column. Figure 2.2 illustrates the spectral bands and reference spectra which were used for the calculations.*

	G_{CO2} [W/m²]	G_{CO2}(15µm-band) [W/m²]	G_{CO2}(TES) [W/m²]	$G_{CO2}(T_{surf})$ [W/m²]	$G_{CO2}(T_{eff})$ [W/m²]
US Standard	28.10	27.55 (98 %)	17.93 (64 %)	22.35 (80 %)	21.86 (78 %)
South Pole March	-2.94	-2.90 (99 %)	-1.82 (62 %)	-2.15 (73 %)	-2.14 (73 %)
South Pole June	2.03	2.05 (101 %)	1.45 (72 %)	1.54 (76 %)	1.55 (76 %)
South Pole October	-0.83	-0.77 (93 %)	-0.79 (95 %)	-1.20 (145 %)	-1.19 (144 %)
South Pole December	3.40	3.38 (99 %)	1.71 (50 %)	1.80 (53 %)	1.80 (53 %)

compensating effects occurring for the values listed under G_{CO2} do not occur for that particular spectrally limited estimate of the GHE of CO_2.

For all atmospheric conditions listed in table 2.1, prerequisite 2 is well fulfilled, particularly for central Antarctica. This can be seen by comparing the two columns $G_{CO2}(TES, T_{surf})$ and $G_{CO2}(TES, T_{eff})$: Both columns consider only the spectral range covered by the TES sensor, but use the actual surface temperature and the effective temperature in the window respectively. The resulting values for the GHE of CO_2 are quite similar, even though $G_{CO2}(TES, T_{eff})$ is two percent less than $G_{CO2}(TES, T_{surf})$ for the US Standard Atmosphere (1976). Hence, absorption in the atmospheric window influences T_{eff} only slightly; T_{surf} is well approximated.

The validity of assumption 3 can be quantified from the columns $G_{CO2}(15\mu m\text{-}band)$ and $G_{CO2}(TES)$: Even though the 15 µm CO_2 band causes nearly the entire GHE of CO_2 (98 % for the US Standard Atmosphere), the spectral limitations of the TES instrument cause a substantial underestimation of the GHE. For the US Standard Atmosphere (1976) 64 % are covered, whereas for typical South Pole conditions it can be as little as 50 %, but not more than 1.69 W/m^2.

Addressing assumption 4, the spectral overlap can be quantified from table 2.1 by comparing the column $G_{CO2}(TES)$ with $G_{CO2}(TES, T_{eff})$: The spectral overlap, particularly with water, causes an overestimation of the GHE of CO_2. More specifically, for the US Standard Atmosphere (1976) it increases the observed fraction from 64 % to 78 %. For typical south-polar conditions the increase is between 3 % and 49 %. However, absolute values of the overestimation caused by spectral overlap with water vapour are less than 0.4 W/m^2.

In summary, the values of the greenhouse effect of CO_2 determined from TES measurements shown in section 2.2.3 are reasonable estimates of the total effect CO_2 has on the outgoing long-wave radiative flux. The values shown typically underestimate the effect by some 25 %.

Results

The presented estimates of GHE of CO_2 inferred from TES satellite observations are plausible when comparing with global estimates known from literature: According to Schmidt et al. (2010, table 2) the GHE of CO_2 is expected to range between 22 W/m^2 and 38 W/m^2, depending on the metric used. For all-sky conditions, taking spectral overlap into account and assuming an atmospheric CO_2 concentration of 339 ppm (as in 1980) they estimated a value of 29 W/m^2. Kiehl and Trenberth (1997) used 353 ppm in their calculations, and quantified the CO_2 contribution to the GHE to be 24 W/m^2, also accounting for clouds and spectral overlap. The global average found here is 19 W/m^2, but does not cover the entire 15 µm CO_2 band. If one assumes that on global average 78 % of the spectral band are covered by the TES sensor (see table 2.1), the total GHE of CO_2 is estimated to be 24.3 W/m^2. This compares well with the named references.

The TES observations demonstrate clearly that the phenomenon of negative GHE of CO_2 does occur frequently over the Antarctic continent. From the satellite data, a core region over the Antarctic ice sheet could be identified, where the yearly average is negative. This is a unique feature on the planet. The TES analysis also revealed, that negative GHE is most pronounced in autumn and spring. Moreover, it became clear that there are distinct differences in the GHE of CO_2 between the two hemispheres: G_{CO2} has higher values in the north, and the difference between day and night-time observations is more pronounced. The latter point is most likely due to the greater fraction of land area on the northern hemisphere. The lower and even negative GHE in the south are caused by the extensive and high-elevated continent Antarctica. Strictly speaking, these statements are limited to observations taken in 2006.

The fact that over central Antarctica long-wave emission spectra show a local emission maximum in the 15 µm CO_2-band is opposite to what holds true for the rest of the planet. This observation hints towards an opposite effect of increasing CO_2: An instantaneous increase would increase the energy loss to space, which is a cooling effect on the system. Nevertheless, this would be the instantaneous effect only, not taking any feedback mechanisms into account.

Comparing the TES results to the temperature trend analyses presented in section 1.5, some similarities can be observed: Figure 1.9 shows three analyses of linear temperature change during the last decades. They all show particularly low or even negative trends for central Antarctica. This coincides with the negative yearly average of G_{CO2} found here. Furthermore, comparing the seasonal averages shown in figures 1.12 and 2.7, one can see that the season with the strongest indication of surface cooling, namely autumn (MAM), is also the season with the most negative GHE of CO_2. However, a causal link between the two features has not been shown in the analyses.

2.3 Two layer model considerations

In order to understand the phenomenon of negative greenhouse effect and to qualitatively estimate the instantaneous changes in emitted long-wave flux at TOA with increasing CO_2 concentration, a simple two-layer model is presented in this section. The model consists of a surface and one atmospheric layer (figure 2.9). As the greenhouse effect concerns only the long-wave, the model here is limited to these fluxes. Furthermore, the temperatures of the surface and atmosphere are considered to be local temperatures. They are set by the local energy budget, including horizontal energy transport, and are regarded to be constant in the following. Changes, i.e. the increase of CO_2, are evaluated for their instantaneous impact on the system. Feedback mechanisms on the temperatures are not considered.

The emitted long-wave flux at the top of atmosphere F_{TOA} can be separated into the transmitted surface radiation $(1 - \alpha)\ \sigma\ T_{surf}^4$ and the emission of the atmosphere itself $\alpha\ \sigma\ T_{atm}^4$:

$$F_{TOA} = (1 - \alpha) \cdot \sigma\ T_{surf}^4 + \alpha \cdot \sigma\ T_{atm}^4\ , \tag{2.9}$$

with α being the emission coefficient of the model's atmosphere, σ the Stefan-Boltzmann constant, T_{surf} the surface temperature, and T_{atm} the temperature of the atmosphere. This can be rewritten as:

$$F_{TOA} = \sigma\ T_{surf}^4 + \alpha \cdot \sigma\ (T_{atm}^4 - T_{surf}^4) \tag{2.10}$$

As the surface in most regions on Earth is warmer than the atmosphere, $T_{atm}^4 - T_{surf}^4$ is commonly negative, hence the presence of the atmosphere reduces the TOA emission F_{TOA}. However, in situations as seen over the Antarctic plateau, where the atmosphere, particularly the stratosphere, is often warmer than the surface, the sign of the second term in equation 2.10 is positive. Consequently, the system loses more energy due to the presence of greenhouse gases.

Defining the greenhouse effect G as the difference between the surface emission and F_{TOA} yields:

$$\begin{aligned} G &= \sigma\ T_{surf}^4 - F_{TOA} \\ &= \alpha \cdot \sigma\ (T_{surf}^4 - T_{atm}^4) \end{aligned} \tag{2.11}$$

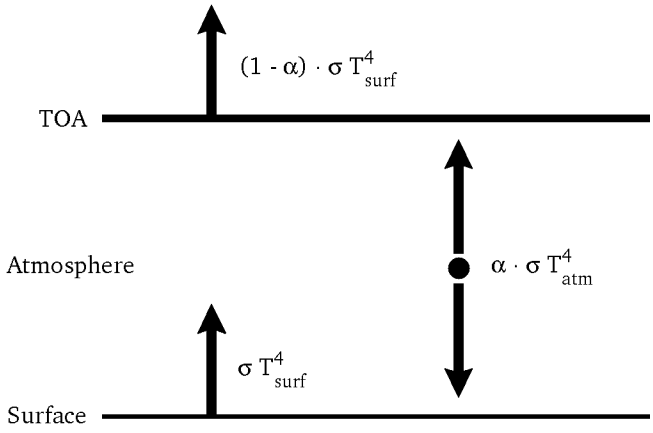

***Figure 2.9**: Two layer model configuration, considering only long-wave fluxes.*

Hence, in regions where the surface is colder than the atmosphere G reaches negative values.

Now, the instantaneous change in long-wave emission caused by a change in α can be formally derived from equation 2.10:

$$\frac{\partial F_{TOA}}{\partial \alpha} = \sigma \, (T_{atm}^4 - T_{surf}^4) \tag{2.12}$$

As stated above, T_{atm}^4 - T_{surf}^4 is typically negative, and therefore F_{TOA} decreases with increasing α. If however, T_{atm}^4 - T_{surf}^4 is positive (as for Antarctica) the energy loss to space F_{TOA} increases with increasing α.

These considerations demonstrate how a surface, which is colder than the atmosphere above it, causes a negative greenhouse effect. Under these conditions, the local instantaneous change in the outgoing long-wave flux after introducing extra greenhouse gases is a cooling effect.

2.4 Radiative transfer calculations for central Antarctic conditions

2.4.1 Radiative transfer model (ALFIP)

Radiative transfer (RT) calculations presented in this study were performed using the line-by-line RT model ALFIP (Automatic Line FInding Program) (Notholt et al. 2006). The program was originally written to identify absorption lines suitable for the retrieval of trace gas concentrations. However, with some modifications implemented by the first author after publication, the code simulates thermal infrared spectra of up- or down-welling radiances for arbitrary clear-sky model atmospheres.

The ALFIP program takes several input files: an overall configuration file, a temperature profile, the concentration profiles of all trace gases to be considered, and a file defining the altitude levels for the model run.

The configuration used in this work was the following:

- Spectral range: 50 cm^{-1} to 2128 cm^{-1} (4.7 µm to 200 µm)
- Spectral resolution: 0.01 cm^{-1} (2.5×10^{-5} µm for 4.7 µm and 0.04 µm for 200 µm)
- Data base of molecular absorption lines: HITRAN 2008 (Rothman et al. 2009)

For the top of atmosphere calculations (section 2.4.5) the altitude levels were chosen such, that two adjacent levels are either 10 hPa or 5 km apart, whatever is closer. For the surface calculations (section 2.4.6) the layer-thickness of the lowermost layer was set to 10 m and gradually increased to 10 hPa at 1500 m above the ground. Above that, the levels are either 10 hPa or 5 km apart, whatever is closer. The determination of TOA in section 2.2.1 was performed using 10 hPa or 1 km thick layers.

The rest of the relevant model input is described in the following three sections. All input data to ALFIP were calculated from in-situ measurements as far as possible. The model atmospheres were constructed as monthly means over the years 1994 - 2012. The South Pole was chosen for being representative for the conditions on the East Antarctic plateau.

Calculations of greenhouse effect of CO_2 G_{CO2} for a specific CO_2 concentration c were done in analogy to equation 2.1; with the limits of integration set to the spectral range of the modelled spectra. Essentially, the GHE is taken as the difference in TOA emission between a model run with and without CO_2:

$$G_{CO_2} = \int_{4.7\ \mu m}^{200\ \mu m} \left[F_{\lambda,TOA}(c=0) - F_{\lambda,TOA}(c)\right]\, d\lambda \tag{2.13}$$

Calculations of long-wave down-welling radiative flux at the surface LWD were done similarly:

$$LWD = \int_{4.7\ \mu m}^{200\ \mu m} F_{\lambda,surf}(c)\, d\lambda\,, \tag{2.14}$$

with $F_{\lambda,surf}$ being the spectral radiance emitted by the atmosphere towards the surface.

2.4.2 Estimation of surface emission from BSRN measurements

The surface skin temperature T_{surf} is crucial for the modelling of top of atmosphere long-wave fluxes and therefore crucial for the quantification of the greenhouse effect. For this reason, the surface skin temperature was determined from in-situ broadband upwelling long-wave (LWU) flux measurements, taken at the South Pole.

The record was taken from the Baseline Surface Radiation Network (BSRN), which aims to provide the best quality possible for this kind of observations (König-Langlo et al. 2013). To determine monthly means of the surface skin temperature at the South Pole, all BSRN data sets entitled *Basic and other measurements* from this station for the period 1994-01-01 until 2012-12-31 (Dutton and Michalsky 2014) were used. From these, monthly averages of LWU were calculated and converted into temperature, assuming black body emission, which is a fair approximation for snow surfaces. More details of the data processing are mentioned in the following section on page 54. The resulting values are shown by the black line in figure 2.10.

This study also utilises reanalyses from the European Centre for Medium-Range Weather Forecasts (ECMWF), namely the ERA-Interim data set (see section 2.4.3). The data set also provides the surface skin temperature, which could readily be used here. However, the skin temperature of the reanalysis data is typically too warm, in comparison with the BSRN LWU record. Figure 2.10 also shows the ECMWF data for the period 1994 till 2012 for comparison with the BSRN values: The skin temperature of the reanalysis is on average 3°C warmer than the BSRN LWU estimate, even though the surface elevation in the ECMWF data is correct (2827 mASL). Comparing the 2 m air temperatures of the two sources yields differences on the order of 5°C.

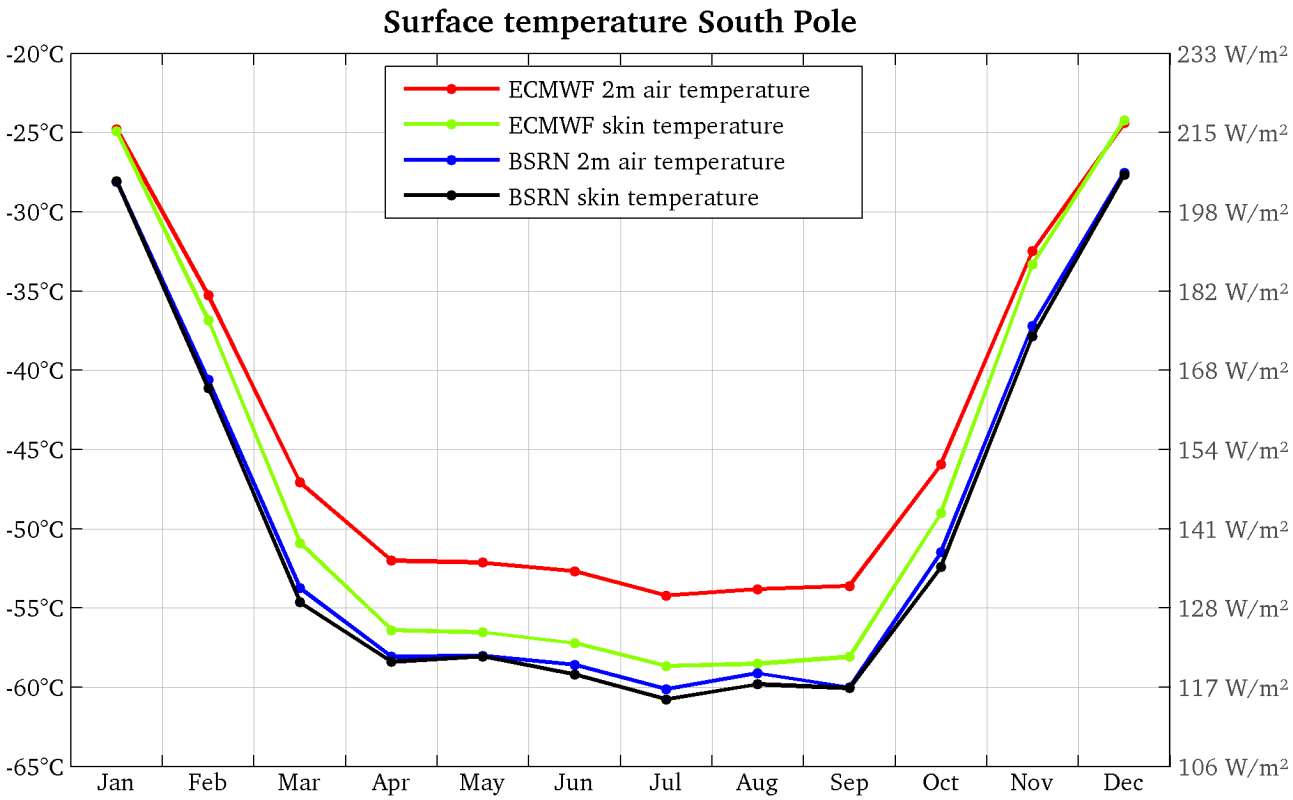

***Figure 2.10**: Monthly means of surface temperature at the South Pole for the years 1994 - 2012. The curves entitled **ECMWF** are from ERA-Interim reanalysis data. The **BSRN skin temperature** was derived from long-wave upwelling radiative flux measurements, assuming black body emission from the surface. For comparison, the scale on the right gives the radiative flux according to the Stefan-Boltzmann law.*

In the ALFIP configuration file one specifies a *source temperature,* which sets the background radiation to the black body spectral radiance of this temperature. For the calculations of the TOA emission performed for this study, the *source temperature* is set to the surface skin temperature T_{surf} determined from the BSRN LWU measurements. This was calculated assuming black body emission from the surface. Now, even if the assumption of black body emission for snow is not fully correct, this inaccuracy is mostly compensated here: The radiative flux LWU was converted into T_{surf}, and is now converted back into spectral radiances using the same assumption. Only effects from possibly non-grey emissivity of snow is not accounted for, which can safely be neglected. For the calculations of downwelling fluxes at the surface as presented in section 2.4.6 the *source temperature* was set to 0 K.

2.4.3 Construction of temperature profiles

The temperature profile is the most essential input for radiative transfer analysis. For this reason, extensive care was taken to create representative temperature profiles for central Antarctica. Even though reanalysis data sets provide perfect temporal and spatial coverage, the most reliable source of data are considered to be in-situ measurements, i.e. radiosonde data and surface observations. As radiosondes typically do not reach higher than 40 km altitude, the in-situ data used here are complemented with reanalyses from the ECMWF, which typically reach up to 60 km altitude. As mentioned in section 2.2.1 (see figure 2.3), the atmosphere above that still has some small effect on TOA outgoing long-wave radiation. Therefore, the temperature profile of the US Standard Atmosphere 1976 is used for completion up to 120 km altitude.

As shown in section 2.2.3 (particularly figure 2.8), the phenomenon of negative GHE varies considerably throughout the year. In view of the course of the temperature of the south-polar atmosphere over the year (figure 2.11), it seems suitable to consider monthly averaged temperature profiles. Seasonal averages, or even a yearly averaged temperature profile, will not represent the essential features of the Antarctic atmosphere. To illustrate the suitability of monthly averaged profiles, figure 2.11 shows two Hovmöller-diagrams: Panel 2.11a was constructed from all radiosondes, interpolated onto a day-of-the-year vs. altitude grid for each year, which were then averaged resulting in the field shown. In contrast to that, panel 2.11b was constructed from the 12 monthly averaged temperature profiles used in this study. Obviously, the monthly profiles are well representative for the south-polar atmosphere.

Data availability and data sources

On the Antarctic plateau, there are three stations that perform or have performed radiosoundings operationally all year-round: Amundsen-Scott (South Pole), Concordia (Dome C) and Vostok. Amundsen-Scott has the longest and most complete record: It dates back to 1961 and is continued until today. Typically, the record contains at least one ascent per day, during summer-time even two launches. Daily radiosoundings at Concordia Station were started in 2005 and are also continued until today; whereas the Vostok record was started in 1958, but discontinued in 1992. Due to the data availability, and as for Amundsen-Scott Station co-located surface measurements of long-wave upwelling radiative flux are available (BSRN station), this site was chosen for the construction of atmospheric temperature profiles.

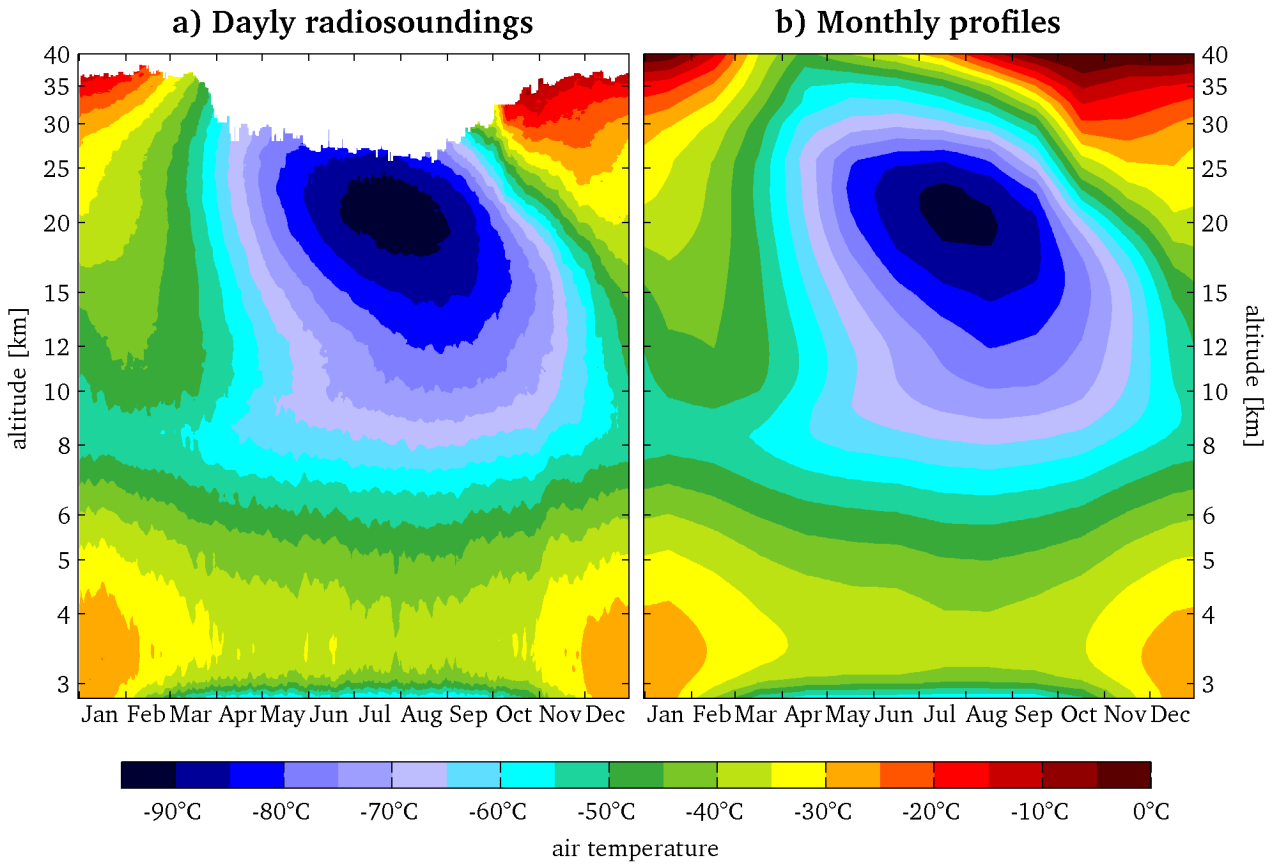

Figure 2.11: *Hovmöller-diagrams showing the typical course of the temperature at the South Pole.* ***a)*** *This data set was constructed from all available radiosoundings from the South Pole between 1994-01-01 and 2012-12-31. All soundings of one year were interpolated onto a day-of-the-year vs. altitude grid. These 19 fields were then averaged grid-point by grid-point, resulting in the field shown.* ***b)*** *This data set shows the 12 monthly averaged temperature profiles used in this study.*

South Pole radiosonde data from soundings since 1994-01-01 are readily available from the data portal at http://www.esrl.noaa.gov/raobs/, which is provided by the Earth System Research Laboratory of the National Oceanic and Atmospheric Administration (Govett 2014). The portal serves data for the so-called *mandatory* pressure levels (i.e. surface, 500 hPa, 400 hPa, 300 hPa, 200 hPa, 150 hPa, 100 hPa, 70 hPa, 50 hPa, 30 hPa, 20 hPa, 10 hPa, 7 hPa and 5 hPa) and those for the *significant* temperature and wind levels. For this study, all soundings between 1994-01-01 and 2012-12-31 were used, which amounts to 9698 ascends for this period of 19 years.

The lowermost data point of the temperature profiles were set to the surface skin temperature determined from the BSRN LWU data from the South Pole, see above section 2.4.2 for details.

Above the radiosonde level, ECMWF ERA-Interim reanalysis data (Berrisford et al. 2011; Dee et al. 2011) were incorporated into the monthly averaged profiles. Specifically, the *Monthly Means of Daily Means, Full Resolution* for the period mentioned above were used.

Beyond the top of model of the ECMWF ERA-Interim data, the US Standard Atmosphere (1976) complements the temperature profiles up to 120 km altitude.

Processing

The BSRN surface data were first checked and cleaned with the *BSRN Toolbox,* applying the *Physical possible limits* and the *Comparison* quality checks (Schmithüsen et al. 2012). For each month, i.e. January till December, all available measurements of LWU acquired during the 19 year period were then averaged into one single value, which was converted into the surface skin temperature using the Stefan-Boltzmann law (see also figure 2.10, curve *BSRN skin temperature*).

The radiosonde profiles were checked and cleaned manually for obviously erroneous measurements. All soundings of a specific month were then interpolated linearly with respect to altitude between the available levels. For altitudes with a minimum of 40 soundings, an average temperature was calculated. The resulting profile was then linearly interpolated onto the altitude levels used by ALFIP.

The ECMWF ERA-Interim monthly mean temperature profiles were interpolated linearly with respect to altitude between the model levels. Then, for each altitude the average over the 19 values was calculated. Finally, the resulting profile was linearly interpolated onto the altitude levels used by ALFIP.

From the uppermost level of the ECMWF data up until the thermal mesopause of the US Standard Atmosphere, the temperature profile was fitted gradually to prevent a spike in the profile. From the mesopause upwards, temperatures of all monthly profiles are identical to those of the US Standard Atmosphere.

Figure 2.12 illustrates an example of such a fitted temperature profile, shown by the black line. At the surface, it starts with the BSRN LWU data (blue marker), which is typically colder than the ECMWF data. Above that, the radiosondes are used until data becomes to sparse, here at about 25 km altitude. From there on, the ECMWF data is used up to the top of the model, which is approximately 55 km here. After that, it approaches the US Standard Atmosphere.

Figure 2.13 visualises the final monthly averaged profiles for the South Pole, which are used for RT modelling with ALFIP.

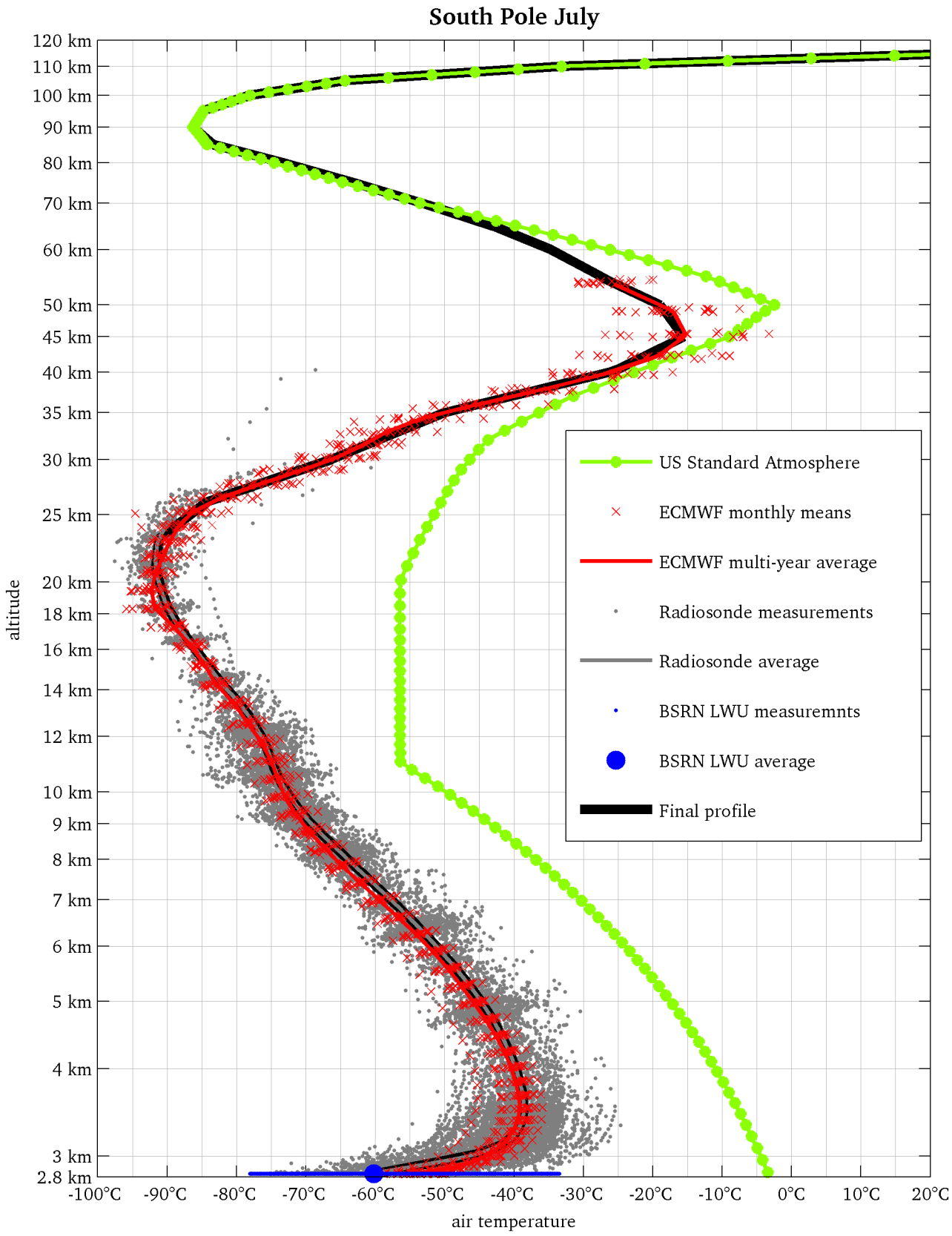

***Figure 2.12**: Example of data used for the construction of temperature profiles, here that of South Pole, July. The actual profile used for the modelling is shown by the black line. It is a compilation of BSRN surface measurements (blue), radiosonde profiles (grey), ECMWF ERA-Interim reanalysis data (red) and the US Standard Atmosphere (1976) (green).*

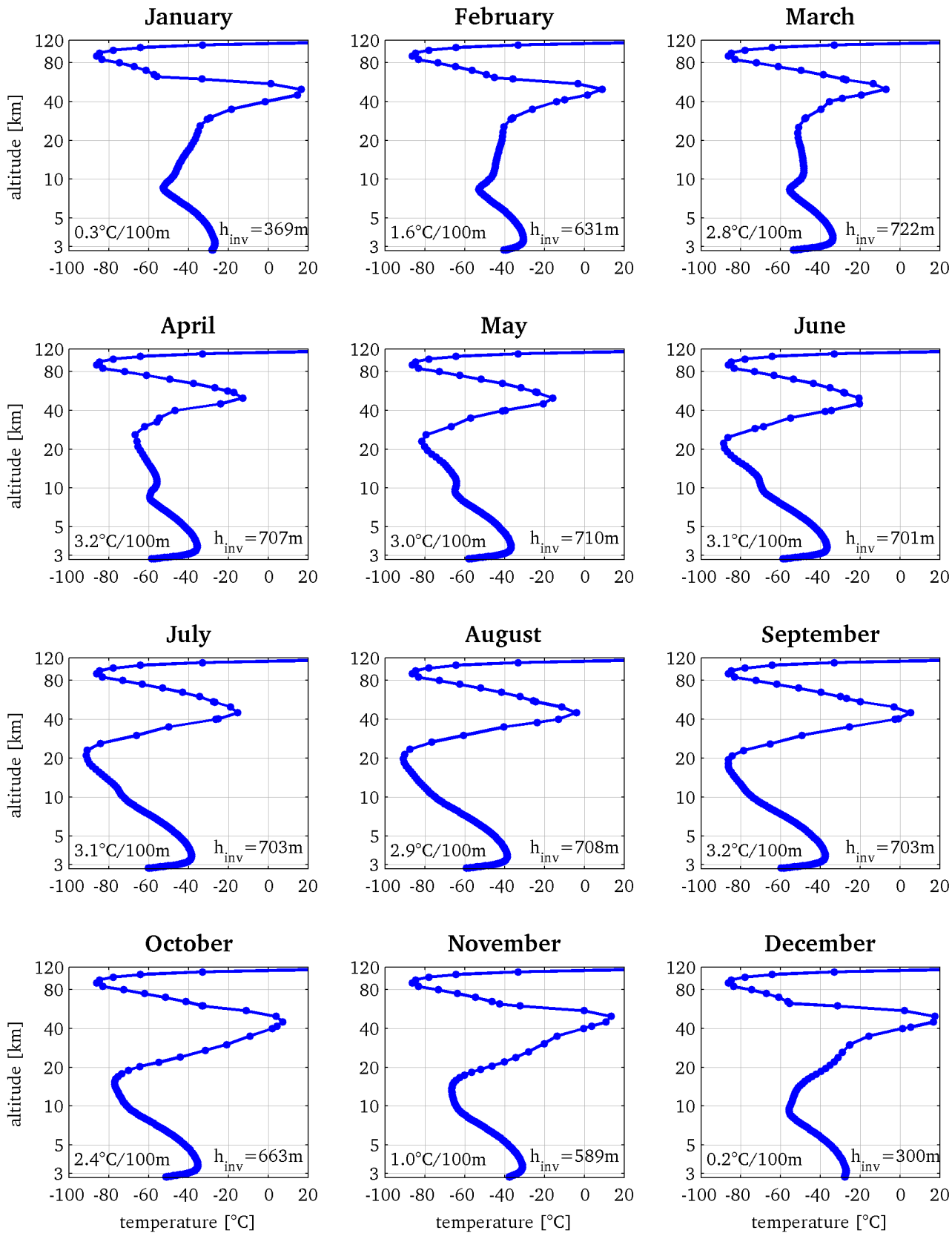

***Figure 2.13**: South-polar monthly averaged temperature profiles used for radiative transfer modelling. The profiles were constructed from BSRN surface data, radiosonde measurements, ECMWF ERA-Interim reanalysis data and complemented with the US Standard Atmosphere. The profiles are mean profiles for the period 1994 till 2012. The height and strength of the inversion layer at the surface are given in the lower right and left corners respectively.*

2.4.4 Construction of trace gas profiles

For the RT simulations presented here, the five most important greenhouse gases were included: H_2O, CO_2, O_3, CH_4, N_2O. This study focuses mainly on CO_2, and more specifically on the 15 µm absorption band of this gas. Out of the other four gases, H_2O has by far the greatest spectral overlap with this CO_2-band. For this reason, great care has also been taken to construct realistic estimates of the H_2O profiles on the Antarctic plateau.

CO_2 is considered to be a well-mixed greenhouse gas. Therefore, the CO_2 concentration was set constant for all levels in the modelling.

Figure 2.14 shows the profiles of the trace gases methane, ozone and nitrous oxide that were used for the line-by-line RT modelling. The concentrations were taken from the *Arctic* profiles suggested and provided by Notholt et al. (2006, http://www.iup.physik.uni-bremen.de/ftir/alfip), originating from soundings reported by Peterson and Margitan (1995). Even though the Arctic is quite different to the Antarctic, this study focuses on CO_2: As the spectral overlap with O_3, CH_4 and N_2O is small, the results should not be influenced greatly by the chosen profiles for these species.

The water profiles were compiled in analogy to the temperature profiles, using the BSRN 2 m relative humidity, radiosonde humidity profiles, ECMWF ERA-Interim reanalyses data, and the *Arctic* profile mentioned above to complement atop the ECMWF data. Essentially, the latter (*Arctic* profile) contributes humidity values only in the meso- and thermosphere, where the abundance of water is virtually zero anyway. Again, measurements and reanalyses from the South Pole for the period 1994 until 2012 were combined into monthly averaged profiles. Figure 2.15 gives an example: It shows all data that were used for the compilation of the South Pole October H_2O-profile.

Radiosonde humidity measurements in the stratosphere are often unrealistically high (figure 2.15). This is caused by the measurement technique: Radiosondes commonly use thin-film capacitors, which measure the relative humidity at a typical numerical resolution of 1 %. In the stratosphere the readings eventually reach 1 %, but usually do not drop to 0 %. The remaining constant 1 % relative humidity causes the water vapour partial pressure to increase monotonically with altitude, due to increasing temperature in the stratospheric inversion layer. The volume mixing ratio, which is shown in figure 2.15, is the quotient of partial pressure over total air pressure; with the latter decreasing exponentially with increasing altitude. Hence, the quotient approaches infinity for small but constant relative humidity readings.

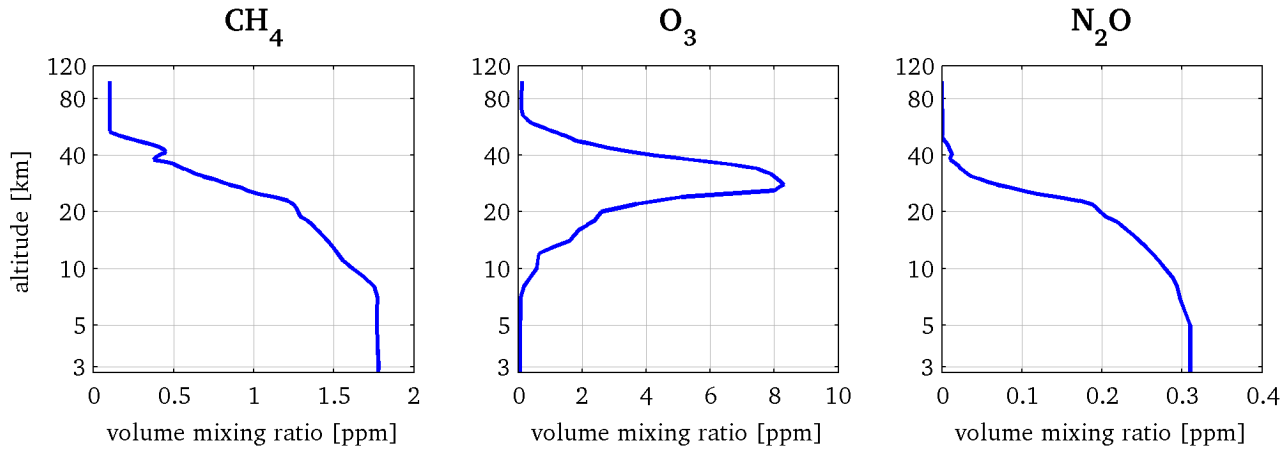

***Figure 2.14**: Profiles of trace gas concentration for methane (CH_4), ozone (O_3) and nitrous oxide (N_2O) used for radiative transfer modelling with ALFIP. The profiles were taken from Notholt et al. (2006, http://www.iup.physik.uni-bremen.de/ftir/alfip).*

For the above reason, the radiosonde profiles were only used from the surface up until the minimum in the volume mixing ratio is reached (tropopause). From there on, the ECMWF data were taken to be the best estimate. In the mesosphere and above, the profile was complemented with the *Arctic* H_2O profile, giving values close to zero anyway. Figure 2.16 shows all H_2O-profiles from the South Pole that were used for RT calculations.

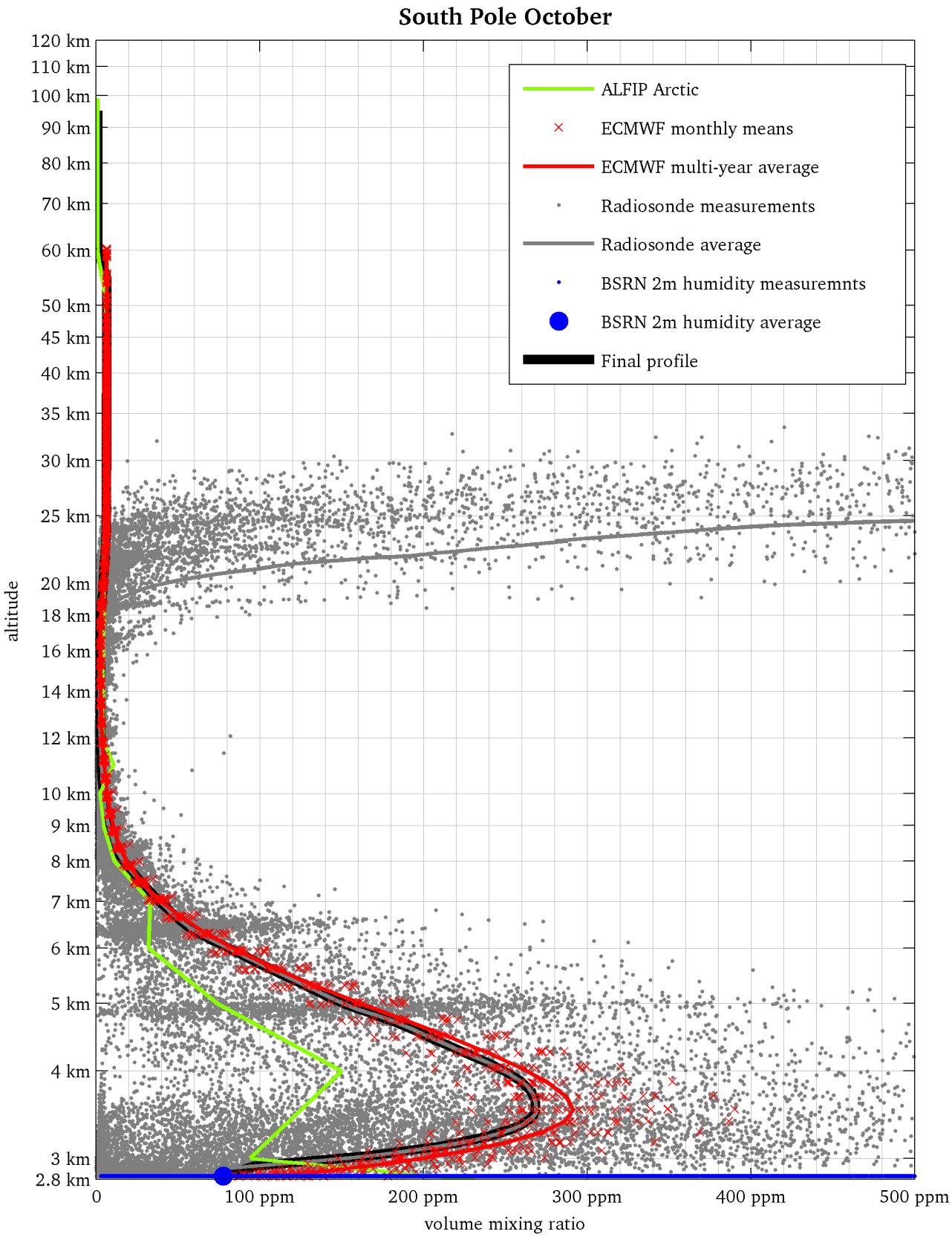

***Figure 2.15**: Example of data used for the construction of humidity profiles, here that of South Pole, October. The actual profile used for the modelling is shown by the black line. It is a compilation of BSRN surface measurements (blue), radiosonde profiles (grey), ECMWF ERA-Interim reanalysis data (red) and the* `Arctic` *template from Notholt et al. (2006, http://www.iup.physik.uni-bremen.de/ftir/alfip) (green).*

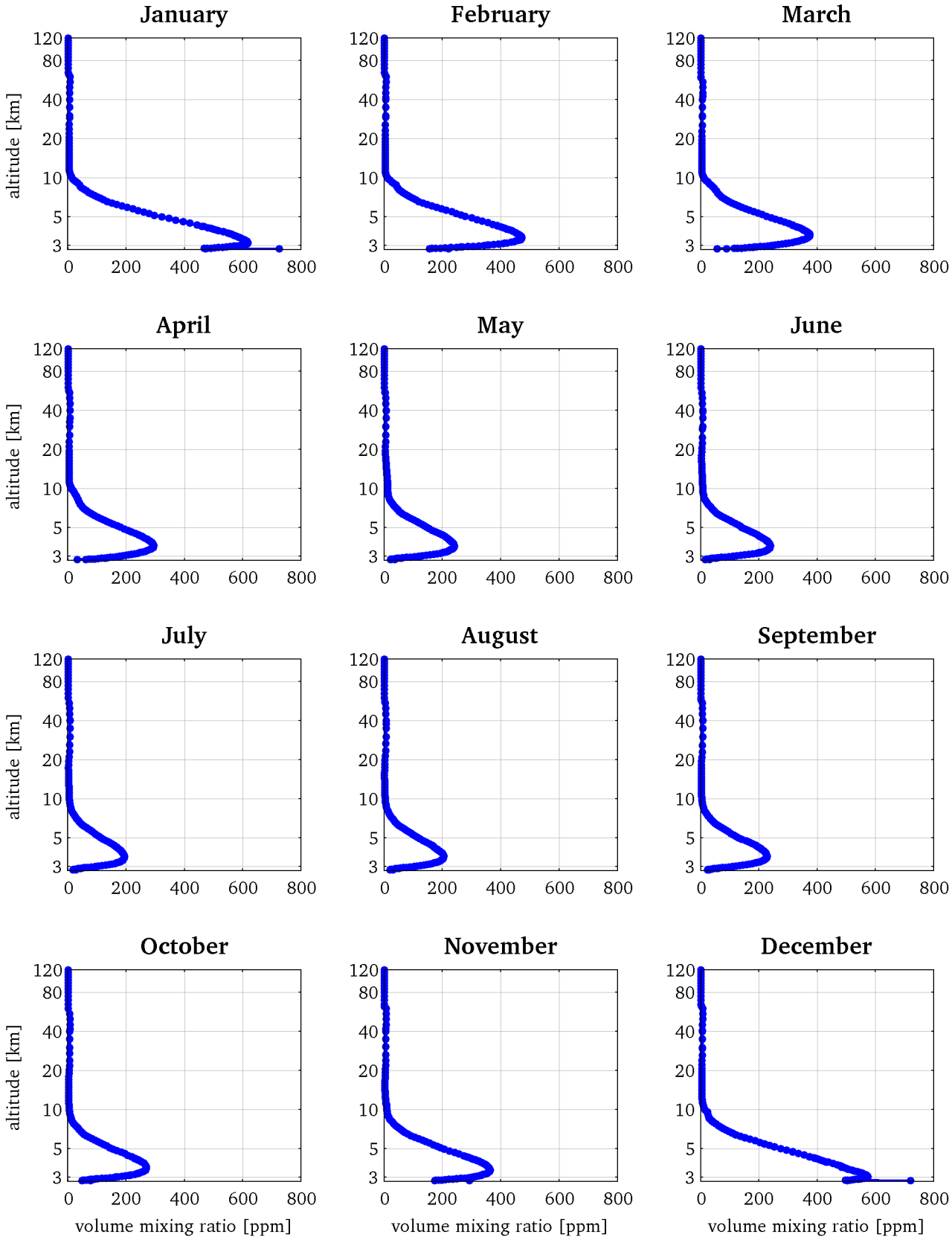

***Figure 2.16**: South-polar monthly averaged humidity profiles used for radiative transfer modelling. The profiles were constructed from BSRN surface data, radiosonde measurements, ECMWF ERA-Interim reanalysis data and complemented with the Arctic profile from Notholt et al. (2006, http://www.iup.physik.uni-bremen.de/ftir/alfip). The profiles are mean profiles for the period 1994 till 2012.*

2.4.5 Results: Top of atmosphere calculations

Figure 2.17 shows five TOA emission spectra that were calculated with ALFIP with a CO_2 concentration of c = 380 ppm. The spectrum of the US Standard Atmosphere (1976) illustrates the characteristic local minimum in the spectral radiance in the CO_2-band around 15 µm. Out of the four examples shown for South Pole, only July exhibits this pronounced local minimum for the modelled clear-sky conditions. During the other months shown here, the emission in the center of the absorption band exceeds the surface emission.

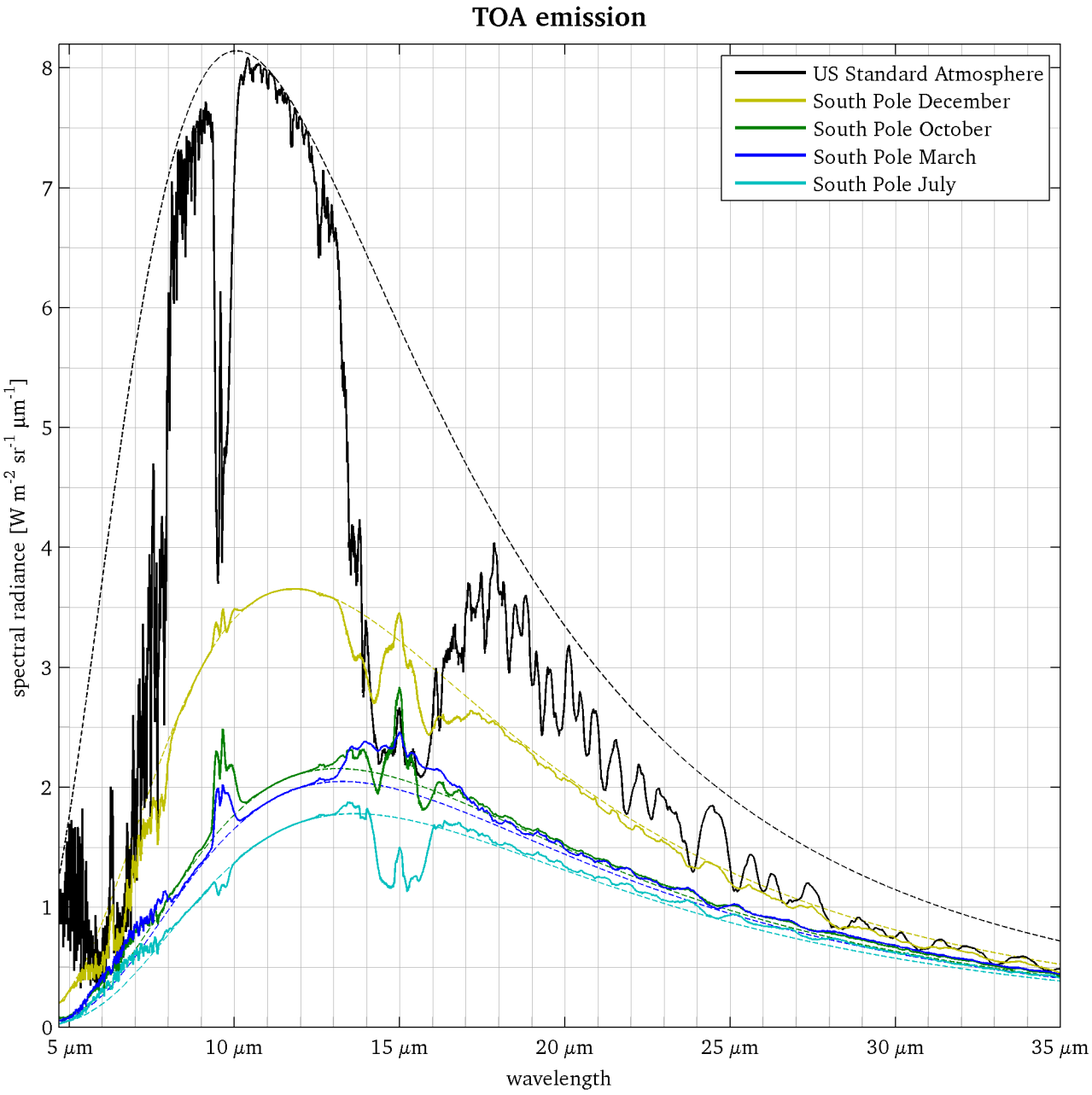

***Figure 2.17**: Top of atmosphere long-wave emission spectra calculated with ALFIP for clear-sky conditions with a CO_2 concentration of 380 ppm (solid lines). The spectra are low-pass filtered for clarity. Dashed lines indicate the surface emission (Planck curves of surface skin temperature).*

Results for all modelled monthly averaged south-polar atmospheric conditions are shown in figure 2.18. The display is limited to the CO_2-band, showing spectra for c = 0 ppm, 100 ppm, 380 ppm and 1000 ppm. In February, March and April the TOA emission calculated for a somewhat realistic CO_2 concentration (black lines) is more than the surface emission (grey lines) and that of a CO_2-free atmosphere (green lines). This applies to almost the entire CO_2-band. Hence, from February till April the GHE of CO_2 is negative. Table 2.2 gives the numeric values: -1.0 W/m^2, -2.9 W/m^2 and -1.0 W/m^2 respectively. From May till August, the spectra show a local minimum in the CO_2-band, illustrating positive GHE between 1.3 W/m^2 and 2.1 W/m^2. Between September and November the spectra for 380 ppm feature substantial parts of both, positive and negative GHE. Out of these three months, only October shows an overall negative value (-0.8 W/m^2) whereas September and November figures are positive (0.6 W/m^2 and 1.8 W/m^2 respectively). Results for December and January demonstrate the strongest GHE of CO_2 occurring over the Antarctic plateau with values of 3.4 W/m^2 and 2.9 W/m^2, respectively; while cogeneric calculations for the US Standard Atmosphere yield 28.1 W/m^2. Note, even during these summer months south-polar TOA emission in the very center of the band exceeds the surface emission.

In figure 2.18 the spectra for 100 ppm (blue) and 1000 ppm (red) are given to illustrate the changes occurring when altering the CO_2 concentration. For increasing CO_2 the TOA emission in the center of the band increases for all months. This is also true for the US Standard Atmosphere, as the atmosphere is opaque at 15 µm and TOA emission at this wavelength originates mostly from the lower stratosphere, where the temperature profile shows an inversion. The typical decrease in TOA emission (which corresponds to an increase in GHE) for increasing CO_2 is attributed to the reduction of spectral radiance on the flanks of the band. For most of the south-polar conditions

***Table 2.2**: Greenhouse effect of CO_2 and derivative thereof (instantaneous radiative forcing) for CO_2 concentration of c = 380 ppm. Results are shown for all atmospheric conditions used for ALFIP modelling.*

	G_{CO_2} $[Wm^{-2}]$	$\frac{d}{dc}G_{CO_2}$ $[\frac{Wm^{-2}}{100ppmv}]$
US Standard Atmosphere	28.07	1.15
South Pole January	2.95	-0.07
South Pole February	-0.99	-0.16
South Pole March	-2.94	-0.15
South Pole April	-1.03	-0.02
South Pole May	1.34	0.08
South Pole June	2.05	0.10
South Pole July	2.12	0.08
South Pole August	1.95	0.02
South Pole September	0.57	-0.11
South Pole October	-0.83	-0.34
South Pole November	1.74	-0.25
South Pole December	3.39	-0.13
South Pole DJF	1.87	-0.12
South Pole MAM	-0.87	-0.03
South Pole JJA	2.04	0.07
South Pole SON	0.48	-0.24
South Pole yearly mean	0.88	-0.08

simulated here, this reduction of spectral radiance on the flanks is overcompensated by the gain in the center of the CO_2-band. Specifically, for all months except May till August the GHE of CO_2 decreases with increasing CO_2 (table 2.2). Figure 2.19 also illustrates this: The figure shows the GHE for different CO_2 concentrations for all atmospheric conditions simulated in this work. For the US Standard Atmosphere (1976) G_{CO2} increases monotonically, while South Pole results are contrary to that: February, March and April show decreasing negative GHE for all CO_2 concentrations. Curves for May until August are qualitatively comparable to the US Standard Atmosphere (1976): positive and monotonically increasing. From September until January, again, the results indicate a decrease in GHE with increasing CO_2, with only October being negative at current day's CO_2 concentration.

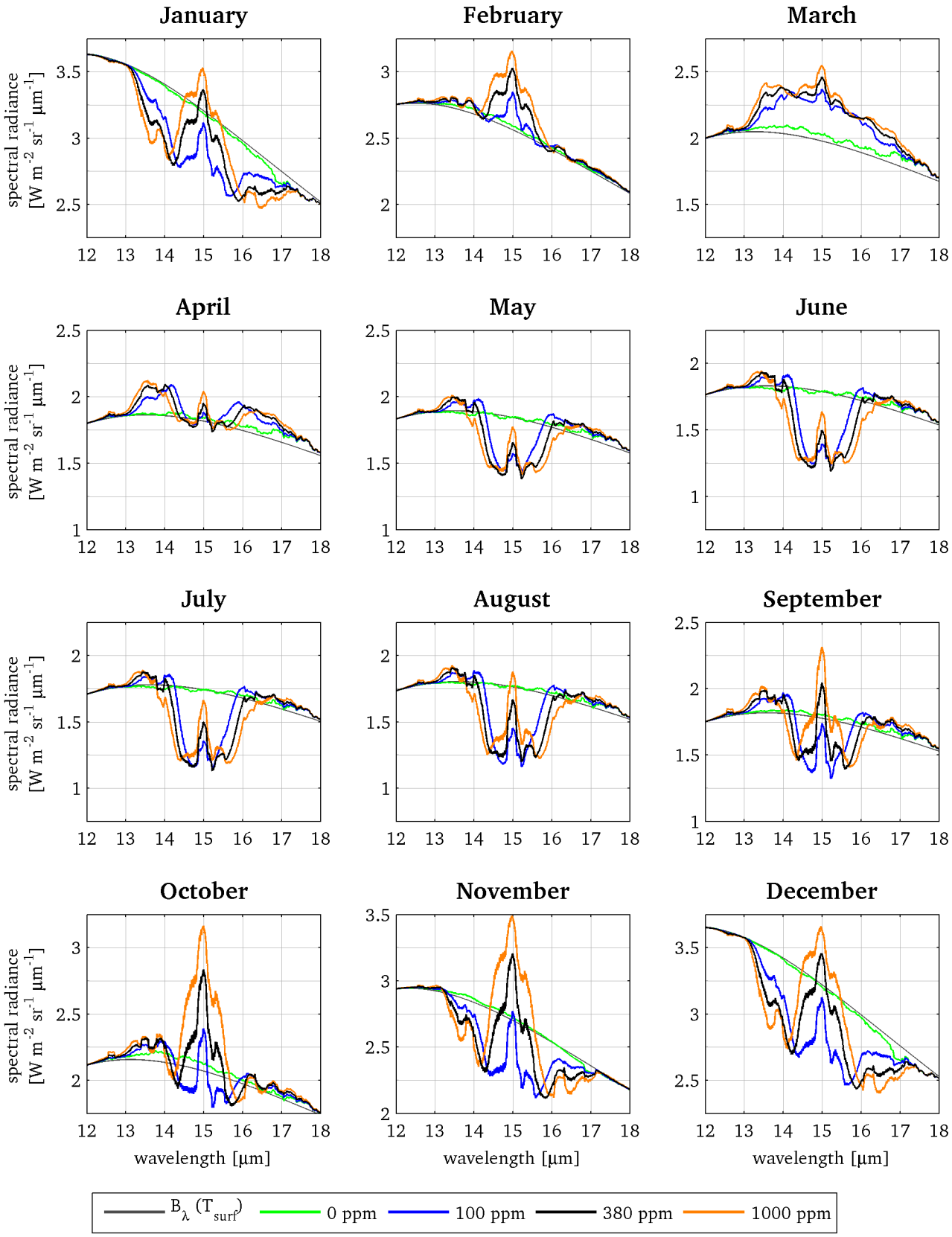

***Figure 2.18**: CO_2-band of top of atmosphere long-wave emission modelled with ALFIP. The spectra were calculated for south-polar clear-sky atmospheric conditions and various CO_2 concentrations. The spectra are low-pass filtered for clarity. The grey lines indicate the surface emission (Planck curves of surface skin temperature).*

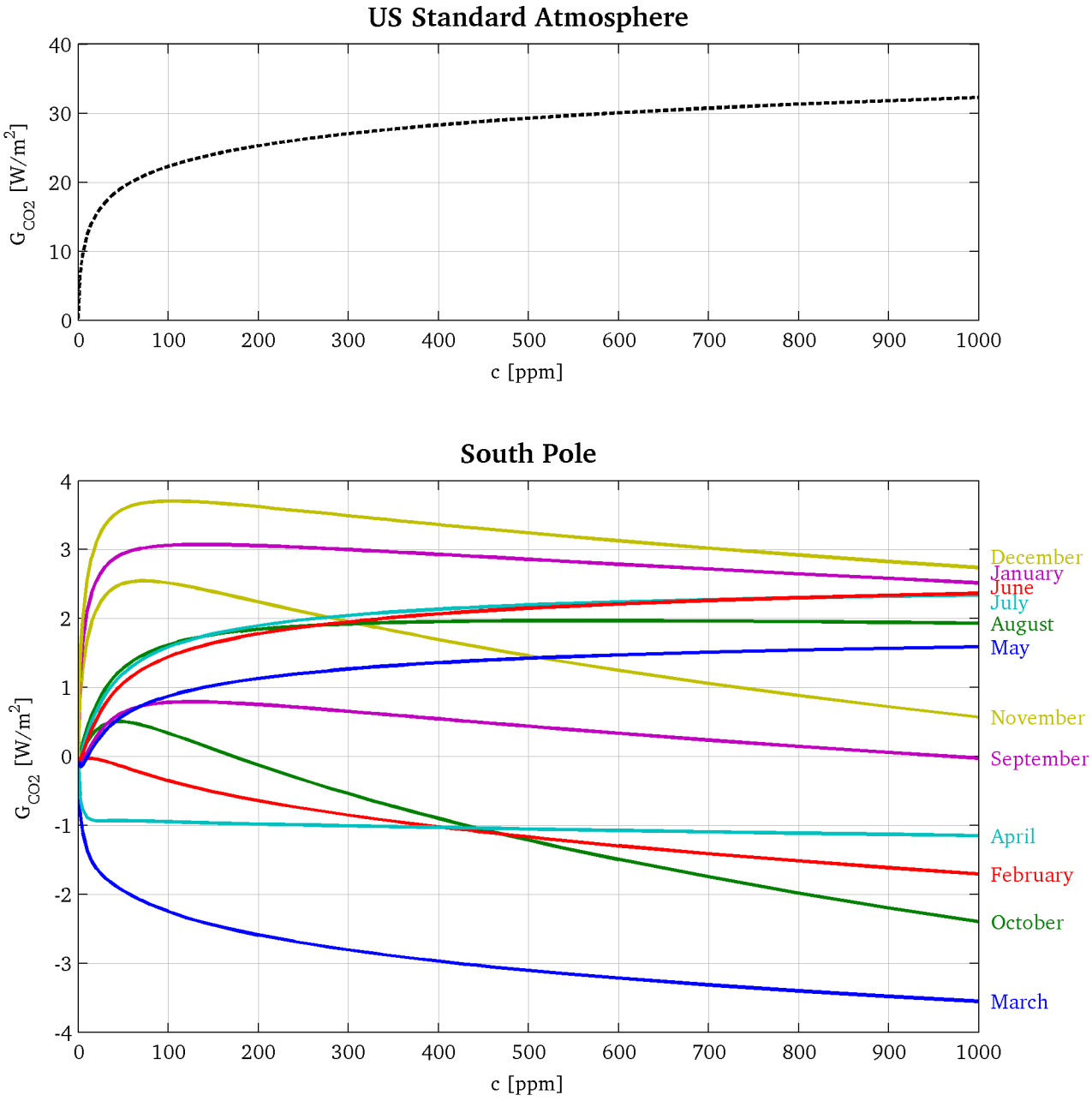

***Figure 2.19**: Greenhouse effect of CO_2 as a function of CO_2 concentration c. The curves were constructed from spectra calculated with ALFIP, assuming clear sky. The slope of the curves can be interpreted as instantaneous radiative forcing of CO_2. Numeric values and the derivative of the curves at c = 380 ppm are given in table 2.2.*

2.4.6 Results: Surface calculations

Figure 2.20 shows examples of modelled spectra of long-wave downwelling radiation at the surface (LWD) for clear-sky conditions. Common atmospheric conditions (US Standard Atmosphere, 1976) feature contributions from virtually all wavelengths with the exception of the window between 8 µm and 13 µm. A substantial difference to that is the dry south-polar atmosphere: Even though the LWD-spectra are qualitatively comparable to the US Standard Atmosphere (1976) for wavelengths up to 14 µm, they differ in and beyond the CO_2-band.

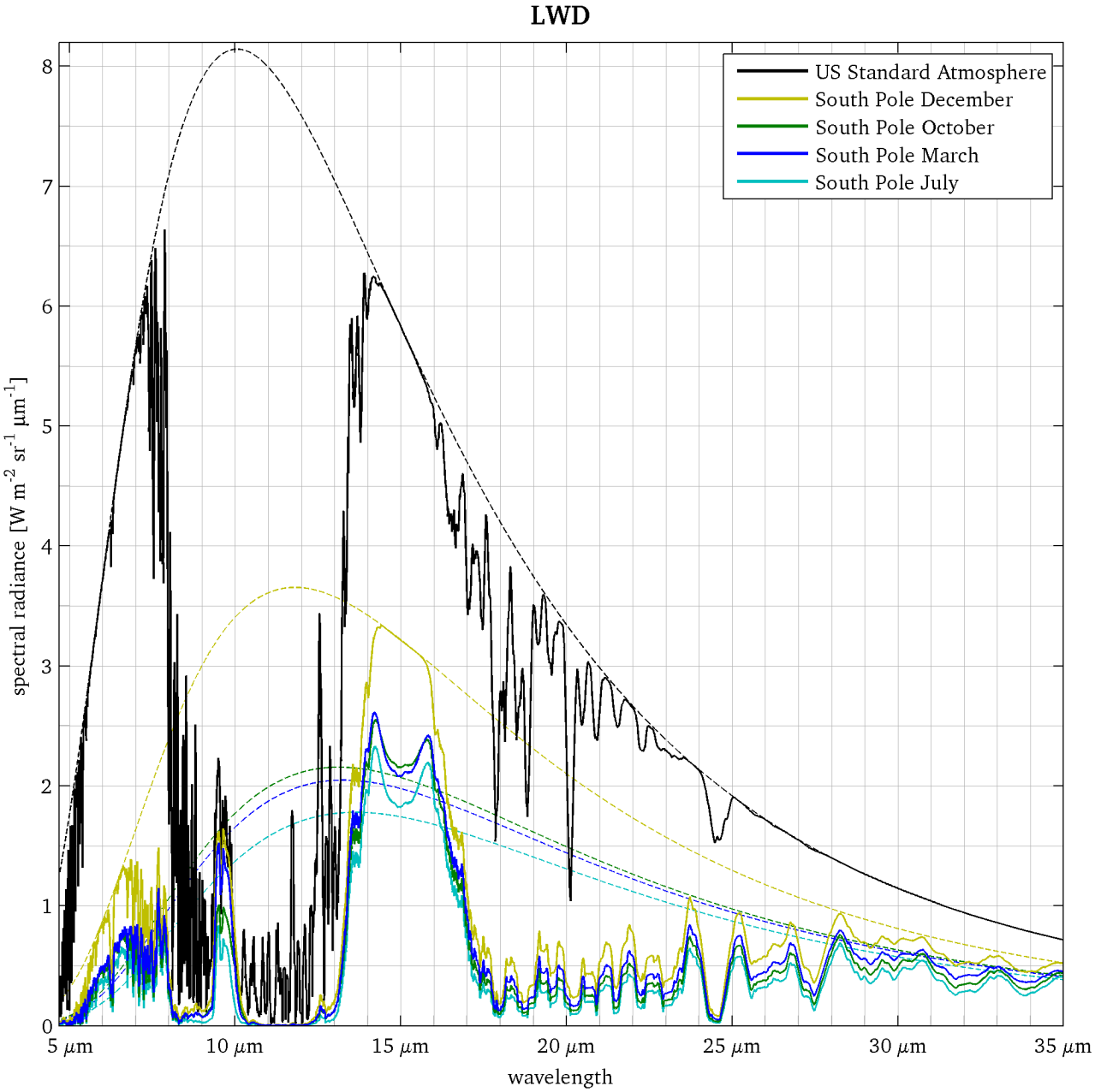

***Figure 2.20**: Surface long-wave downwelling spectral radiance calculated with ALFIP for clear-sky conditions with a CO_2 concentration of 380 ppm (solid lines). The spectra are low-pass filtered for clarity. Dashed lines indicate the upward flux (Planck curves of surface skin temperature).*

In the center of the CO_2-band (between 14.2 µm and 15.8 µm) the curves of March, July and October show a local minimum. This is caused by the strong temperature inversion at the surface: The more opaque the atmosphere is at a certain wavelength, the lower is the effective emission height of the radiance seen at the surface. For inverted temperature profiles, this means lower spectral radiance for wavelengths of strong atmospheric absorption/ emission. Furthermore, the inversion causes the spectral radiance in this wavelength range to be higher than the surface emission (dashed lines). This is in contrast to US Standard Atmosphere and south-polar summer conditions, where the spectral radiance in the center of the CO_2-band is nearly equal to the surface emission.

The other difference, beyond the CO_2-band, is the lack of the contribution from water vapour to LWD. As the atmosphere at the South Pole is extremely dry, it is far from being opaque for wavelengths between 17 µm and 28 µm (see also figure 2.1c).

Figure 2.21 gives modelled LWD-spectra for all south-polar atmospheric conditions considered here. For realistic CO_2 concentrations, all months but January and December feature the local minimum in the very center of the CO_2 band, which is characteristic for strong temperature inversions at the surface. Additionally, the LWD spectral radiance exceeds the surface emission due to that. Furthermore, common to all 12 conditions is the well pronounced flank of the CO_2-band between 16 µm and 18 µm. This shows that even in the warmest months, water vapour is not abundant enough to fill the spectrum for wavelengths greater than the CO_2-band. Consequently, this means that the typical LWD-flux on the Antarctic ice sheet is dominated by the contribution of CO_2.

Integrated spectra of the ALFIP simulations for a CO_2 concentration of 380 ppm are also included in section 2.5.2, figure 2.26 (panel *LWD*). Since no clouds were considered in the ALFIP calculations, the values for LWD are lower than in reality.

In analogy to the TOA emission spectra, figure 2.21 gives LWD-spectra for greatly reduced (100 ppm, shown in green) and increased (1000 ppm, shown in orange) CO_2 concentration. For all months from February till November increasing CO_2 causes a slight decrease of LWD in the center of the CO_2-band. This is the part of the spectrum, where radiation originates mostly from within the inversion. On the flanks, where the emission received at the surface comes predominantly from higher layers of the atmosphere, increasing CO_2 causes the well known increase in LWD. The overall effect can be seen from figure 2.22. For all modelled south-polar conditions LWD instantaneously increases with increasing CO_2. The slopes of the curves at c = 380 ppm range between 0.7 W/(m^2 100 ppm) during April until September and almost 1.2 W/(m^2 100 ppm) for December and January. The yearly average is 0.82 W/(m^2 100 ppm). For comparison, the curve of the US Standard Atmosphere (1976) slopes at 1.6 W/(m^2 100 ppm) at c = 380 ppm.

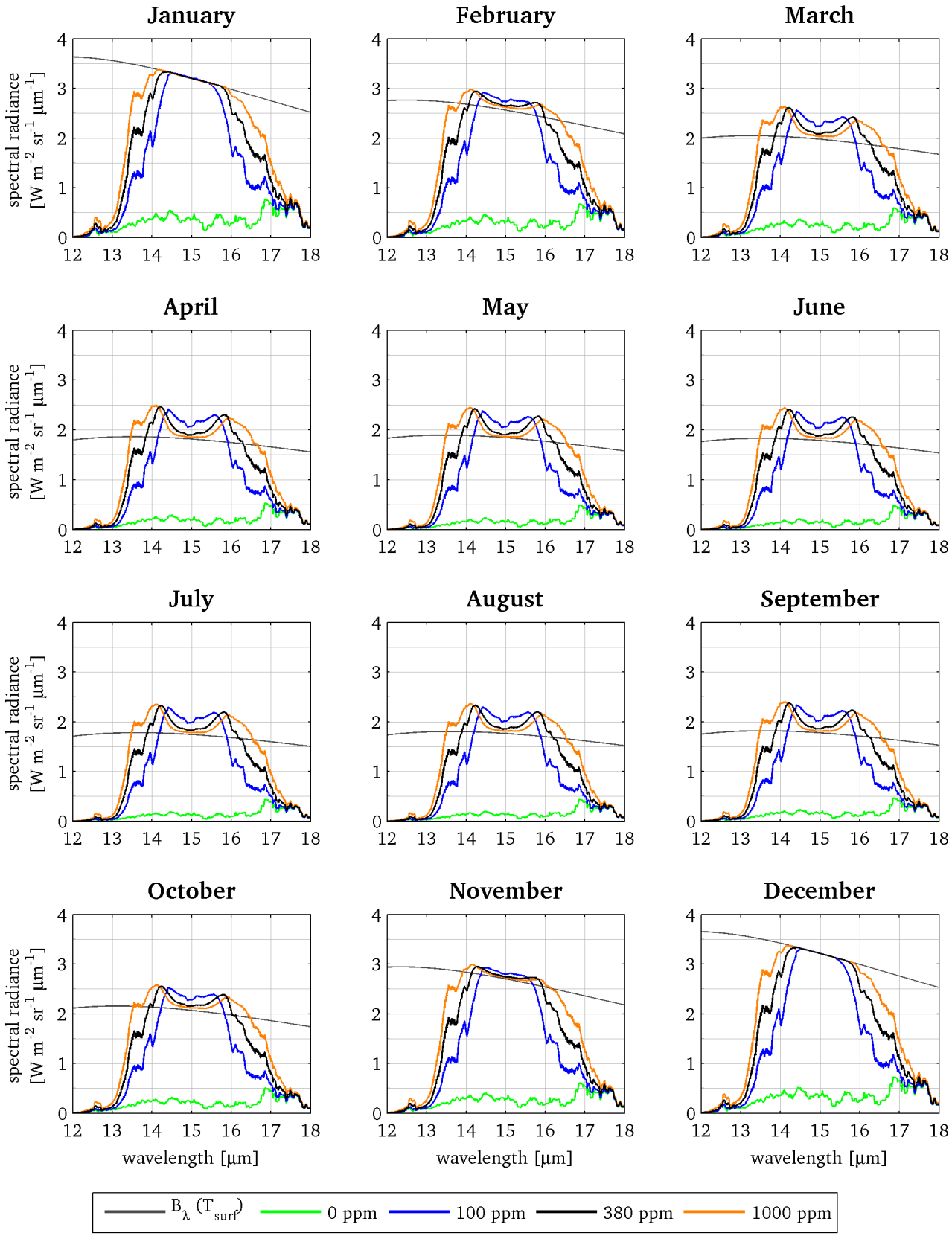

***Figure 2.21**: CO_2-band of surface long-wave downwelling spectral radiance modelled with ALFIP. The spectra were calculated for south-polar clear-sky atmospheric conditions and various CO_2 concentrations. The spectra are low-pass filtered for clarity. The grey lines indicate the upward flux (Planck curves of surface skin temperature).*

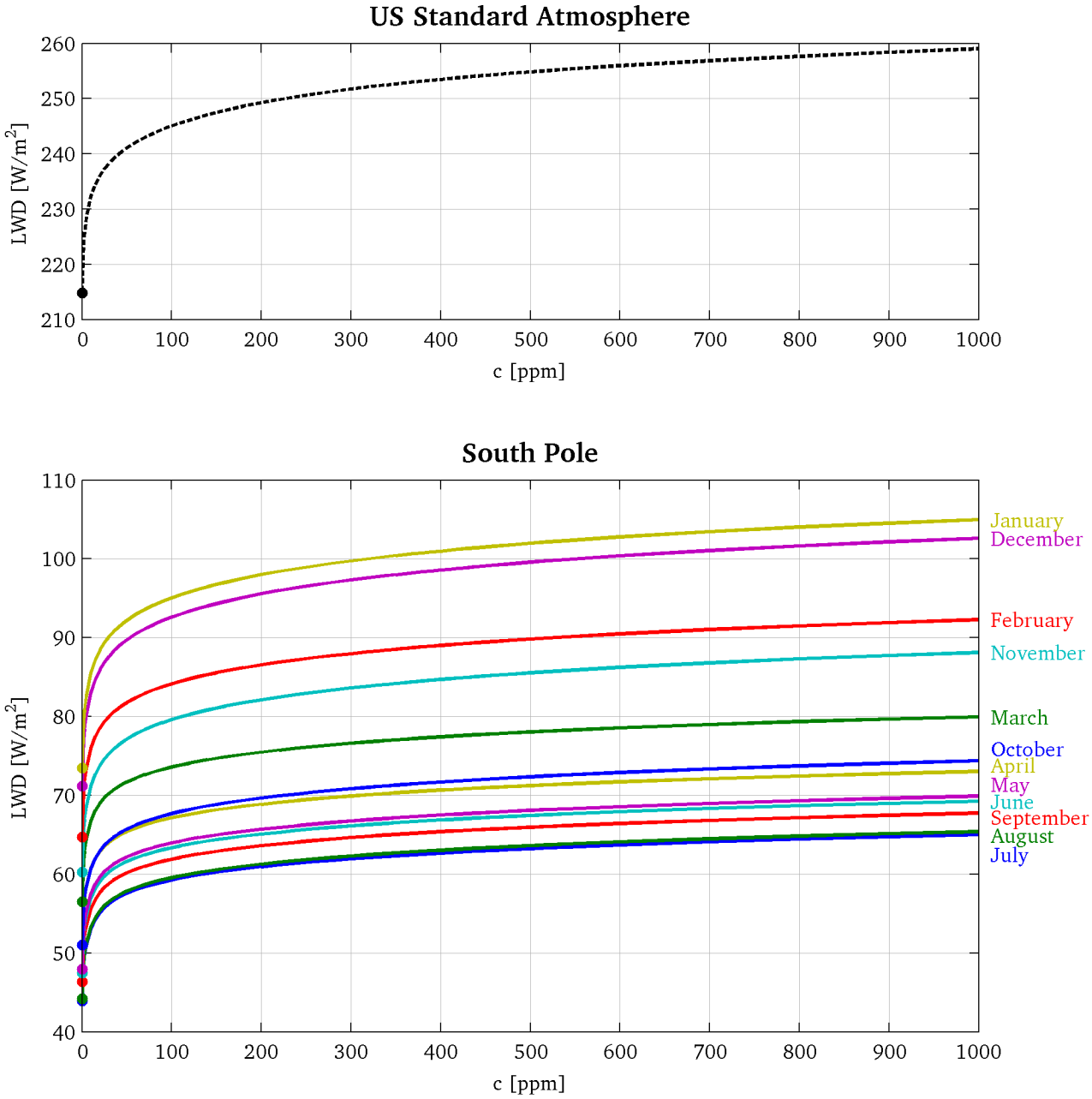

***Figure 2.22**: Long-wave downwelling radiative flux at the surface as a function of CO_2 concentration c. The curves were constructed from spectra calculated with ALFIP, assuming clear sky and typical, south-polar temperature profiles. The dots on the ordinate mark the values for a CO_2 free atmosphere.*

2.4.7 Discussion

Monthly averaged profiles of atmospheric temperature and trace gas concentration were created for conditions typically found in central Antarctica. These profiles were used to quantify the greenhouse effect and the instantaneous radiative forcing of CO_2. This was done with the help of the line-by-line radiative transfer model ALFIP. The calculations represent clear-sky conditions, omit the influence of aerosol on the long-wave radiation, and omit greenhouse gases other than the dominant ones, which are H_2O, CO_2, O_3, CH_4 and N_2O.

Congeneric calculation using the US Standard Atmosphere (1976) were carried out for comparison. Results give a greenhouse effect of CO_2 of some 28 W/m^2, representing the global average. This assumes an atmospheric CO_2 concentration of 380 ppm. Comparing this to values known from literature approves the applied method to estimate the GHE: Schmidt et al. (2010) found 29 W/m^2, using a CO_2 concentration of 339 ppm, whereas Kiehl and Trenberth (1997) published a value of 24 W/m^2 for c = 353 ppm (see also section 2.2.4).

The radiative transfer analysis confirms the occurrence of negative values of the GHE of CO_2 over the central Antarctic plateau. The mechanism behind this phenomenon can be explained from the underlying temperature profile and the resulting TOA long-wave emission spectrum: Most of the atmospheric emission in the CO_2 band originates from the stratosphere, while the TOA emission in the adjacent spectral regions comes predominantly from surface. If the surface is colder than large parts of the stratosphere, then the outgoing long-wave radiative flux to space can exceed the surface emission. This yields a negative GHE.

Altering the CO_2 concentration in the ALFIP model atmosphere gives estimates of the instantaneous radiative forcing of this gas. Again, this was done also for the US Standard Atmosphere (1976) in order to justify the method: AR5 (IPCC 2013) quantifies the stratospheric adjusted radiative forcing of the observed CO_2 increase from approximately 280 ppm in 1750 to 391 ppm in 2011 to be 1.66 W/m^2 ± 0.17 W/m^2. Here, an instantaneous RF of 1.15 W/m^2 for 100 ppm CO_2 increase was found, which corresponds to 1.28 W/m^2 for an increase of 111 ppm (= 391 ppm - 280 ppm). The value is some 23 % lower than the very robust IPCC estimate. On the one hand, this is caused by the great simplifications assumed here. On the other hand, the different measures of RF (instantaneous versus stratospheric adjusted) cannot be expected to yield the same values. Even though the ALFIP results are not directly comparable to the common RF metrics used in the IPCC context, they still illustrate clearly the unique situation of the GHE and RF over central Antarctica.

Clear-sky estimates of LWD provided here for the South Pole range from 63 W/m^2 to 101 W/m^2. They are, on average, some 12 W/m^2 lower than broadband clear-sky measurements reported by Town et al. (2005) for experiments carried out in 2001. The deviations during summer (DJF) are as large as 25 W/m^2, while for the other months the ALFIP results are only between 3 W/m^2 and 12 W/m^2 lower. Town et al. also give monthly estimates of LWD in the spectral region from 5.6 µm to 22.2 µm, collected with a system called *Polar Atmospheric Emitted Radiance Interferometer* (PAERI). Compared to these values, the ALFIP results of the respective spectral region are, on average, 5 W/m^2 lower (8 W/m^2 for January, 10 W/m^2 for February, between 1 W/m^2 and 7 W/m^2 for the other months).

The AFLIP calculations of LWD at the surface for different CO_2 concentrations illustrate the special situation of Antarctica: The strong surface temperature inversion causes decreasing downwelling spectral radiance for increasing CO_2 in the very center of the 15 µm CO_2 band. This is not enough to dominate the overall effect, but LWD on the Antarctic plateau is not as sensitive to changes in the CO_2 concentration as elsewhere on the planet.

2.5 General circulation model analysis

2.5.1 ECMWF experiment with quadrupled CO_2

As a third modelling approach, results from experiments with general circulation models were evaluated in view of the instantaneous radiative effect of increasing CO_2 at TOA. This section presents results from experiments with the atmospheric model of the European Centre for Medium-Range Weather Forecast. The experiments were carried out by Soumia Serrar and Thomas Jung, who kindly supplied the model output data for the analysis presented here.

The ECMWF model was set-up to calculate 15-day forecasts with present-day (*control* run) and quadrupled CO_2 concentrations (*4xCO₂* run). For each month of the years 1989 - 2010 four runs of both CO_2 concentrations were carried out. Except for the CO_2 concentration, the *control* and *4xCO₂* runs started with the same initial conditions. The forecasts for day 15 of all runs were then evaluated and averaged over the 22 years. By comparing results from the *control* run, using present-day CO_2 concentration, to the one with the quadrupled CO_2 one gets an estimate of the effect that instantaneously and drastically increased CO_2 would have on the climate system. This set-up allows fast processes to adjust to the increased GHG, while the climate remains virtually unchanged. This way, the climate forcing of increasing CO_2 can be quantified better, as rapid initial adjustments to the new situation are not taken into account. In the following, resulting TOA radiative fluxes from these experiments are presented.

Figure 2.23 shows the impact that instantaneously quadrupled CO_2 has on the outgoing radiative flux after 15 days into the forecast, averaged over the entire 22 years. The top panel illustrates the total (long- and short-wave) flux change, showing a reduction in energy loss to space everywhere. The greatest decrease is seen over the tropics, with the exception of the ITCZ. Local minima are situated over the Tibetan plateau, Siberia, the Arctic Ocean, Greenland and most pronounced over Antarctica. Most of the total change in TOA radiative flux is attributed to the decreased long-wave emission, which can be seen from the second and the third panels of the figure. The *Long-wave* panel shows basically the same pattern as the top *Total* panel, with three exceptions: 1. The local minima over the ITCZ are more pronounced in the *Long-wave*. This indicates a lower albedo, caused by less or darker clouds. 2. The strong decrease in total outgoing flux off the west-coasts of Africa, North- and South-America are also caused by changes in the short-wave, i.e. from reduced reflection from clouds. Consequently, these maxima are barely seen in the *Long-wave* panel. 3. On the Antarctic plateau the effect of quadrupled CO_2 concentration on the TOA long-wave emission is the smallest on the planet: The change is mostly around 1 W/m^2, with a core region showing slightly negative values. Hence, this GCM experiment shows, that drastically increased CO_2 causes increased long-wave energy loss over a small region in central Antarctica. Nevertheless, the slight cooling effect here is compensated by increased short-wave absorption of some 0.3 W/m^2 over Antarctica.

The zonal mean of these changes in radiative flux are given in figure 2.24. The curves for the *Total* (black) and the *Long-wave* (red) changes show the same asymmetry as the GHE of CO_2 derived from the TES measurements (section 2.2.3, figure 2.6). This demonstrates the strong correlation between greenhouse effect on the one hand, and instantaneous radiative forcing of CO_2 on the other hand.

Finally, figure 2.25 illustrates the total, long- and short-wave TOA flux changes in the southern hemisphere averaged for each season. In spring (panels *SON*), the total effect at TOA is negative over the highest part of Antarctica. This is caused by the increased long-wave energy loss at this time of the year, while the extra short-wave absorption cannot compensate for that. Apart from spring, the summer months also show increased long-wave cooling due to the increased CO_2

(panel *Long-wave - DJF*). However, this is compensated by the short-wave, resulting in a slightly warming total effect. Furthermore, nearly all around Antarctica (at 60°S) during summer the experiments show increased short-wave cooling (panel *Short-wave - DJF*). This suggests increased cloud formation at this latitude, as the ECMWF does not incorporate a dynamical sea ice model.

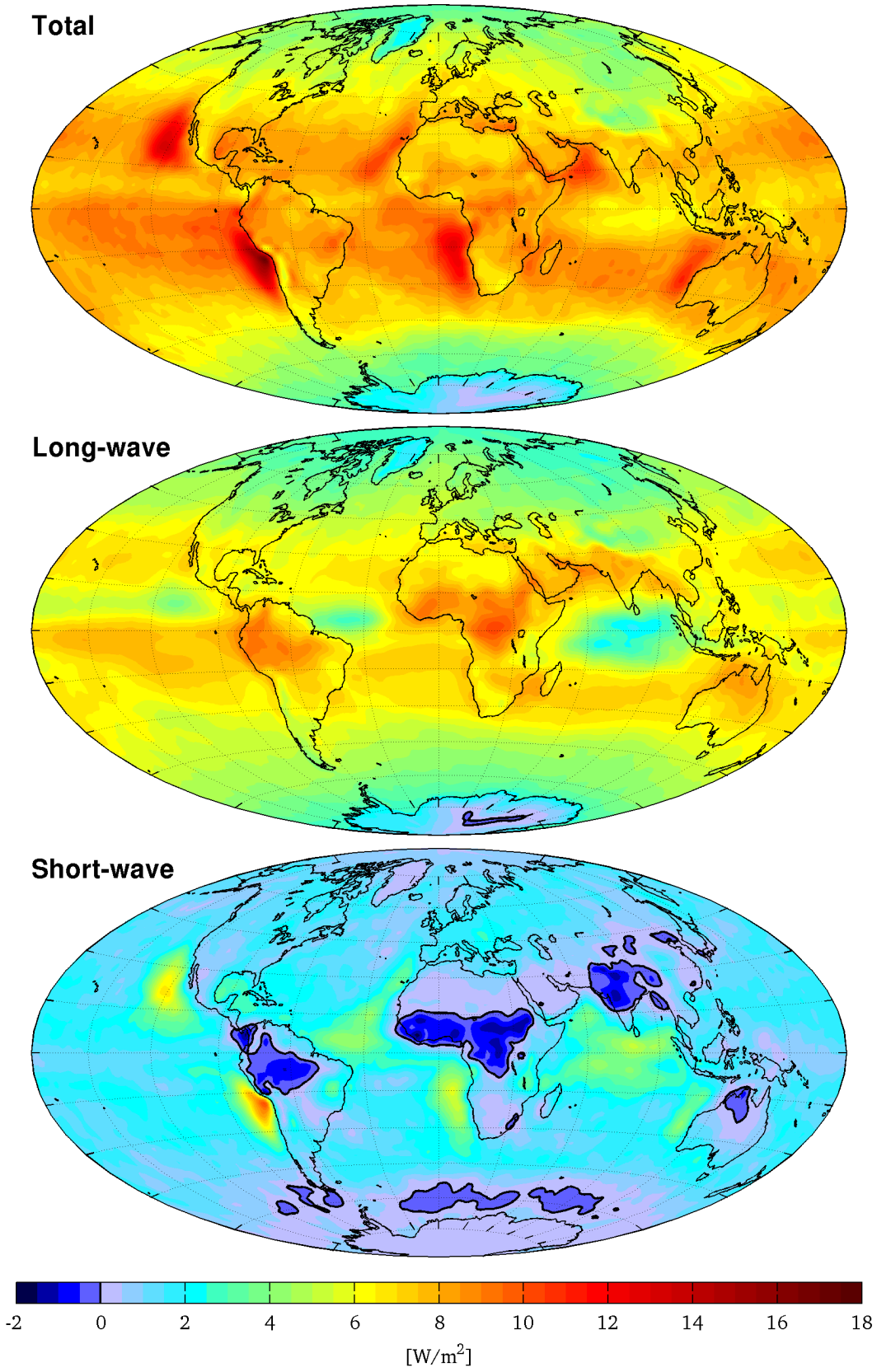

***Figure 2.23**: Changes in TOA outgoing radiative flux 15 days after quadrupling CO_2 in an ECMWF experiment. The fields shown are the differences "control run minus 4xCO_2 run" and were calculated as average over the years 1989 - 2010. The panel **Total** is the sum of **Long-wave** and **Short-wave**. The 0 W/m^2 contour line is drawn in black.*

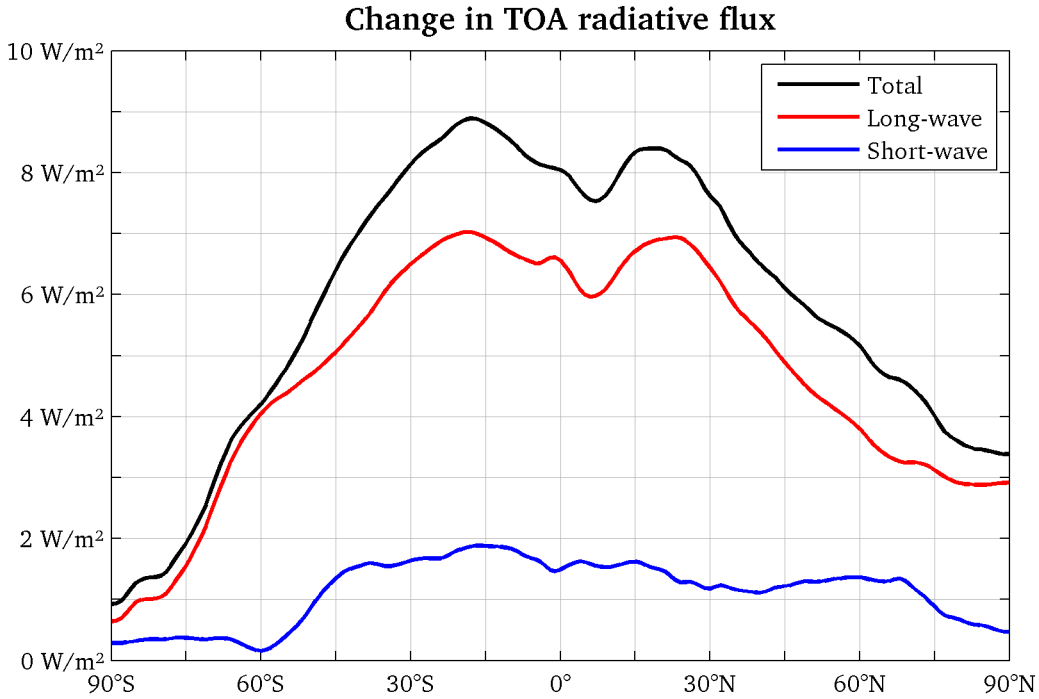

***Figure 2.24**: Zonal mean of changes in TOA outgoing radiative flux 15 days after quadrupling CO_2 in an ECMWF experiment. The differences were calculated as "control run minus 4xCO_2 run", averaged over the years 1989 - 2010.*

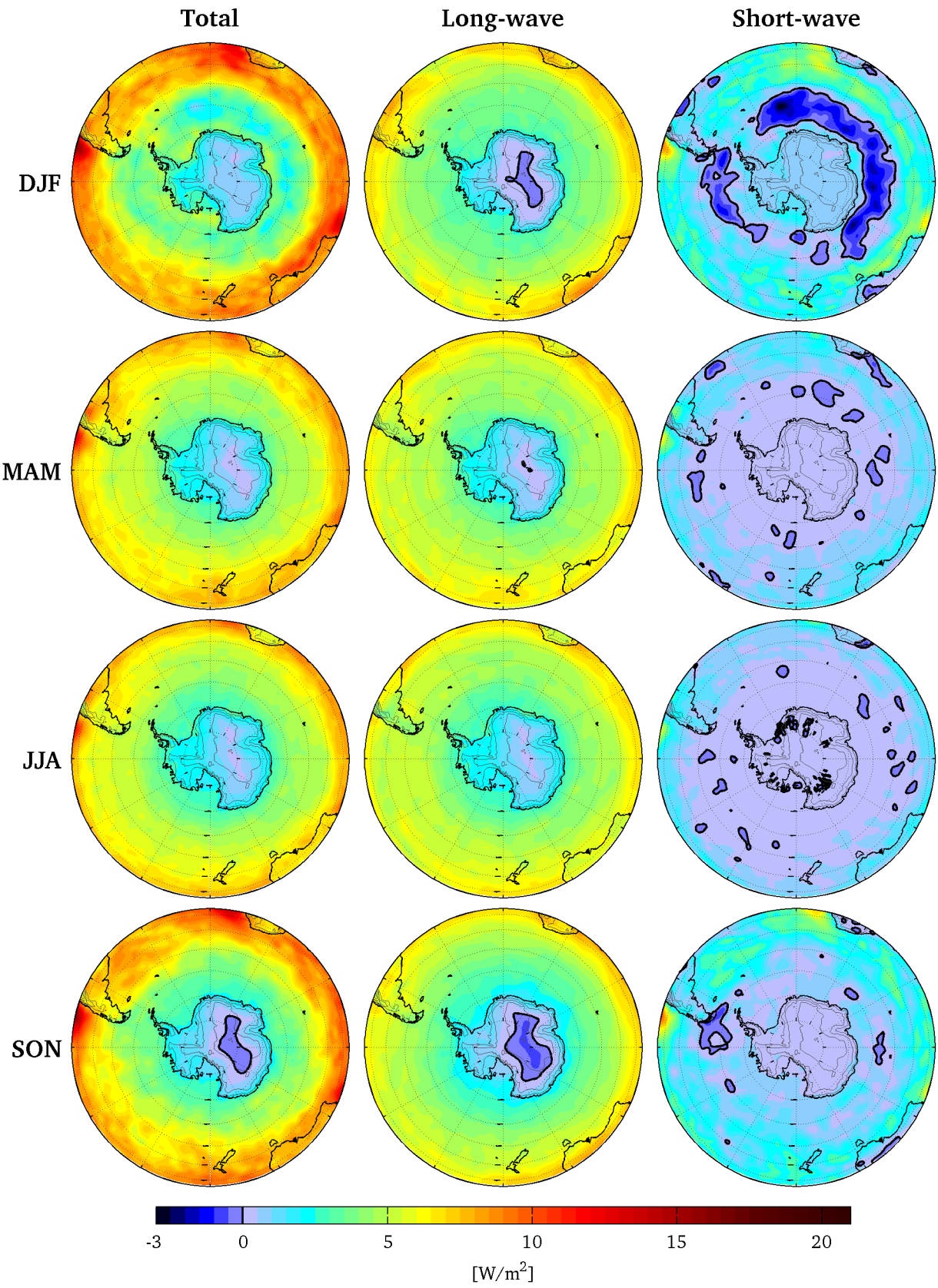

***Figure 2.25**:Changes in TOA outgoing radiative flux 15 days after quadrupling CO_2 in an ECMWF experiment for each season: summer (**DJF**), autumn (**MAM**), winter (**JJA**) and spring (**SON**). The fields shown are the differences "control run minus 4xCO_2 run" and were calculated as average over the years 1989 - 2010. The panels entitled **Total** are the sum of **Long-wave** and **Short-wave**. The black contour lines denote 0 W/m^2. Surface elevation contour lines are shown in 1000 m intervals.*

2.5.2 Climate model intercomparison (CMIP5)

The effect of negative GHE and increasing long-wave emission for increasing CO_2 over central Antarctica should also be notable in current full featured climate models. In order to check this for state of the art models, an evaluation of output from 22 *historical* modelling experiments, which were carried out by various modelling groups for AR5 (IPCC 2013), is presented here. The data were compiled in the 5th phase of the Coupled Model Intercomparison Project (CMIP5) (Taylor et al. 2012) and are provided by various data centres (DKRZ 2014). The so-called *historical* model runs used here mimic the conditions on Earth since 1850, with the external forcings derived from measurements. In this work, the 22 models that were used in the comprehensive analysis of the global energy budget carried out by Wild et al. (2012) (see table 2.3) are compared with BSRN measurements from the South Pole. The BSRN data set utilised for the comparison is the same as described earlier in section 2.4.2.

The top panel in figure 2.26 (*LWU*) compares the modelled surface long-wave upwelling irradiances at the South Pole with BSRN measurements. The monthly averages of the years 1994 until 2005 deviate from the measurements by up to 40 W/m^2, while the multi-model ensemble mean differs not more than 13 W/m^2. It is noteworthy, that the multi-model ensemble mean suggest higher surface temperatures for all months. This might indicate a general problem in modelling the strong Antarctic temperature inversions near the surface.

Table 2.4 reveals more details of the comparison of LWU at the South Pole: It gives the numeric differences of the modelled monthly means for the period 1994 - 2005 to the BSRN data. The numeric data is emphasised by red colouring for warmer surface temperatures in the models, and blue for colder surface values. From this it can be easily seen, that most models overestimate the central Antarctic surface temperatures. The last column of table 2.4 also gives the deviation of the surface altitude to 2827 mASL, but the offsets do not show a coherent dependence on the overestimation of LWU.

Figure 2.26 also shows the modelled surface downwelling long-wave radiation (middle panel, *LWD*) along with the BSRN measurements of this quantity. The ALFIP results from section 2.4.6 are also included for comparison. However, the latter will be dealt with in more detail in section 2.6. The CMIP5 vs. BSRN comparison is similar to the one carried out by Wild et al. (2012), but without the surface adjustment of 2.8 W/m^2 per 100 m surface offset that they have applied. Also, Wild et al. used the period 1985 - 2004 for the model averages, while BSRN data are only available since 1992. Nevertheless, the result is qualitatively the same: The climate models tend to underestimate LWD.

The lowermost panel (*GHE*) of figure 2.26 gives the total greenhouse effect of the CMIP5 models at the South Pole. The monthly averages were calculated as the difference between the upwelling long-wave fluxes at the surface and those at the top of atmosphere. All models feature local minima around March, and some also around September. As for March, most simulations have produced a negative GHE, while in October only few models are below zero, which could be expected from the TES observations (figure 2.8).

Figure 2.27 shows the same parameter, the total greenhouse effect, as multi-model ensemble mean for all Antarctica. March and April are the months with the most negative GHE over central Antarctica. All through the winter, a rather large area of negative GHE remains. In September, the area of negative GHE reaches a weak maximum, before it diminishes. The summer months November till January do not show any areas of negative GHE over Antarctica. The figure only illustrates the situation on the southern hemisphere. In the north, there are no regions with negative GHE.

***Table 2.3**: Climate models used for comparison with BSRN measurements. Of all models, the* historical *runs which were carried out for the 5th IPCC assessment report were used here.*

Model ID	Institute
BCC-CSM1-1	Beijing Climate Center(BCC),China Meteorological Administration,China
CANESM2	Canadian Centre for Climate Modelling and Analysis (CCCma), Victoria, Canada
CCSM4	National Center for Atmospheric Research (NCAR), Boulder, USA
CNRM-CM5	Centre National de Recherches Meteorologiques (CNRM), Meteo-France, Toulouse, France, and Centre Europeen de Recherches et de Formation Avancee en Calcul Scientifique (CERFACS), Toulouse, France
CSIRO-MK3-6-0	Australian Commonwealth Scientific and Industrial Research Organization (CSIRO), Marine and Atmospheric Research, Melbourne, Australia, and Queensland Climate Change Centre of Excellence (QCCCE), Brisbane, Australia
GFDL-CM3	Geophysical Fluid Dynamics Laboratory (NOAA GFDL), Princeton, USA
GFDL-ESM2G	Geophysical Fluid Dynamics Laboratory (NOAA GFDL), Princeton, USA
GFDL-ESM2M	Geophysical Fluid Dynamics Laboratory (NOAA GFDL), Princeton, USA
GISS-E2-H	Goddard Institute for Space Studies (NASA/GISS), New York, USA
GISS-E2-R	Goddard Institute for Space Studies (NASA/GISS), New York, USA
HADCM3	Met Office Hadley Centre, Fitzroy Road, Exeter, United Kingdom
HADGEM2-CC	Met Office Hadley Centre, Fitzroy Road, Exeter, United Kingdom
HADGEM2-ES	Met Office Hadley Centre, Fitzroy Road, Exeter, United Kingdom
INMCM4	Institute for Numerical Mathematics (INM), Moscow, Russia
IPSL-CM5A-LR	Institut Pierre Simon Laplace (IPSL), Paris, France
IPSL-CM5A-MR	Institut Pierre Simon Laplace (IPSL), Paris, France
MIROC-ESM	Japan Agency for Marine-Earth Science and Technology (JAMSTEC), Kanagawa, Japan, and Atmosphere and Ocean Research Institute (AORI), The University of Tokyo, Chiba, Japan, and National Institute for Environmental Studies (NIES), Ibaraki, Japan
MIROC4H	Atmosphere and Ocean Research Institute (AORI), The University of Tokyo, Chiba, Japan, and National Institute for Environmental Studies (NIES), Ibaraki, Japan, and Japan Agency for Marine-Earth Science and Technology (JAMSTEC), Kanagawa, Japan
MIROC5	Atmosphere and Ocean Research Institute (AORI), The University of Tokyo, Chiba, Japan, and National Institute for Environmental Studies (NIES), Ibaraki, Japan, and Japan Agency for Marine-Earth Science and Technology (JAMSTEC), Kanagawa, Japan
MPI-ESM-LR	Max Planck Institute for Meteorology, Hamburg, Germany
MRI-CGCM3	Meteorological Research Institute (MRI), Tsukuba, Japan
NORESM1-M	Norwegian Climate Centre, Norway

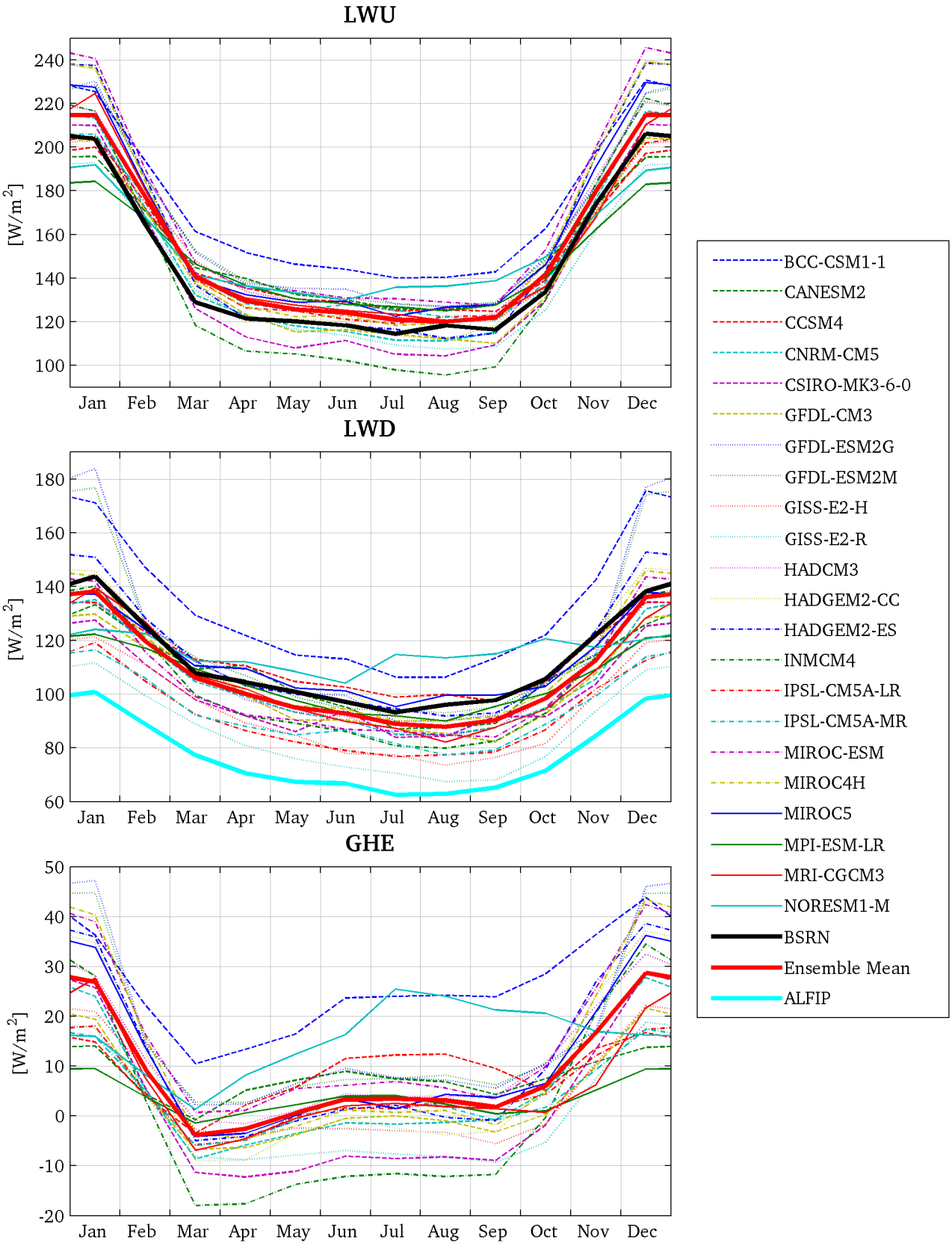

***Figure 2.26**: Comparison of CMIP5* historical *climate model results with BSRN data from the South Pole. Shown are monthly means for the period 1994 - 2005. Panel **LWU**: Surface long-wave upwelling irradiance. Panel **LWD**: Surface long-wave downwelling irradiance. The line* ALFIP *included here shows the values from figure 2.22 for $c = 380$ ppm, which are clear-sky calculations. Panel **GHE**: Total greenhouse effect calculated as difference between the surface and top of atmosphere upwelling long-wave irradiance (only CMIP5 model results).*

***Table 2.4**:Comparison of long-wave surface emission at the South Pole from 22 CMIP5 models with BSRN measurements for the years 1994 till 2005. The monthly averaged differences listed in the columns **Jan** till **Dec** were calculated as "CMIP5 minus BSRN". The colouring of the cells indicates whether a monthly average is above or below the BSRN value: red shading indicates positive values up 40 W/m², blue shading numbers down to -23 W/m². Columns **Mean** and **σ** give the mean difference and standard deviation for each model. Columns entitled $N_{>0}$ and $N_{<0}$ list the number of monthly means above and below zero respectively. The **Surface Offset** is the difference in surface elevation of the grid point at 90°S to the value 2827 mASL. The rows **Mean**, **σ**, $N_{>0}$, and $N_{<0}$ give the according statistical values for each month. The models are ordered by the mean difference (column* Mean*).*

	Jan	Feb	Mar	Apr	May	Jun	Jul	Aug	Sep	Oct	Nov	Dec	Mean	σ	$N_{>0}$	$N_{<0}$	Surface Offset
	[W/m²]												[W/m²]				
BCC-CSM1-1	+22	+29	+32	+30	+26	+26	+26	+22	+27	+29	+24	+24	+26	3	12	0	-251 m
MIROC-ESM	+37	+25	+18	+14	+14	+13	+16	+11	+11	+19	+26	+40	+20	10	12	0	-181 m
GFDL-ESM2G	+26	+22	+23	+16	+15	+17	+14	+9	+12	+16	+9	+19	+16	5	12	0	+21 m
GFDL-ESM2M	+25	+22	+24	+17	+14	+12	+14	+9	+13	+15	+8	+18	+16	5	12	0	+21 m
MIROC5	+24	+17	+11	+11	+9	+11	+8	+8	+11	+12	+17	+23	+14	5	12	0	+74 m
MIROC4H	+32	+19	+10	+5	+2	+4	+4	+1	+5	+13	+22	+33	+13	11	12	0	-7 m
HADGEM2-ES	+34	+22	+8	+0	+0	-0	+2	-6	-2	+9	+22	+32	+10	14	9	3	-26 m
HADGEM2-CC	+32	+20	+5	-2	+1	+2	-1	-7	+2	+10	+25	+34	+10	14	9	3	-26 m
HADCM3	+13	+14	+14	+7	+4	+7	+6	+1	+8	+13	+12	+15	+9	4	12	0	-119 m
NORESM1-M	-12	+3	+13	+15	+13	+12	+21	+18	+22	+16	-5	-17	+8	13	9	3	+25 m
MRI-CGCM3	+21	+16	+11	+9	+7	+7	+9	+2	+6	+3	-6	+4	+7	7	11	1	+33 m
CANESM2	-8	+6	+16	+18	+12	+12	+11	+7	+11	+13	-0	-11	+7	9	9	3	-149 m
CCSM4	-4	+7	+13	+14	+10	+11	+11	+7	+8	+5	-4	-9	+6	7	9	3	-2 m
IPSL-CM5A-MR	+2	+12	+11	+7	+5	+10	+11	+4	+5	+4	-0	-0	+6	4	10	2	-11 m
GISS-E2-H	-1	+14	+19	+12	+9	+6	+8	+2	+4	+2	-2	-4	+6	7	9	3	+38 m
IPSL-CM5A-LR	+1	+10	+11	+5	+5	+3	+5	+4	+6	+6	+1	-4	+4	4	11	1	-91 m
MPI-ESM-LR	-20	+2	+17	+15	+10	+10	+12	+7	+11	+6	-12	-23	+3	14	9	3	+60 m
CNRM-CM5	+9	+7	+3	+1	-2	-3	-3	-7	-1	+2	+2	+11	+2	5	7	5	+18 m
GFDL-CM3	-1	+7	+9	+2	-5	-2	-0	-6	-6	-2	-4	-2	-1	5	3	9	+20 m
CSIRO-MK3-6-0	+6	+3	-3	-9	-12	-7	-9	-14	-7	-4	-1	+4	-4	6	3	9	-45 m
GISS-E2-R	-11	+1	+6	+1	-4	-5	-5	-11	-8	-8	-12	-14	-6	6	3	9	+41 m
INMCM4	+13	+3	-11	-15	-15	-16	-17	-23	-17	-4	+10	+16	-6	13	4	8	-20 m
Mean [W/m²]	+11	+13	+12	+8	+6	+6	+6	+2	+6	+8	+6	+9					
σ [W/m²]	17	8	9	10	9	9	10	10	10	9	12	18					
$N_{>0}$	15	22	20	19	17	16	16	15	16	18	12	13					
$N_{<0}$	7	0	2	3	5	6	6	7	6	4	10	9					

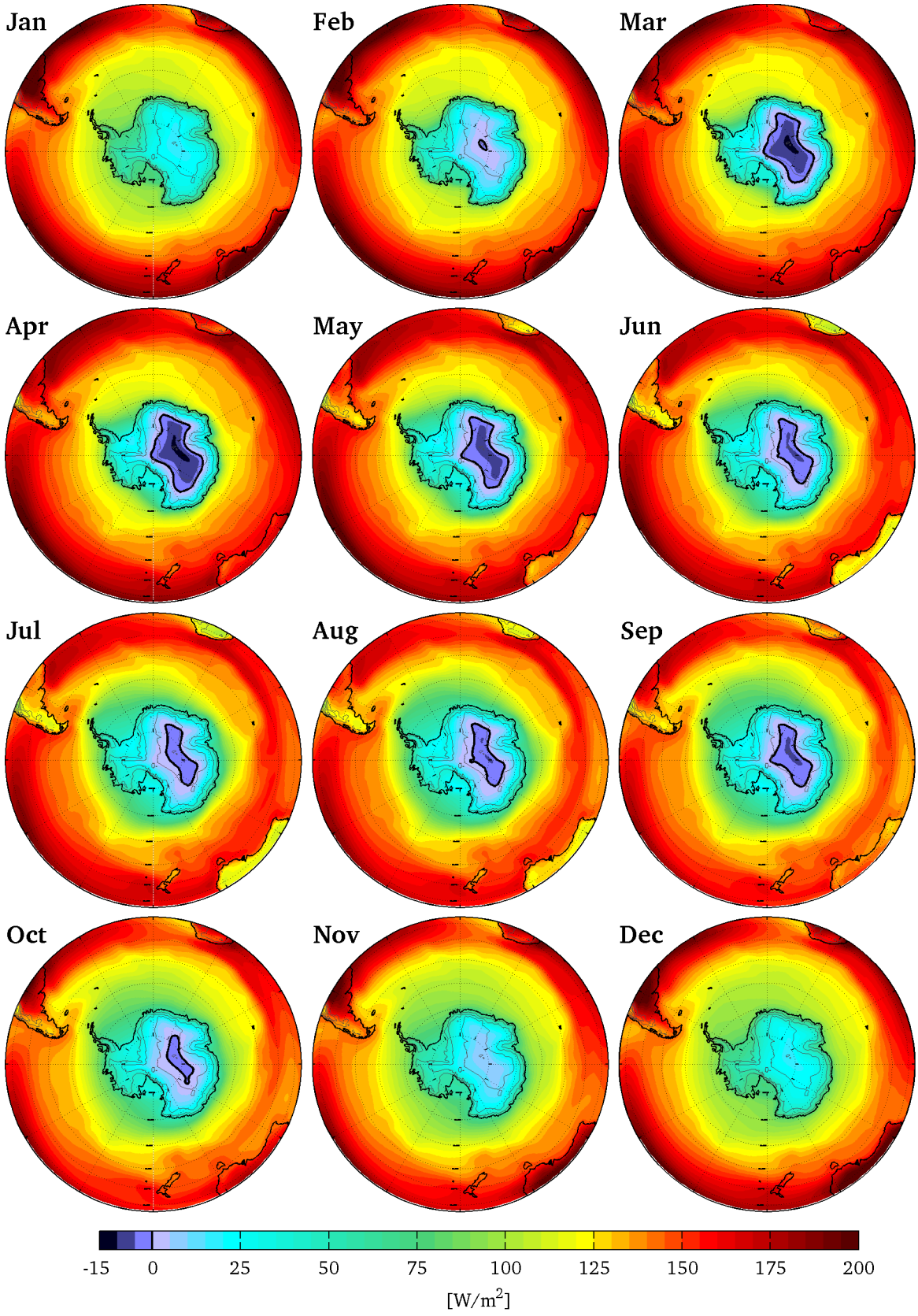

***Figure 2.27**: Ensemble mean of total greenhouse effect from 22 CMIP5* historical *model simulations for the years 1994 till 2005. The monthly averages were calculated as difference between the surface and top of atmosphere upwelling long-wave irradiance. The black contour lines denote 0 W/m^2. Surface elevation contour lines are shown in 1000 m intervals.*

2.5.3 Discussion

Most CMIP5 models investigated here suggest more surface upwelling long-wave radiation than the BSRN data at the South Pole. Some CMIP5 models have substantial differences in the orography of central Antarctica, which consequently influences the surface temperature and hence the long-wave emission. Even though the two warmest models, namely *BCC-CSM1-1* and *MIROC-ESM,* have the lowest surface at the South Pole with an offset of -251 m and -181 m respectively, this cannot serve as an explanation for general overestimation of LWU: One reason for this is the fact that the 3rd, 4th and 5th warmest models in the list (table 2.4), showing mean differences in LWU between 14 W/m^2 and 16 W/m^2, have a higher surface than 2827 mASL with offsets up to +74 m. Furthermore, the two models *HADCM3* and *CANESM2* also have substantial differences in the surface elevation (-119 m and -149 m respectively) but are not among the “warmest” models. A third indication is the difference in the long-wave downwelling flux: If the differences in surface elevation caused LWU to be overestimated, the same should apply to LWD, but LWD is generally underestimated.

The CMIP5 results confirm the occurrence of a negative GHE over the Antarctic plateau. The analysis also identified autumn as the season with the most pronounced occurrence of the phenomenon. Furthermore, they confirm that Antarctica is the only place on the planet, where such cold surface temperatures are reached to allow a negative GHE.

Nevertheless, the surface temperature in the GCMs tends to be too warm on the Antarctic plateau, in comparison with the BSRN measurements. This results in an overestimation of LWU, while the atmospheric emission seems to be underestimated in the CMIP5 models (shown here only for the surface LWD-flux though). GHE is essentially “absorbed surface emission minus atmospheric emission”. Therefore, with the surface emission being too high, and the atmospheric emission being potentially too low, it is not surprising that the GHE of the CMIP5 models is not as negative as could be expected from the TES findings.

Furthermore, the above tendencies of the CMIP5 long-wave fluxes hint towards a potential overestimation of the instantaneous radiative forcing induced by rising CO_2 concentration in central Antarctica. The forcing has been known to be small there (Hansen et al. 2005), but it might actually be slightly negative.

The ECMWF results also confirmed the mechanism of negative GHE over the Antarctic plateau and the resulting long-wave cooling for increasing CO_2. However, the cooling in the long-wave is compensated by increased short-wave warming, yielding an overall energy gain for the entire planet. Like the CMIP5 models, the ECMWF experiments also overestimate the surface temperature on the Antarctic plateau. And again, as for the CMIP5 results, this fact is capable to cause an underestimation of the increased long-wave cooling. Hence, whether increasing CO_2 causes instantaneous radiative warming or cooling over the Antarctic plateau cannot ultimately be concluded from these experiments.

2.6 Comparison of measurements and models

Greenhouse effect (GHE)

Satellite observations (figure 2.5), simple two-layer model considerations (equation 2.11), radiative transfer calculations (table 2.2), and climate model runs (figures 2.26 and 2.27) all show that the greenhouse effect can be negative. This assumes the GHE to be defined as the difference between the surface and TOA long-wave emission.

The magnitude of the different estimates of the GHE of CO_2 over Antarctica which are presented here are consistent: The monthly averaged satellite measurements shown in figure 2.8 which are south of 78°S and in the altitude range comparable to the South Pole (between 2700 mASL and 2900 mASL) range from -2.7 W/m^2 (in March) to 3.9 W/m^2 (in June). As seen from table 2.2, the GHE of CO_2 from the South Pole simulations with ALFIP are between -2.9 W/m^2 in March and 3.4 W/m^2 in December. The evaluation of the CMIP5 data (panel *GHE* in figure 2.26) reveals estimates of the *TOTAL* GHE at the South Pole (monthly averages) between -18 W/m^2 to 47 W/m^2 for all individual models, and between -4 W/m^2 and 29 W/m^2 for the ensemble mean. Schmidt et al. (2010) estimate the contribution of CO_2 to the total globally averaged GHE of 155 W/m^2 to be some 19 %. Hence, the ranges of the CMIP5 data at the South Pole would translate to -3.4 W/m^2 to 9.0 W/m^2 as GHE of CO_2 for the individual models and to -0.7 W/m^2 to 5.4 W/m^2 for the ensemble mean. Again, this hints towards a slightly overestimated GHE for the CMIP5 ensemble mean.

Considering the global distribution of the GHE as determined from satellite (figure 2.5) and from the CMIP5 *historical* model runs (figure 2.27) confirms that negative values of GHE only occur over the East Antarctic ice sheet. This holds true for monthly and longer averages.

The seasonality of the GHE over central Antarctica as determined from satellite (figure 2.8) resembles the ALFIP line-by-line model results (table 2.2) in some respect: The TES results identify austral autumn (specifically February till May) as the season with the most negative GHE over the Antarctic plateau. This is confirmed by the ALFIP calculations: They indicate negative values during February, March and April at the South Pole. The other minimum in GHE occurs around October in both analyses, again slightly more pronounced in the TES results. A noteworthy difference between the two estimates of GHE occurs in summer: While the satellite results show a remaining area of negative GHE during December and January (which hardly occurs in winter), the ALFIP calculations indicate the highest values during these months, clearly exceeding the winter values.

A plausible reason for this difference might by the fact that the method used in the TES estimate is influenced by clouds, while the ALFIP results imply clear sky. In summer, the GHE (i.e. TOA emission spectra) over Antarctica is qualitatively close to what it is elsewhere on the planet. This bases on a comparable warm surface, clouds which are colder than the surface, and the stratosphere being yet colder. This kind of temperature distribution yields an underestimation by the TES method to determine the GHE, which is not as pronounced in winter (see table 2.1).

Radiative forcing (RF)

The two layer model consideration (equation 2.12) presented here, radiative transfer calculations (table 2.2), and ECMWF results (figures 2.23 and 2.24) all show *QUALITATIVELY* that increasing atmospheric CO_2 can force an increase in long-wave energy loss to space for conditions typical for central Antarctica.

The two layer model and ALFIP results give the *instantaneous radiative forcing* - the instantaneous change in TOA emission for a given change of the atmospheric CO_2 concentration.

Only the ALFIP results give *QUANTITATIVE* estimates of the instantaneous RF for central Antarctica. Hence, besides the qualitative agreement of the two layer model and ALFIP, a numerical, quantitative comparison cannot be carried out here.

The ECMWF experiment provides a quantity which is known as *effective radiative forcing* in the IPCC context. This differs from the instantaneous RF and the previously favoured *stratospheric adjusted radiative forcing* in the level of adjustments allowed in the model runs, before the changes in the radiative fluxes are determined (Hansen et al. 2005; IPCC 2013, chapter 8.1). So, even though instantaneous RF from the ALFIP results and effective RF from the ECMWF cannot be compared numerically, some parallels in the qualitative course through the year can be drawn:

Both ALFIP and ECMWF analyses show the largest, but still comparably small, positive radiative forcing in central Antarctica during winter (see *South Pole May* till *August* in table 2.2 and panel *Long-wave - or Total - JJA* of figure 2.25). The strongest cooling, i.e. negative RF associated with increasing CO_2, on the plateau seems to occur in spring. Again, this is indicated both by the ALFIP and ECMWF results. The summer also shows consistent negative RF in the long-wave, extending to April in the ALFIP analysis.

The flux change in the short-wave induced by increasing CO_2 is considered only in the ECMWF analysis. There, it compensates the long-wave slight cooling effect seen over the Antarctic plateau when considering the yearly average. Since the other methods applied do not regard the short-wave effects, a comparison of this spectral range is not possible here.

Correlation of GHE with RF

The greenhouse effect of CO_2 is strongly correlated with the radiative forcing induced by changes in the concentration of this greenhouse gas. This can be seen from spectra like the ones shown in figure 2.18: Increasing CO_2 essentially *WIDENS* the absorption band, and hence widens the relative emission minima seen in the TOA spectra. So the (instantaneous) decrease in long-wave emission depends mainly on the *DEPTH* of the local emission minimum, as the actual minimum value does not change all that much. Consequently, a large GHE implies a large RF.

When comparing the spacial distribution of the greenhouse effect from the TES measurements (figure 2.5, panel *All*) with the radiative forcing of the ECMWF results (figure 2.23, panel *Total* or *Long-wave*) a strong correlation between the two quantities becomes apparent. The general pattern of the two analyses matches: The highest values are seen over the tropics, with the exception of the ITCZ. Towards the poles, both GHE and RF decrease. Local minima in the northern hemisphere are seen over Greenland, Siberia, the Arctic Ocean (only ECMWF, TES lacks data there) and the Tibetan plateau. In the southern hemisphere Antarctica stands out with the lowest GHE and RF on the globe. The negative GHE observed by TES also correlates well with the long-wave cooling demonstrated in the ECMWF plot.

The asymmetry of the GHE between the two hemispheres seen by TES (figure 2.6) also resembles the according plot of RF from the ECMWF analysis (figure 2.24). Both curves show a steep incline from the South Pole to about 20°S, decreasing from there to about 6°N, increasing again up to 20°N, and declining steeply towards the North Pole. Also common to both parameter is the fact that the values in the Antarctic are lower than in the Arctic. What differs are the relative maxima at 20°S and 20°N: While the GHE is stronger in the north, the RF is stronger in the south.

The correlation of GHE with RF is not that apparent in the seasonal changes seen in the satellite measurements (figure 2.7, panels showing the southern hemisphere) and the ECMWF estimates (figure 2.25, panels *Long-wave*). Even though the GHE and RF over the Southern Ocean are both stronger in austral autumn and winter, while the months September till February show lower

values, there are some distinct differences: The summer minimum over the Southern Ocean seen in the GHE (panel *DJF*), appears earlier in the ECMWF forcing plot (panel *Long-wave - SON*). Presumably, this is due to the determination of GHE applied here: It uses the top of cloud temperature as reference, if sufficiently thick clouds are present. During the months with an ice-free ocean there are probably the most clouds of all seasons (figure 2.25, panel *Short-wave - JJA* indicates this). Hence, the GHE is biased towards lower values in summer.

Another substantial difference between GHE and RF can be seen over the Antarctic continent: The GHE reaches a pronounced minimum during austral autumn, which is evident in the TES data (figure 2.7) as well as the CMIP5 ensemble mean (figure 2.27). This autumn minimum is not seen in the radiative forcing, neither in the ECMWF estimate (figure 2.25) nor the ALFIP results (table 2.2). Clouds, which typically cause short-wave cooling, do not seem to be the reason for the mismatch in this case (figure 2.25, panel *Short-wave - JJA* vs. *DJF*). Instead, looking at the typical temperature profile of the central Antarctic atmosphere in autumn (figure 2.13, panel *March*) reveals the reason for the RF being close to zero: The stratospheric temperatures up to ~25 km are fairly constant. Consequently, the TOA emission cannot change as much (figure 2.18) as, for instance, in October, when the stratospheric inversion reaches from the stratopause down, well below 20 km.

Surface long-wave downwelling radiation (LWD)

The clear-sky ALFIP calculations of LWD at the surface (section 2.4.6) clearly underestimate the radiative flux at the South Pole. This is seen in the comparison with BSRN measurements and CMIP5 climate model estimates (figure 2.26, panel *LWD*). The values determined with ALFIP are, on yearly average, some 35 W/m^2 lower than the measurements, ranging between 43 W/m^2 difference in summer and 30 W/m^2 in winter. About 13 W/m^2 can be explained with the lack of clouds in the simulations: When filtering the BSRN LWD measurements for clear-sky observations, the average during the months with sunlight (October till February) drops from more than 132 W/m^2 (all sky) below 120 W/m^2 (clear sky). The criterion used here for *clear sky* is that the surface short-wave downwelling radiation is within the range 84 % ± 7.5 % of the incoming solar radiation at TOA. This range was chosen from minimising the clear-sky LWD average reading, through altering both the range's center and width. The filter range of the clear-sky criterion does not influence the clear-sky LWD value greatly. If the so-determined summer value of cloud influence of 13 W/m^2 is taken to be representative for the winter also, then the remaining 22 W/m^2 must be attributed to the greenhouse gases not included in the ALFIP modelling and to aerosol. Town et al. (2007) estimated the cloud's contribution to LWD at the South Pole to be around 18 W/m^2, which would leave some 17 W/m^2 for the GHGs and aerosol not modelled with ALFIP.

Chapter 3: Conclusion and outlook

3.1 A thought experiment on negative greenhouse effect

The term *negative GHE* might seem to sound odd, as we think of GHGs to act like a blanket for the planet, shielding terrestrial radiation from being emitted to space. “Anti-shielding” does not make sense. The following thought experiment demonstrates that GHGs can actually help the planet to lose energy, that would not be emitted without them:

> Say, there were no GHGs in the Earth's atmosphere. Clouds shall be neglected as well, to make things easier. The planet gains energy over the tropics (positive budget) and loses this extra energy over the poles (negative budget). The energy transport in-between is carried out by the atmosphere. The ocean, of course, also contributes to this meridional transport of energy, but this is not of importance here.
>
> The energy gained over the tropics, which is then transported to the poles, must enter the ground in the polar regions before it can be emitted to space. This is because no GHGs and no clouds, also no aerosol, shall be contained in this hypothetical atmosphere. The atmosphere cannot emit energy directly to space, as it lacks long-wave emitters. Consequently, any “imported” energy that shall leave the Earth-atmosphere system in the polar regions, must be transported via sensible heat flux into the ground. From there it can then be emitted to space.
>
> Now, GHGs shall be introduced. Sure, they have a “shielding” effect over the tropics by causing long-wave downwelling radiation to heat the surface. The same happens, to some smaller extent though, in the polar regions. In addition to that, GHGs give the atmosphere the ability to emit energy directly into space, without the need to transport it through the surface first. This increases the ability of the planet to get rid of energy at the poles, which has been collected over the tropics. In essence, this helps the atmosphere to perform its “task” of meridional energy transport; GHGs help to balance the radiative imbalance between the tropics and the poles.

The conditions in central Antarctica, being a high-altitude plateau and having a continental climate, are such, that the “shielding” effect of GHGs is excelled by the “helping in losing energy” effect. This, one can name *negative greenhouse effect*.

3.2 Greenhouse effect of CO_2 over Antarctica

The work presented here shows that GHGs, particularly CO_2, frequently cause relative maxima in the TOA long-wave emission over a core region on the East Antarctic plateau. This is referred to as negative GHE, as these emission maxima correspond to a TOA radiative flux exceeding the long-wave emission of the underlying surface. Besides Antarctica, such emission spectra occur over high-reaching clouds, particularly over the ITCZ, and very occasionally in the Arctic over Siberia or Greenland. The Antarctic plateau is the only place on the planet with monthly averaged GHE of CO_2 below zero. This is shown with the help of satellite observations of long-wave TOA emission spectra.

The satellite data also revealed the seasonal variations of the phenomenon of negative GHE over central Antarctica: It is most pronounced in austral autumn, with its peak in March. At this time of the year, the surface has cooled off drastically, while the stratosphere is still relatively warm. This temperature distribution yields the TOA emission maxima in the CO_2 band, as the long-wave emission to space of CO_2 originates mostly from the stratosphere. In winter, namely form June till August, the surface has not cooled down much more, but the stratosphere has. Therefore, in winter the GHE is typically positive as everywhere else on the planet. In spring, mainly October, the stratosphere warms up rapidly, while the surface is still comparably cold. Again, the GHE reaches negative values, but not as low as in autumn. In summer, the satellite observations also show slightly negative values.

The occurrence and seasonal course of negative GHE over central Antarctica were confirmed from line-by-line radiative transfer calculations; with one exception: In summer the RT calculations show the greatest (positive) GHE, while the satellite data indicate slightly negative values. This is most likely due to the method used to determine GHE from satellite and the presence of clouds: For the determination of GHE, the long-wave surface emission must be estimated. In the satellite analysis, this is done by assuming the spectral radiance seen in an atmospheric window to represent the surface emission. Under cloudy conditions, this is actually the top of cloud emission. In summer, the clouds' top temperatures are well below the surface temperature, which is not the case for the rest of the year. Consequently, the deviation between the satellite analysis and the RT calculation is greatest in summer.

Considerations with a simple two layer model could affirm the occurrence of a negative GHE for conditions typical for central Antarctica. Additionally, climate model runs from CMIP5 were evaluated and found to support above findings.

The satellite observations of GHE of CO_2 revealed a pronounced asymmetry between the two hemispheres: Generally, the GHE is largest over the tropics, with maxima at 20°S and 20°N, and a local minimum at 6°N, caused by the clouds in the ITCZ. Towards the poles, the GHE drastically declines, approaching about one third of its peak value in the north, and zero in the south. Another difference found between the two hemispheres is the discrepancy between day- and night-time observations outside the tropics: In the south, there are virtually no differences in the GHE of CO_2 between day and night. This is not the case in the north: Here, there is a distinct daily cycle, which is most likely due to the greater fraction of land area on the northern hemisphere.

3.3 Instantaneous radiative forcing of CO_2 over Antarctica

The unique situation of Antarctica regarding the GHE is also seen in the RF of CO_2. Considering TOA long-wave emission spectra associated with negative GHE suggests that increasing CO_2 would yield, instantaneously, a negative radiative forcing on the earth-atmosphere system. This assumption is confirmed by a simple two layer model: If the temperature of the surface is below the temperature of the atmosphere, an increase in GHGs results in increasing long-wave energy loss to space. Line-by-line RT calculations for south-polar clear-sky conditions also confirm a weak, but negative instantaneous RF of CO_2. The effect is on the order of -0.1 W/m^2 per 100 ppm increase in CO_2, whereas comparable calculations for the global average give a RF well above 1 W/(m^2 100ppm). Experiments with the ECMWF model also show a negative forcing effect of increasing CO_2 in the long-wave. However, in these experiments, the negative RF in the long-wave is mostly compensated for by additional short-wave absorption. Still, the ECMWF results show, that the RF of increasing CO_2 is exceptionally low over Antarctica.

The instantaneous RF of CO_2 is strongly coupled with the GHE of this atmospheric species. Comparing the global distribution of annually averaged estimates of these two parameter demonstrates the strong correlation. Also, the hemispheric asymmetry seen in the GHE is clearly evident in the RF estimates presented here. The coupling between GHE and RF in Antarctica is not as pronounced when considering seasonal changes: In particular, the autumn minimum in GHE is not evident in the RF. The reason for this is the fairly homogenous temperature distribution in the south-polar stratosphere at this time of the year: In the center of the 15 µm absorption band of CO_2 the atmosphere is opaque. The absorption and emission is that strong, that, when seen from above, the effective emission height lies in stratosphere. An increase in emissivity results in increasing emission from higher layers. Hence, when the temperature is approximately constant in this altitude range, TOA emission does not change greatly with increasing CO_2.

3.4 Effect of CO_2 on LWD under strong inversion conditions

Analysis known from literature of surface temperature of the Antarctic have shown no statistically significant warming on the East Antarctic plateau (see section 1.5). The region might even have cooled slightly since the IGY in 1957/58. The analyses concerned with GHE and RF do not provide a direct link to surface temperature. For this, line-by-line RT simulations of the surface downwelling long-wave radiation were carried out for south-polar conditions.

Clear-sky radiative transfer calculations show that, at the South Pole, LWD increases with increasing CO_2, just as everywhere else on the planet. This holds true for all months of the year. However, the strong surface temperature inversion, which is typically present over the Antarctic plateau, causes LWD to increase not as greatly as elsewhere.

This somewhat smaller increase in LWD can be explained when considering the spectral changes induced by increasing CO_2: In some spectral regions, where absorption and emission is particularly strong, the contribution to the LWD-flux can decrease with increasing long-wave opacity. This is due to the lower emission height, associated with increasing concentrations of GHGs. If the emission height lies within the temperature inversion layer, lower emission height means emission at a lower temperature, and hence a decreasing LWD.

3.5 Outlook

The work presented here contributes to explain the non-warming of East Antarctica. Results focus on the GHE and RF of CO_2. The general spacial pattern of the non-warming coincides with the areas of negative GHE and negative RF. However, the direct link between the unique radiative features of central Antarctica and Antarctic surface temperatures is not shown.

A better linkage between the reported phenomena and the widely discussed surface temperature can be provided from analyses of GCM results. For this, it is crucial that the surface temperatures on the Antarctic plateau are modelled correctly. The CMIP5 comparison shown here demonstrates that this is not the case for many state-of-the-art climate models: most models evaluated here overestimate the surface temperature. Consequently, many models do not reproduce the observed negative GHE over central Antarctica. Furthermore, GCM analyses shall ensure that the surface temperature inversion is correctly reproduced. Both the strength and the height of the inversion influence the changes in LWD caused by increasing GHGs. If the surface inversion is too weak in a model, the increase of LWD caused by increasing GHGs will be overestimated.

Further observational proof of the phenomena reported here could be gained from long-term analysis of TOA thermal infrared emission spectra. Satellite records of such measurements date back to the launch of the *Nimbus 4* satellite in 1970. Given the comparability of the different sensors, that have been in space since then, and given sufficient data coverage, a correlation of GHE of CO_2 over central Antarctica with the atmospheric CO_2 concentration should be feasible. This kind of analysis is expected to resemble the results of RF of CO_2 presented here, essentially showing no or slightly negative correlation.

A promising observational record to further evaluate the effects of increasing GHGs on LWD on the Antarctic plateau is collected at Concordia Station at Dome C. The *Istituto Nazionale di Ottica* (INO-CNR), Italy runs an infrared spectroradiometer called *Radiation Explorer in the Far InfraRed - Prototype for Applications and Developments* (REFIR-PAD) on an operational basis since 2011 (Palchetti et al. 2014; Palchetti and Bianchini 2014). The instrument covers nearly the entire long-wave spectrum, namely from 7 µm to 100 µm. Earlier experiments at the South Pole provided similar data, but were run only for periods up to one year (Myers 2000; Smith and Harper 1998; Van Allen et al. 1996; Walden et al. 1998). A long-term record of the surface LWD-spectra on the East Antarctic plateau should provide experimental proof of the assumed changes in LWD caused by increasing CO_2.

Bibliography

Allen, J.R.; 1971: *Measurements of Cloud Emissivity in the 8–13 µ Waveband*. Journal of Applied Meteorology 10, pp. 260–265. DOI:10.1175/1520-0450(1971)010<0260:MOCEIT>2.0.CO;2.

Arndt, J.E., Schenke, H.W., Jakobsson, M., Nitsche, F.-O., Buys, G., Goleby, B., Rebesco, M., Bohoyo, F., Hong, J.K., Black, J., Greku, R.K., Udintsev, G.B., Barrios, F., Reynoso-Peralta, W., Taisei, M., Wigley, R.; 2013: *The International Bathymetric Chart of the Southern Ocean (IBCSO) - digital bathymetric model*. PANGAEA - Data Publisher for Earth & Environmental Science. http://dx.doi.org/10.1594/PANGAEA.805734.

Beer, R., Glavich, T.A., Rider, D.M.; 2001: *Tropospheric emission spectrometer for the Earth Observing System's Aura satellite*. Applied Optics 40, pp. 2356–2367. DOI:10.1364/AO.40.002356.

Berrisford, P., Dee, D., Poli, P., Brugge, R., Fielding, K., Fuentes, M., Kållberg, P., Kobayashi, S., Uppala, S., Simmons, A.; 2011: *The ERA-Interim archive* [Version 2.0]. European Centre for Medium Range Weather Forecasts, Shinfield Park, Reading, UK, 23 pp.

Chamberlain, J.W.; 1987: *Theory of planetary atmospheres: an introduction to their physics and chemistry*, 2nd ed. ed, International geophysics series. Academic Press, Orlando, USA, 481 pp. ISBN 0-12-167251-4.

Chapman, W.L., Walsh, J.E.; 2007: *A Synthesis of Antarctic Temperatures*. Journal of Climate 20, pp. 4096–4117. DOI:10.1175/JCLI4236.1.

Colwell, S., Turner, J.; 2014: *Antarctic Climate Data - Results From the SCAR READER Project* [WWW Document]. URL http://www.antarctica.ac.uk/met/READER/ (accessed 2014-05-20).

Dee, D.P., Uppala, S.M., Simmons, A.J., Berrisford, P., Poli, P., Kobayashi, S., Andrae, U., Balmaseda, M.A., Balsamo, G., Bauer, P., Bechtold, P., Beljaars, A.C.M., van de Berg, L., Bidlot, J., Bormann, N., Delsol, C., Dragani, R., Fuentes, M., Geer, A.J., Haimberger, L., Healy, S.B., Hersbach, H., Hólm, E.V., Isaksen, L., Kållberg, P., Köhler, M., Matricardi, M., McNally, A.P., Monge-Sanz, B.M., Morcrette, J.-J., Park, B.-K., Peubey, C., de Rosnay, P., Tavolato, C., Thépaut, J.-N., Vitart, F.; 2011: *The ERA-Interim reanalysis: configuration and performance of the data assimilation system*. Quarterly Journal of the Royal Meteorological Society 137, pp. 553–597. DOI:10.1002/qj.828.

DKRZ; 2014: *ESGF Portal* [WWW Document]. URL http://esgf-data.dkrz.de/esgf-web-fe/ (accessed 2014-09-02).

Douglass, A., Brill, J.; 2014: *Aura atmospheric chemistry - The Aura Mission* [WWW Document]. URL http://aura.gsfc.nasa.gov/about.html (accessed 2014-07-01).

Dutton, E.G., Michalsky, J.; 2014: *Basic measurements and other of radiation from the Baseline Surface Radiation Network (BSRN) Station South Pole (SPO) in the years 1994 to 2012, reference list of 226 datasets*. PANGAEA - Data Publisher for Earth & Environmental Science. http://dx.doi.org/10.1594/PANGAEA.150004.

Forster, P.M. de F., Shine, K.P.; 1999: *Stratospheric water vapour changes as a possible contributor to observed stratospheric cooling*. Geophysical Research Letters 26, pp. 3309–3312. DOI:10.1029/1999GL010487.

Fretwell, P., Pritchard, H.D., Vaughan, D.G., Bamber, J.L., Barrand, N.E., Bell, R., Bianchi, C., Bingham, R.G., Blankenship, D.D., Casassa, G., Catania, G., Callens, D., Conway, H., Cook, A.J., Corr, H.F.J., Damaske, D., Damm, V., Ferraccioli, F., Forsberg, R., Fujita, S., Gim, Y., Gogineni, P., Griggs, J.A., Hindmarsh, R.C.A.,

Holmlund, P., Holt, J.W., Jacobel, R.W., Jenkins, A., Jokat, W., Jordan, T., King, E.C., Kohler, J., Krabill, W., Riger-Kusk, M., Langley, K.A., Leitchenkov, G., Leuschen, C., Luyendyk, B.P., Matsuoka, K., Mouginot, J., Nitsche, F.O., Nogi, Y., Nost, O.A., Popov, S.V., Rignot, E., Rippin, D.M., Rivera, A., Roberts, J., Ross, N., Siegert, M.J., Smith, A.M., Steinhage, D., Studinger, M., Sun, B., Tinto, B.K., Welch, B.C., Wilson, D., Young, D.A., Xiangbin, C., Zirizzotti, A.; 2013: *Bedmap2: improved ice bed, surface and thickness datasets for Antarctica*. The Cryosphere 7, pp. 375–393. DOI:10.5194/tc-7-375-2013.

Gluck, S., Cosic, S.; 2008: *TES News: Global Survey Revised* [WWW Document]. URL http://tes.jpl.nasa.gov/news/index.cfm?FuseAction=ShowNews&NewsID=16 (accessed 2014-10-23).

Gluck, S., Cosic, S.; 2014: *TES: Data Calendar* [WWW Document]. URL http://tes.jpl.nasa.gov/data/datacalendar/ (accessed 2014-10-23).

Govett, M.; 2014: *NOAA/ESRL Radiosonde Database* [WWW Document]. URL http://www.esrl.noaa.gov/raobs/ (accessed 2014-02-18).

Griffith, K.T., Cox, S.K., Knollenberg, R.G.; 1980: *Infrared Radiative Properties of Tropical Cirrus Clouds Inferred from Aircraft Measurements*. Journal of the Atmospheric Sciences 37, pp. 1077–1087. DOI:10.1175/1520-0469(1980)037<1077:IRPOTC>2.0.CO;2.

Hansen, J., Ruedy, R., Sato, M., Lo, K.; 2010: *Global surface temperature change*. Reviews of Geophysics 48. DOI:10.1029/2010RG000345.

Hansen, J., Sato, M.K.I., Ruedy, R., Nazarenko, L., Lacis, A., Schmidt, G.A., Russell, G., Aleinov, I., Bauer, M., Bauer, S.; 2005: *Efficacy of climate forcings*. Journal of Geophysical Research 110, p. D18104.

Hori, M., Aoki, T., Tanikawa, T., Motoyoshi, H., Hachikubo, A., Sugiura, K., Yasunari, T.J., Eide, H., Storvold, R., Nakajima, Y., Takahashi, F.; 2006: *In-situ measured spectral directional emissivity of snow and ice in the 8–14 µm atmospheric window*. Remote Sensing of Environment 100, pp. 486 – 502. DOI:10.1016/j.rse.2005.11.001.

IPCC [Stocker, T.F., Qin, D., Plattner, G.-K., Tignor, M., Allen, S.K., Boschung, J., Nauels, A., Xia, Y., Bex, V., Midgley, P.M. (Eds.)]; 2013: *Climate change 2013: the physical science basis: Working Group I contribution to the Fifth assessment report of the Intergovernmental Panel on Climate Change*. Cambridge University Press, Cambridge, United Kingdom and New York, USA, 1535 pp. ISBN 978-1-107-057999-1.

Kiehl, J.T., Trenberth, K.E.; 1997: *Earth's Annual Global Mean Energy Budget*. Bulletin of the American Meteorological Society 78, pp. 197–208. DOI:10.1175/1520-0477(1997)078<0197:EAGMEB>2.0.CO;2.

König-Langlo, G., Sieger, R., Schmithüsen, H., Bücker, A., Richter, F., Dutton, E.G.; 2013: *Global Climate Observing System (GCOS) - Baseline Surface Radiation System (BSRN) - Update of the Technical Plan for BSRN Data Management* [GCOS - 174, WCRP - 24/2013]. World Meteorological Organisation, Geneva, Switzerland, 26 pp.

Kopp, G., Lean, J.L.; 2011: *A new, lower value of total solar irradiance: Evidence and climate significance*. Geophysical Research Letters 38. DOI:10.1029/2010GL045777.

Langematz, U.; 2003: *Thermal and dynamical changes of the stratosphere since 1979 and their link to ozone and CO_2 changes*. Journal of Geophysical Research 108. DOI:10.1029/2002JD002069.

Lewicki, S., Shepard, D., Madatyan, M., Gluck, S.; 2009: *Earth Observing System (EOS) Tropospheric Emission Spectrometer (TES) Science Data Processing Standard and Special Observation Data Products Specifications* [Version 11.9 (Science Software Release 11.3) ESDT Version 4]. Jet Propulsion Laboratory California

Institute of Technology, Pasadena, California, USA, 111 pp.

Loeb, N.G., Wielicki, B.A., Doelling, D.R., Smith, G.L., Keyes, D.F., Kato, S., Manalo-Smith, N., Wong, T.; 2009: *Toward Optimal Closure of the Earth's Top-of-Atmosphere Radiation Budget*. Journal of Climate 22, pp. 748–766. DOI:10.1175/2008JCLI2637.1.

Marshall, G.J.; 2003: *Trends in the Southern Annular Mode from Observations and Reanalyses*. Journal of Climate 16, pp. 4134–4143. DOI:10.1175/1520-0442(2003)016<4134:TITSAM>2.0.CO;2.

Myers, B.A.; 2000: *Atmospheric Longwave Infrared Emission Spectroscopy of Water Vapor at the South Pole*. Physics Department, University of Denver, USA, 5 pp. http://digitalcommons.usu.edu/spacegrant/2000/2000/4/.

Nan, S., Li, J.; 2003: *The relationship between the summer precipitation in the Yangtze River valley and the boreal spring Southern Hemisphere annular mode*. Geophysical Research Letters 30. DOI:10.1029/2003GL018381.

National Oceanic and Atmospheric Administration, National Aeronautics and Space Administration, United States Air Force; 1976: *US Standard Atmosphere, 1976*. US Government Printing Office, Washington, DC.

Notholt, J., Toon, G., Jones, N., Griffith, D., Warneke, T.; 2006: *Spectral line finding program for atmospheric remote sensing using full radiation transfer*. Journal of Quantitative Spectroscopy and Radiative Transfer 97, pp. 112 – 125. DOI:10.1016/j.jqsrt.2004.12.025.

Palchetti, L., Bianchini, G.; 2014: *Radiation Explorer in the Far InfraRed - Prototype for Applications and Developments; Atmospheric Physics at Dome Concordia 75°S 123°E* [WWW Document]. URL http://refir.ifac.cnr.it/refir-pad-prana.html (accessed 2014-11-10).

Palchetti, L., Di Natale, G., Bianchini, G.; 2014: *Characterization of optical and micro-physical properties of cirrus clouds using a wideband thermal infrared spectrometer*. Presented at the European Geosciences Union General Assembly 2014, Geophysical Research Abstracts, Copernicus Publications, Vienna, Austria.

Peterson, D.B., Margitan, J.M.; 1995: *Upper Atmospheric Research Satellite Correlative Measurements Program (UARS-CMP), Balloon Data Atlas*. National Aeronautics and Space Administration, Washington, DC, USA, 214 pp.

Rothman, L.S., Gordon, I.E., Barbe, A., Benner, D.C., Bernath, P.F., Birk, M., Boudon, V., Brown, L.R., Campargue, A., Champion, J.-P., Chance, K., Coudert, L.H., Dana, V., Devi, V.M., Fally, S., Flaud, J.-M., Gamache, R.R., Goldman, A., Jacquemart, D., Kleiner, I., Lacome, N., Lafferty, W.J., Mandin, J.-Y., Massie, S.T., Mikhailenko, S.N., Miller, C.E., Moazzen-Ahmadi, N., Naumenko, O.V., Nikitin, A.V., Orphal, J., Perevalov, V.I., Perrin, A., Predoi-Cross, A., Rinsland, C.P., Rotger, M., Šimečková, M., Smith, M.A.H., Sung, K., Tashkun, S.A., Tennyson, J., Toth, R.A., Vandaele, A.C., Vander Auwera, J.; 2009: *The HITRAN 2008 molecular spectroscopic database*. Journal of Quantitative Spectroscopy and Radiative Transfer 110, pp. 533–572. DOI:10.1016/j.jqsrt.2009.02.013.

Salby, M.L.; 1996: *Fundamentals of atmospheric physics*, International geophysics series. Academic Press Limited, San Diego, California, USA, 627 pp. ISBN 0-12-615160-1.

Schmidt, G.A., Ruedy, R.A., Miller, R.L., Lacis, A.A.; 2010: *Attribution of the present-day total greenhouse effect*. Journal of Geophysical Research 115, p. D20106.

Schmithüsen, H., Sieger, R., König-Langlo, G.; 2012: *BSRN Toolbox - a tool to create quality checked output files from BSRN datasets and station-to-archive files* [WWW Document]. URL http://doi.pangaea.de/10.1594/PANGAEA.774827 (accessed 2012-09-10).

Schmunk, R.B.; 2014: *GISS Surface Temperature Analysis: Global Maps from GHCN v3 Data* [WWW Document]. URL http://data.giss.nasa.gov/gistemp/maps/ (accessed 2014-06-02).

Shindell, D.T.; 2004: *Southern Hemisphere climate response to ozone changes and greenhouse gas increases*. Geophysical Research Letters 31. DOI:10.1029/2004GL020724.

Smith, C.H., Harper, D.A.; 1998: *Mid-Infrared Sky Brightness Site Testing at the South Pole*. Publications of the Astronomical Society of the Pacific 110, pp. 747–753. DOI:10.1086/316170.

Steig, E.J., Schneider, D.P., Rutherford, S.D., Mann, M.E., Comiso, J.C., Shindell, D.T.; 2009: *Warming of the Antarctic ice-sheet surface since the 1957 International Geophysical Year*. Nature 457, pp. 459–462. DOI:10.1038/nature07669.

Taylor, K.E., Stouffer, R.J., Meehl, G.A.; 2012: *An Overview of CMIP5 and the Experiment Design*. Bulletin of the American Meteorological Society 93, pp. 485–498. DOI:10.1175/BAMS-D-11-00094.1.

Thomas, G.E., Stamnes, K.; 1999: *Radiative Transfer in the Atmosphere and Ocean* -. Cambridge University Press, Cambridge, UK, 517 pp. ISBN 978-0-521-40124-1.

Thompson, D.W.J., Solomon, S.; 2002: *Interpretation of Recent Southern Hemisphere Climate Change*. Science 296, pp. 895–899. DOI:10.1126/science.1069270.

Thompson, D.W.J., Solomon, S., Kushner, P.J., England, M.H., Grise, K.M., Karoly, D.J.; 2011: *Signatures of the Antarctic ozone hole in Southern Hemisphere surface climate change*. Nature Geoscience 4, pp. 741–749. DOI:10.1038/ngeo1296.

Thompson, D.W.J., Wallace, J.M.; 2000: *Annular Modes in the Extratropical Circulation. Part I: Month-to-Month Variability**. Journal of Climate 13, pp. 1000–1016. DOI:10.1175/1520-0442(2000)013<1000:AMITEC>2.0.CO;2.

Town, M.S., Walden, V.P., Warren, S.G.; 2005: *Spectral and Broadband Longwave Downwelling Radiative Fluxes, Cloud Radiative Forcing, and Fractional Cloud Cover over the South Pole*. Journal of Climate 18, pp. 4235–4252. DOI:10.1175/JCLI3525.1.

Town, M.S., Walden, V.P., Warren, S.G.; 2007: *Cloud Cover over the South Pole from Visual Observations, Satellite Retrievals, and Surface-Based Infrared Radiation Measurements*. Journal of Climate 20, pp. 544–559. DOI:10.1175/JCLI4005.1.

Turner, J., Colwell, S.R., Marshall, G.J., Lachlan-Cope, T.A., Carleton, A.M., Jones, P.D., Lagun, V., Reid, P.A., Iagovkina, S.; 2004: *The SCAR READER Project: Toward a High-Quality Database of Mean Antarctic Meteorological Observations*. Journal of Climate 17, pp. 2890–2898. DOI:10.1175/1520-0442(2004)017<2890:TSRPTA>2.0.CO;2.

Van Allen, R., Murcray, F.J., Liu, X.; 1996: *Mid-infrared measurements of the atmospheric emission over the South Pole using a radiometrically calibrated Fourier transform spectrometer*. Applied Optics 35, p. 1523. DOI:10.1364/AO.35.001523.

Walden, V.P., Warren, S.G., Murcray, F.J.; 1998: *Measurements of the downward longwave radiation spectrum over the Antarctic Plateau and comparisons with a line-by-line radiative transfer model for clear skies*. Journal of Geophysical Research 103, p. PP. 3825–3846. DOI:199810.1029/97JD02433.

Wild, M., Folini, D., Schär, C., Loeb, N., Dutton, E.G., König-Langlo, G.; 2012: *The global energy balance from a surface perspective*. Climate Dynamics. DOI:10.1007/s00382-012-1569-8.

Zhang, Y.; 2005: *Global tectonic and climatic control of mean elevation of continents, and Phanerozoic sea level change*. Earth and Planetary Science Letters 237, pp. 524–531. DOI:10.1016/j.epsl.2005.07.015.

List of figures

List of tables

Acronyms

		Introduced on page
ALFIP	**A**utomatic **L**ine **FI**nding **P**rogram	50
AR5	**5**th Assessment **R**eport of the IPCC, working group I (IPCC 2013)	16
ASL	**A**bove **S**ea **L**evel	18
BSRN	**B**aseline **S**urface **R**adiation **N**etwork	51
CMIP5	**5**th phase of the **C**oupled **M**odel **I**ntercomparison **P**roject	76
DJF	**D**ecember, **J**anuary, **F**ebruary	25
ECMWF	**E**uropean **C**entre for **M**edium-**R**ange **W**eather **F**orecast	51
ERA	**E**CMWF **R**e**A**nalysis	51
GCM	**G**eneral **C**irculation **M**odel	33
GHE	**G**reen**H**ouse **E**ffect	14
GHG	**G**reen**H**ouse **G**as	14
GISS	**G**oddard **I**nstitute for **S**pace **S**tudies	24
GISTEMP	**GI**SS **S**urface **TEMP**erature Analysis	24
IGY	**I**nternational **G**eophysical **Y**ear	20
IPCC	**I**ntergovernmental **P**anel on **C**limate **C**hange	16
ITCZ	**I**nner-**T**ropical **C**onvergence **Z**one	38
JJA	**J**une, **J**uly, **A**ugust	25
LWD	**L**ong-**W**ave **D**ownwelling radiation at the surface	66
LWU	**L**ong-**W**ave **U**pwelling radiation at the surface	51
MAM	**M**arch, **A**pril, **M**ay	25
NASA	**N**ational **A**eronautics and **S**pace **A**dministration	37
READER	**RE**ference **A**ntarctic **D**ata for **E**nvironmental **R**esearch	20
RF	**R**adiative **F**orcing	16
RT	**R**adiative **T**ransfer	50

SAM **S**outhern **A**nnular **M**ode 29

SCAR **S**cientific **C**ommittee on **A**ntarctic **R**esearch 20

SON **S**eptember, **O**ctober, **N**ovember 25

TES **T**ropospheric **E**mission **S**pectrometer 37

TOA **T**op **O**f **A**tmosphere 13

UV **U**ltra**V**iolet 11

Mathematical symbols

		Introduced on page
a	attenuation	35
α	emissivity of the atmosphere	48
B_λ	spectral radiance of a black body (Planck function)	13
c	*In Chapter 1*: speed of light	13
c	*In Chapter 2*: atmospheric CO_2 concentration	34
F_{BB}	radiative flux of a black body (Stefan-Boltzmann function)	14
$F_{\lambda,sat}$	satellite observation of spectral irradiance	35
$F_{\lambda,surf}$	spectral radiance emitted by the atmosphere towards the surface	50
$F_{\lambda,TOA}$	spectral irradiance emitted to space	34
F_{TOA}	long-wave radiative flux emitted to space	48
G	greenhouse effect	48
G_{CO2}	greenhouse effect of CO_2	34
h	Planck constant	13
h_{sat}	altitude of the satellite	35
h_{TOA}	altitude of the top of the atmosphere	35
k	Boltzmann constant	13
LWD	long-wave downwelling radiative flux at the surface	50
LWU	long-wave upwelling radiative flux at the surface	52
λ	wavelength	13
λ_{max}	highest wavelength of satellite observation	37
λ_{min}	lowest wavelength of satellite observation	37
$\lambda_{w,max}$	upper bounding wavelength of atmospheric window	36
$\lambda_{w,min}$	lower bounding wavelength of atmospheric window	36

λ_0	wavelength that separates the solar and terrestrial spectra	14
ν	wave number	37
r_{earth}	mean radius of the Earth	35
σ	Stefan-Boltzmann constant	14
T	temperature	13
T_{atm}	temperature of the atmosphere	48
T_{eff}	effective temperature of $F_{\lambda,TOA}$ in an atmospheric window	36
T_{surf}	temperature of the emitting surface	36

Acknowledgements

First of all, I thank my tutors and colleagues:

Dr. Gert König-Langlo for the many fruitful and constructive discussions, for which he was available virtually at all times. I found it a great privilege to discuss new ideas straight away, whenever they appeared.

Prof. Dr. Peter Lemke for his support, particularly for rethinking the governing idea behind this study over and over again, consolidating my confidence in my theory.

Prof. Dr. Justus Notholt for the supply of and constructive help with his radiative transfer model ALFIP, but also for the astute comments on my work.

Soumia Serrar and Thomas Jung for carrying out and getting me interested in the ECMWF experiments shown here.

I like to thank the many people, that stand behind the measurements and model data, which I was able to use. Without there continuous effort over decades, this study would not have been possible.

Last but not least I thank my wife Tosia Schmithüsen, who has supported me at all stages.